NTNU

Norwegian University of
Science and Technology

Process- and Alloy Development of Recyclable Aluminium Alloys

Recovery and Recrystallization Behavior of a Selection of AlMn-model Alloys

Jarl Erik Morsund Flatøy

Chemical Engineering and Biotechnology
Submission date: June 2011
Supervisor: Knut Marthinsen, IMTE
Co-supervisor: Gavin Wang, IMT

Norwegian University of Science and Technology
Department of Materials Science and Engineering

Erklæring

Jeg bekrefter herved at diplomoppgaven er utført selvstendig og i samsvar med Reglement for sivilarkitekt- og sivilingeniøreksamen ved Norges teknisk-naturvitenskapelige universitet (NTNU).

Trondheim, 23. juni 2011

_____

Jarl Erik Flatøy

Preface

The work presented in this report has been carried out in Trondheim, at the Norwegian University of Science and Technology (NTNU), Department of Materials Technology, in the period from January to June 2011 as my master's thesis, TMT4900. My supervisor has been Professor Knut Marthinsen, and my co-supervisor has been PhD-student Gavin Wang, and I thankfully acknowledge both their contributions in helping and guiding me throughout this work.

I would also like to thank engineer Pål Ulseth, engineer Yingda Yu, post doc. Youngjun Chen, and PhD-student Sindre Bunkholt, for their technical assistance, and also for all their helpful comments.

This project work has been conducted as a part of the MOREAL-project, a collaboration between Hydro, Sapa, NTNU and SINTEF. The main objective of the MOREAL-project is to develop and improve physically based numerical through process models to predict the microstructure evolution during homogenization, deformation, and softening (recovery and recrystallization) as well as the mechanical properties of the semi products of primary and recycle-based aluminium alloys.

Trondheim, June 2011

Jarl Erik Flatøy

Contents

Abstract

A study of the effect of various amounts of manganese in solid solution on the recovery and recrystallization behavior of an AlMn-alloy, for different annealing conditions after different degrees of deformation (cold rolling) has been carried out. The alloy studied was a 3xxx-type model alloy with 0.5 wt% Fe, 0.15 wt% Si and 1.0 wt% Mn. The studies were a contribution to the MOREAL-project, where the main objective is to quantify and characterize the softening behavior of recyclable aluminium alloys, with small amounts of manganese, iron and silicon, as a basis to validate and further develop the ALSOFT-model. 5 variants of the AlMn-alloy, with respect to strain and homogenization, were prepared and further investigated.

Based on electrical conductivity measurements the different amounts of Mn in solid solution, after the different homogenization (hom.) treatments, were estimated to be approximately 0.85 wt% (as cast), 0.55 wt% (hom. nr. 2) and 0.49 wt% (hom. nr. 3). The reductions of Mn in solid solution by hom. nr. 2 and hom. nr. 3 resulted in less concurrent precipitation and consequently a larger effective driving force for recovery and recrystallization. The high amount of Mn in solid solution for the as cast variants resulted in much concurrent precipitation.

Concurrent precipitation was found to delay and suppress the recovery and recrystallization processes. At high annealing temperatures, with no (or little) concurrent precipitation occurring, the recrystallised grain structures were found to be homogeneous, fine grained and consisting of equiaxed grains. In these cases the recrystallised textures were found to be approximately random after a strain of 0.7, while they showed cube textures of weak and medium strength after a strain of 3.0. At low annealing temperatures, with concurrent precipitation occurring, the recrystallised grain structures were found to be inhomogeneous and coarse grained, with grains elongated in the rolling direction. In these cases the recrystallised textures were found to consist of P-textures and ND-rotated cube textures of medium and high strength.

A high degree of deformation was found to increase the rate and degree of the recovery and recrystallization processes during the isothermal annealing procedures, and to result in fine recrystallised grain structures, consistent with the increased effective driving force for recovery and recrystallization. A high degree of deformation was also found to increase the rate and magnitude of precipitation during the isothermal annealing procedures.

Non-isothermal annealing experiments were carried out to investigate if they could result in significantly different grain structures and textures compared to the isothermal annealing experiments. No significantly different results were achieved, only results directly comparable to the results from the isothermal annealing experiments.

1. Introduction

The energy needed to re-melt aluminium is only 5 % of the total energy needed to produce an equal amount of primary aluminium. This is because of the low melting point of aluminium. Therefore, it is highly profitable and environmentally friendly to produce as much aluminium as possible through recycling and re-melting of scrap aluminium.

During recycling, alloying elements will accumulate and as a consequence new demands to alloy design arise. This is why the aluminium producers Hydro and Sapa together with NTNU and SINTEF have formed a Norwegian Research Council-supported competence project, MOREAL (Modelling towards Value-added Recycling Friendly Aluminium Alloys), where the effect of varying amounts of alloying elements in aluminium is studied. The objective of the project is to develop and improve physically based numerical through process models to predict the microstructure evolution during homogenization, deformation, and softening (recovery and recrystallization) as well as the mechanical properties of the semi products of primary and recycle-based aluminium alloys. One of these models is the ALSOFT-model which calculates evolution in the microstructure and changes in the mechanical properties during recovery and recrystallization after deformation.

The present work is an extension of my TMT4500 work [1], and some of the results presented in this thesis were obtained during the TMT4500 work. These results are included since they are critical for the understanding of the present work, which has been carried out as a part of the total activity within the MOREAL-project and was intended as a contribution to the overall objective of the project. The work was limited to a 3xxx-type model alloy with 0.5 wt% Fe, 0.15 wt% Si and 1.0 wt% Mn, named C2. The main objective of the work was to study the effect of the small amounts of manganese, iron and silicon on the recovery and recrystallization behavior of the alloy, during annealing after different degrees of deformation.

More specifically, five different variants of the C2-alloy were achieved by different homogenization treatments and by deforming the alloy to different degrees of strain. The five

variants were subsequently annealed isothermally and non-isothermally at different temperatures and times, mechanically tested, and the microstructures and textures were studied. This was done to achieve better understanding and quantitative description of the softening behavior (i.e. amount and kinetics of recovery, nucleation and kinetics of recrystallization, and fully annealed grain structure and texture) in the alloy that was studied and to use this to validate and further develop the ALSOFT-model.

In addition, due to challenges characterizing the texture of the C2-alloy variants using the electron back-scatter diffraction (EBSD) method, a lot of work was done to optimize the sample preparation, the EBSD-scanning parameters and the post-processing of the EBSD-data. This is reflected in the detailed description of the EBSD procedure used in this work presented in the experimental chapter.

2. Theoretical Background

The following chapter covers the theoretical background for this work and is divided into 7 parts, where the first part gives a general introduction to non-heat treatable aluminium alloys. The second part gives a more detailed description of the 3xxx-alloys. The third part of this chapter provides a short presentation of the homogenization process. Cold deformation and typical microstructural phenomena during deformation are the topics in the fourth part of this chapter. The fifth part describes annealing (precipitation, recovery and recrystallization), while the sixth part covers texture and texture development during deformation and annealing. The final part of this chapter presents the different characterization methods used during this work.

2.1 Non-Heat Treatable Aluminium Alloys

Non-heat treatable aluminium alloys owe their strength mainly to elements in solid solution and deformation hardening. These alloys can also to some extent get strength contributions from particles and special texture components. In general, heat treatment of this type of alloys will not produce any kind of strengthening precipitates like heat treatment will for the heat treatable aluminium alloys. An exception is dispersoids formed in the AlMn-alloys. AA1xxx (commercial pure aluminium with small additions of mainly Fe and Si), AA3xxx (AA1xxx-alloys with primarily Mn additions), AA5xxx (AA1xxx-alloys with Mg additions) and AA8xxx (AA1xxx-alloys with larger alloy additions) are all alloy-systems belonging to this class [2].

2.2 3xxx-Alloys

The 3xxx-alloys belong to the AlMn-class of alloys and are non-heat treatable. Mn is the main alloying element and contributes to the strength of the alloy through solid solution strengthening (where the interaction of Mn with the dislocations results in increased glide resistance, and consequently a stronger material). Elements like Fe, Si, Cu and Mg are also often added to the 3xxx-alloys. Cu and Mg are added mainly to improve the strength of the 3xxx-alloys. In the present work, however, the focus has been on a 3xxx-alloy with 1.0 wt%

Mn, 0.5 wt% Fe and 0.15 wt% Si. Fe and Si are added primarily to increase the precipitation rate of Mn to create large constituent particles acting as nuclei for recrystallization. Because these phases will have a very different electrochemical potential than the matrix (making the alloy prone to corrosion), as much as 1.0 wt% Mn is added to the alloy. The Mn diffuses into the particles, creating more of a balance between the electrochemical potential of the particles and the matrix, and the alloy is again very resistant to corrosion. Since the particles become larger because of the 1.0 wt% Mn, they also become better nucleation sites for recrystallization after deformation [2] [3].

Mn in solid solution may result in precipitation of dispersoids during thermomechanical processing of the 3xxx-alloys. These dispersoids are known to affect the softening processes (recovery and recrystallization) and may result in a coarse grain structure through pinning of subgrain boundaries during recovery and thus suppression of the nucleation of recrystallization, as well as slowing down the recrystallization process itself through a reduced effective driving force for growth of recrystallization grains, due to the Zener-drag the dispersoids induce. The combination of these dispersoids, which retard the softening processes, and the constituent particles that work as nucleation sites for recrystallization is an important aspect of the 3xxx-alloys. By adjusting the particle and dispersoids structures it is possible to control the microstructure development during thermomechanical treatment [2].

The 3xxx-alloys are frequently used for their good combination of strength, formability, corrosion performance and weldability. Typical applications for the 3xxx-alloys are beverage cans, heat exchangers and aluminium foil.

2.3 Homogenization

Most aluminium alloys are typically subjected to a homogenization heat treatment after casting. The primary goals of this treatment is to eliminate the consequences of microsegregation, reduce Mn in solid solution and obtain desirable particle size distributions, including fine dispersoids and coarser constituents. As mentioned in Chapter 2.2, these

particles and dispersoids have a strong influence on the alloy, and especially the recrystallization kinetics, texture development, grain size and mechanical properties of the alloy. This is why the homogenization procedure is important with regard to the control of the microstructure evolution [2] [4] [5] [6] [7].

Knut Sjølstad [8] showed that homogenization at 610 °C for 14 hours (before water quenching) of an as cast LP 3103-alloy containing 0.57 wt% Fe, 0.12 wt% Si, 1.0 wt% Mn, 0.015 wt% Mg and 0.012 wt% Cu (almost the same alloy as the C2-alloy investigated in this work) resulted in a decrease of Mn in solid solution from 0.80 wt% to 0.59 wt%.

Li and Arnberg [9] have shown that the electrical conductivity increased with increasing homogenization temperature for AA3003-alloys and AA3103-alloys, which means that the supersaturated solution decomposed and that dispersoids were formed. They found that the conductivity reached a maximum at around 500-530 °C due to dissolution of dispersoids with the increased solubility for Mn in solid solution. But when the temperature was increased to 600 °C the conductivity increased even more due to growth of constituent particles [2].

2.4 Cold Work – Deformation

The final microstructure and texture of a deformed material after annealing is closely linked to the microstructure that developed during deformation. A thorough characterization of the deformed structure is therefore necessary. Characteristic features of the deformation microstructure are described in the following, along with a description of the cold work procedure applied in this work.

2.4.1 Cold Rolling

For aluminium, cold work is performed below temperatures of 150 °C since recovery and recrystallization will occur at higher temperatures. Cold rolling is a typical cold work procedure and is performed by passing the material through a pair of rolls (as shown in Fig.

2.1) until the desired material thickness is achieved. During cold rolling (or cold work), the lattice is distorted by introduction of defects and consequently changes in the microstructure occur. These changes include elongated grains (see Fig. 2.1), an increase in dislocation density, an increase in entanglement of dislocations and re-orientation of the grains in the direction of the applied stress (see Fig. 2.1). This increases the stored energy in the material and consequently also the driving force for reactions like recovery and recrystallization.

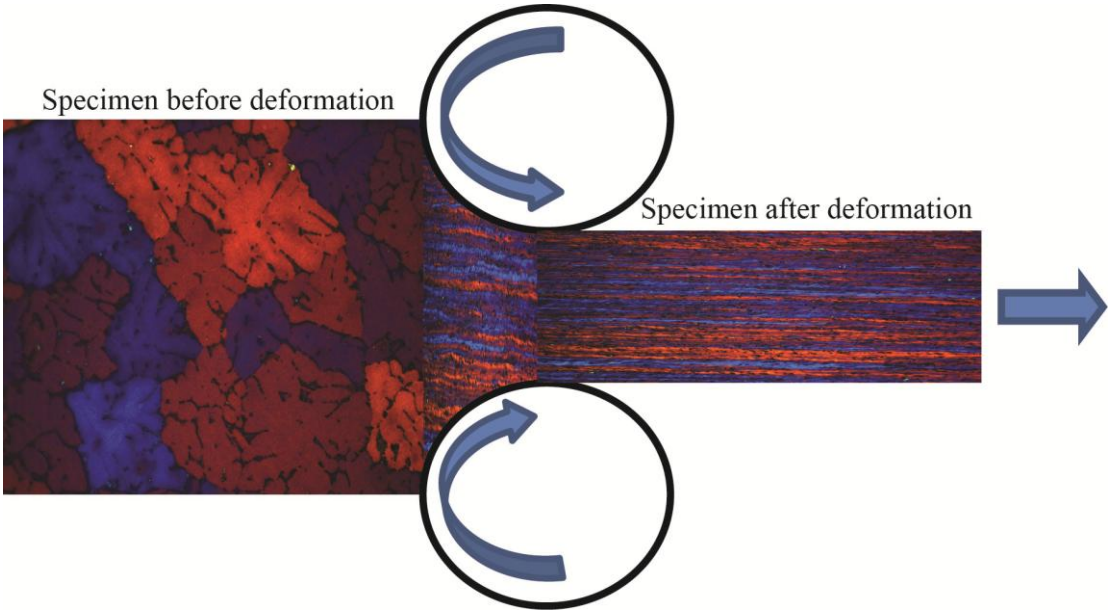

Fig. 2.1: An indication of how the grain structure change during the cold rolling procedure

2.4.2 Deformation Heterogeneities

During cold deformation, several microstructural phenomena occur and certain microstructure features characteristic for the deformed state develop. The most common ones will be described briefly in the following.

Slipbands/Microbands

Slipbands/microbands represent an intrinsic slip mode, which dominates the sub-structure evolution at low to intermediate strains. Slipbands/microbands are crystallographic in nature

and form on {111} slip planes in FCC-metals. Microbanding is the typical slip mode in aluminium alloys with a high content of elements in solid solution due to the increased capability to store dislocations. Slipbands/microbands are associated with small misorientation to the surrounding matrix and are of no significance as nucleation sites for recrystallization [2] [8].

Transition Bands

Transition bands are defined as bands separating different parts of a grain, which has split and rotated away from each other during deformation. Neighboring volumes of a grain deform on different slip systems and rotate towards different, but stable end orientations, and transition bands develop. A transition band is hence a region of sharp orientation gradients with cumulative misorientations across the band, indicating an ideal site for nucleation of recrystallization [2] [8].

Shear Banding

A shear band is a narrow zone of intense shearing strain (see Fig. 2.2), and the formation of such a zone is highly dependent on the stacking fault energy of the material. Aluminium has high stacking fault energy and shear banding in aluminium requires large deformations. Shear banding occurs when the dislocation density saturates. The material becomes unstable with respect to shear and shear banding becomes the alternative slip mode which accommodates strain. In addition to large amounts of strain, the shear bands contain fine substructures of cells/subgrains that are extended in the band direction and large misorientations with respect to the surroundings. Shear bands are non-crystallographic and macroscopic [2] [8].

Deformation Zones

In aluminium alloys, the formation of deformation zones occurs at hard non-deformable particles larger than approximately 2 μm. Applied strain, temperature and particle size are some of the factors determining the microstructure and the size of the deformation zones.

Dislocations accumulate at the particles because of incompatibility between the plastically deforming matrix and the non-deforming particles. These zones (see Fig. 2.3) can act as nucleation sites for recrystallization because they have a high dislocation density, small subgrains (i.e. locally a high stored energy) and high angle boundaries to the surroundings. This mechanism for creation of recrystallization nuclei is named particle stimulated nucleation (PSN) of recrystallization [2] [8] [10] [11].

Fig. 2.2: Shear banding [10]

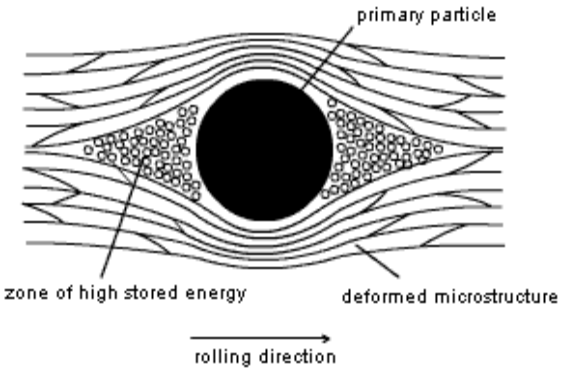

Fig. 2.3: Deformation zone around particle [10]

Old Grain Boundaries

Grain boundaries are heterogeneities already present in the microstructure before deformation takes place, and these heterogeneities are changed during the deformation. A large increase of the grain boundary area per unit volume is introduced during cold deformation since the originally equiaxed shape of the grains change towards flat elongated grains. The grain boundaries constitute obstacles for dislocation movement just like the hard non-deformable particles, resulting in a sharpening of the lattice rotation and a refinement of the microstructure close to the boundaries. The high angle grain boundaries work as ideal sites for nucleation of recrystallization by SIBM (strain induced boundary migration) due to large misorientation and small subgrain sizes (high local stored energy) in the grain boundary regions [2] [8].

2.4.3 Sub-Structure Development

In alloys of high stacking fault energy (γ_{SFE}) the dislocations are typically arranged in a cell structure after deformation, where the cell walls are complex dislocation tangles. The sizes of these cells are dependent on material and strain. High stacking fault energy, large strain and low solute content are parameters that further promote accumulation of dislocations in the cell boundaries. The boundaries become more defined with defined misorientations, and the cell structures develop into sub-grain structures [2] [11].

The dislocation density within the sub-grains (ρ_i), the sub-grain size (δ) and the misorientation across sub-grain boundaries (φ) are the most commonly used parameters for describing the global deformed microstructure. Further, each grain rotates towards particular orientations during the deformation [2] [8].

Interior Dislocation Density (ρ_i)

After low reductions the principle of similitude ($\delta \times \sqrt{\rho_i}$ = constant) is expected to be obeyed. It is also reasonable to assume that the ratio between the number of interior dislocation and those found in the sub-structure will decrease with strain [8].

The dislocation density and sub-grain size of a variety of Al-alloys and deformation modes where measured by Nord-Varhaug et al. [12]. They observed that the dislocation density converged towards a saturation density after cold deformation to strains larger than 0.2.

Cell/Sub-Grain Size (δ)

Uniform equiaxed cells are formed at strains typically below 0.2. Deformation occurs by multiple slip for intermediate strains and the equiaxed cells will elongate in the deformation direction and the microstructure becomes more inhomogeneous. A more uniform

microstructure will appear at large strains, where all cells have collapsed into pancake shaped grains with well-defined sub-grain boundaries with a given misorientation [8].

Misorientation (φ)

The boundary misorientation between the sub-grains change during deformation and extensive work on this topic has been carried out during the last decades. Furu et al. [13] compiled the available data on aluminium deformed to a variety of strains and found that the misorientation increased rapidly with strain and saturated at approximately 3 ° after a strain of about one.

Stored Energy (P_D)

As mentioned above, the stored energy in the material is increased during deformation and it is this stored energy that is providing the driving force for recovery and recrystallization during annealing of the material. Almost all of the stored energy introduced during deformation is derived from the accumulation of dislocations and therefore the stored energy (P_D) can be described as a function of the dislocation density in the interior of the subgrains (ρ_i), the subgrain size (δ) and subgrain boundary energy (γ_{sb}), as seen in Equation 2.1 (G is the shear modulus, b is the Burgers vector and κ is a geometrical constant) [2] [8]:

$$P_D = \rho_i \frac{Gb^2}{2} + \kappa \frac{\gamma_{sb}}{\delta} \qquad (2.1)$$

In Equation 2.1 the subgrain boundary energy can be calculated using the Read Shockley relation [2] [8]:

$$\gamma_{sb} = \frac{Gb\varphi}{4\pi(1-\upsilon)} \ln\left(\frac{e\varphi_c}{\varphi}\right) \qquad (2.2)$$

The boundary misorientation, φ_c (typically taken to be ≈ 15 °) is the critical misorientation separating between what is a high angle grain boundary and a low angle grain boundary, and υ is the Poisson ratio [2] [8].

2.5 Annealing Behavior of a Deformed Material

Ductility can partially be restored in a work-hardened metal by annealing. Recovery, recrystallization and precipitation are the most common phenomena that can occur during annealing, and are therefore more thoroughly presented in the following chapters. During precipitation, dispersoids are formed which may retard recovery and recrystallization. During recovery, dislocations are annihilated, dislocations rearrange and subgrain grows. During recrystallization new strain free grains nucleate in certain areas of the material and grow to consume the deformed or recovered microstructure [8] [10].

Annealing of a deformed AlMn-alloy leads to a hardness reduction due to recovery and recrystallization. A typical plot of hardness vs. annealing time is presented in Fig. 2.4. It is indicated in the figure where it is assumed that the different annealing phenomena (recovery and recrystallization) are occurring. Fig. 2.5 – Fig. 2.7 shows EBSD-OIM-images of how the microstructure is expected to develop during annealing; from a clearly deformed structure, to a recovered deformation structure with some growing grains, to a deformation free recrystallised structure.

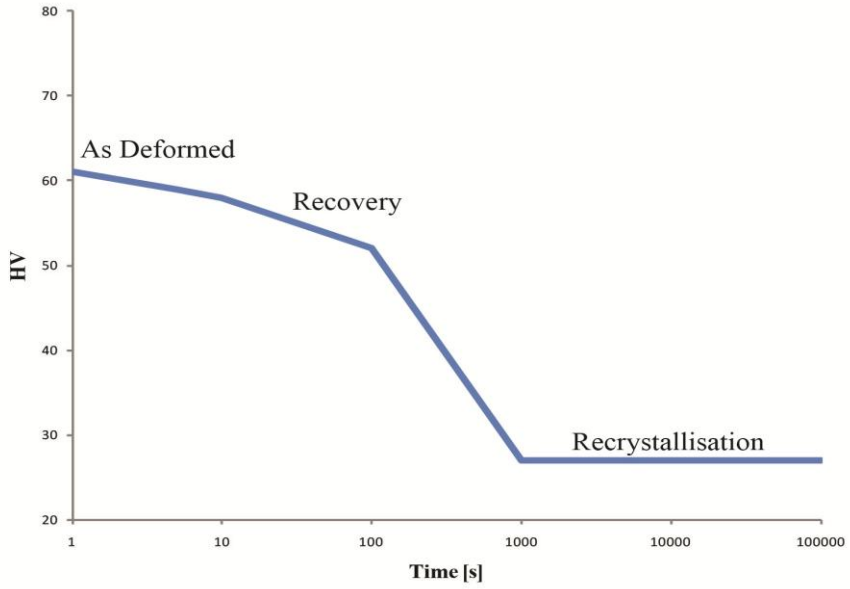

Fig. 2.4: A typical softening curve (HV vs. annealing time)

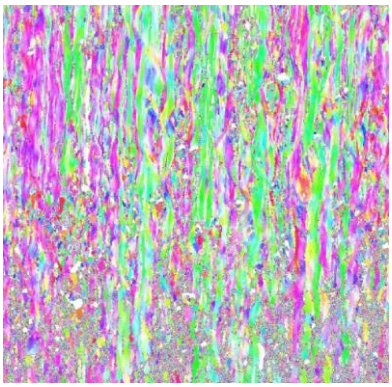

Fig. 2.5: As-Deformed

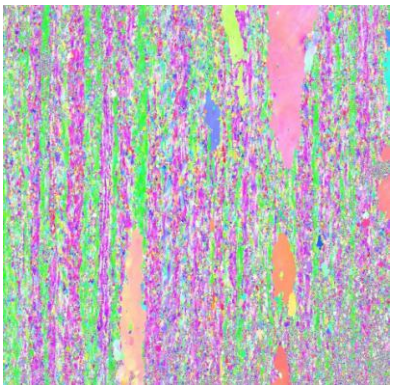

Fig. 2.6: Recovery

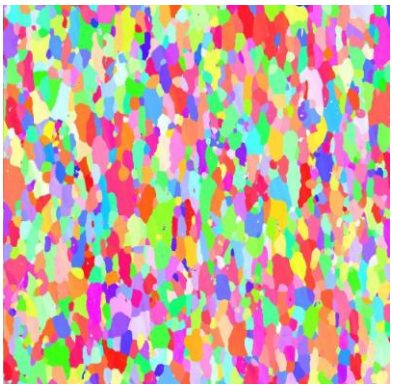

Fig. 2.7: Recrystallised

Sæter [14] found that the hardness can increase slightly in the early stages of annealing for deformed AlMn-alloys at low temperatures. By investigations in the transmission electron microscope (TEM) indications of cluster formations of solute atoms were found for these alloys, which might explain the slight increase in hardness. The effect has also been found to be less significant with increasing temperatures due to an increased recovery rate [8] [14] [15].

2.5.1 Precipitation

Nucleation and growth of a precipitate is associated with the decomposition of a supersaturated solid solution. Nucleation is in almost every case occurring heterogeneously at grain- or phase boundaries, dislocations, stacking faults or at clusters of vacancies. These places are natural places for nucleation because these sites are associated with a higher average free energy than in the metal matrix [8].

The Zener-drag

The Zener-drag is a retarding force from a dispersion of small precipitates/dispersoids exerted upon a moving grain boundary. To move a boundary past a particle a force has to be exerted which is related to the particle size and the energy of the boundary. For a random distribution

of particles, the pinning force exerted on the boundary is given by Equation 2.3 where γ is the grain boundary energy, f is the particle volume fraction and r is the particle radius [8] [11].

$$P_z = \frac{3 f_r \gamma}{2r} \tag{2.3}$$

The precipitation will affect both the subgrain-growth and the growth of recrystallized grains. During recovery the dispersoids from precipitation prevents the sub-grains to grow large enough to nucleate new strain free grains (see Equation 2.5 below). Fewer strain free grains nucleated from overcritical sub-grains leads to larger grains after recrystallization since each grain can grow larger than if there were more nucleation from overcritical sub-grains. In the most extreme cases no nucleation from sub-grains will happen and the alloy will only soften due to slow sub-grain growth. During recrystallization the precipitated dispersoids will pin and slow down the movement of the grain boundaries, which mainly will affect the speed of the recrystallization (i.e. the time to reach a fully recrystallised condition). The pinning during recrystallization will not (or to a very small degree) affect the number of recrystallized grains and the size of these.

Hornbogen and Köstner [16] studied the effect of precipitation on recrystallization for two different supersaturated and deformed Al-alloys and found that recrystallization will be affected by precipitation unless recrystallization has completed before precipitation begins. A schematic illustration (TTT-diagram) of the recrystallization behavior as a function of time and temperature is given in Fig. 2.8.

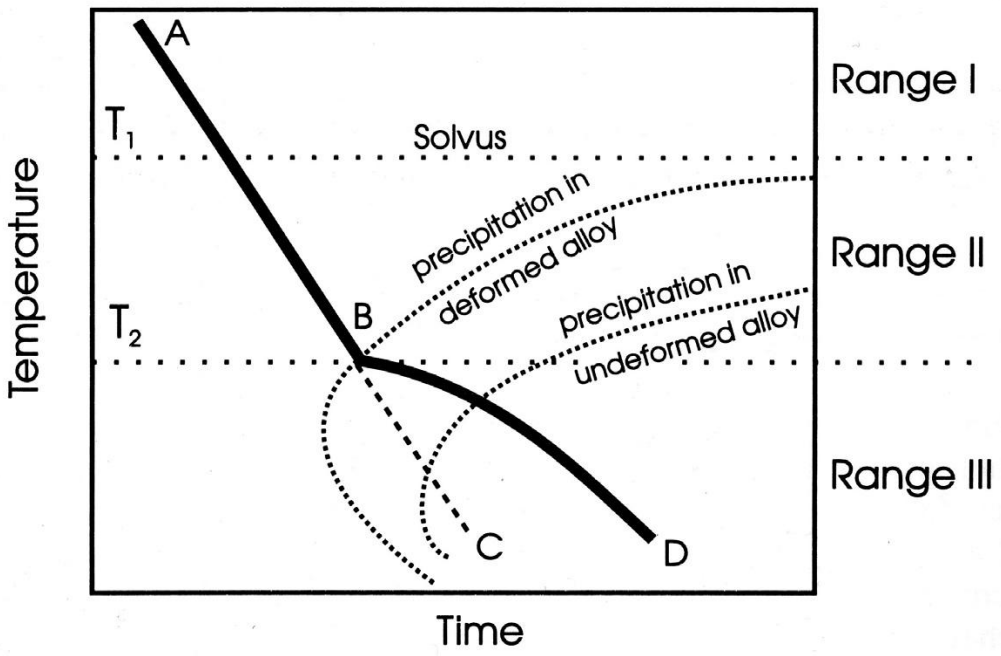

Fig. 2.8: The influence of concurrent precipitation on softening kinetics [16]

Absence of precipitation would result in recrystallization occurring at times given by the line AC. Concurrent precipitation has slowed down the process in line BD. As seen above TTT-diagrams are a helpful method of interpreting the precipitation and recrystallization reactions, and as shown in Fig. 2.8 these diagrams are divided into three regions. Range I is above the solvus temperature (T_1), and no precipitation is possible in this region. In range II precipitation occurs after recrystallization is completed, and no retarding effects will be observed. In range III precipitation occurs before recrystallization, which results in a postponed start of recrystallization. The sharp transition between range II and range III is only an illustration and is not true for real situations. This is because a certain period of time is required to complete recrystallization. In the transient period both regions operated simultaneously at different sites in the material [2] [8].

The Effect of Manganese

Morris and Liu [17] have shown that when manganese is retained in solid solution prior to subsequent cold working and annealing it can cause a significant retardation in the start and

end of recrystallization (up to a factor of 500X) due to (concurrent) precipitation of a fine dispersion of $MnAl_6$ during annealing.

Haan et al. [18] have shown that after casting as much as 1 wt% of manganese can retain in solid solution due to the low diffusivity of the Mn-atoms even at 600 °C. The Al_6Mn equilibrium phase is formed during solidification and following processing. $Al_6(Mn,Fe)$-particles are formed if the alloy contains iron. $Al_{12}(Mn,Fe)Si$-particles are formed if the silicon-content is larger than 0.07 wt%. Haan et.al [18] found that the precipitation rate for a binary AlMn-alloy reached its maximum at 490 °C. Growth was found to be the limiting factor below this temperature, while nucleation of new precipitates was found to limit the decrease of Mn in supersaturated solid solution at higher temperatures.

In both the works of Alexander & Greer [19] and Watanabe et al. [20] the Fe/Mn concentration ratio was observed to decrease with increasing holding time during homogenization. This indicates that the supersaturation of Mn in solid solution diffuses into the α-particles during the entire homogenization treatment.

Li and Arnberg [21] demonstrated that a commercial AA3003-alloy reached a maximum precipitation rate (for manganese containing dispersoids) during homogenization at about 490 °C.

The Effect of Iron

Furu et al. [13] found that an increase of 0.01 wt% Fe in solid solution shifted the softening of a commercially pure aluminium alloy towards significantly longer annealing times (especially for lower annealing temperatures). Further, Ito et al. [22] found the recrystallization texture of two different AlFe-alloys to be dominated by the cube texture if a low supersaturation of iron was present prior to recrystallization. R-oriented grains dominated the recrystallization texture in the opposite condition.

The rate of recrystallization is known to be increased by iron bearing constituent particles due to the formation of recrystallization nuclei within the deformation zones (see Chapter 2.4.2) [8].

The Effect of Silicon

Since silicon increases the rate of particle formation during heat-treatment, the particles become larger and the number of available nucleation sites for recrystallization by PSN (see Chapter 2.4.2) increases [8].

According to Hausch et al. [23] increasing amounts of Si in a binary AlMn-alloy increases the precipitation rate and retards the recrystallization rate.

2.5.2 Recovery

After plastic deformation there are large amounts of stored internal energy in the metal, which can be released by heating the metal to an elevated temperature. At elevated temperatures edge dislocations may move in a direction perpendicular to their Burgers vector and line by climb. Climb involves the addition or removal of atoms at the extra half plane associated with the edge dislocation. Climb occurs by atomic diffusion and vacancy migration, and is the rate controlling mechanism of recovery. For metals, like aluminium, with high stacking fault energy (γ_{SFE}) climb is much easier, which means that a substantial proportion of the stored energy in aluminium (after deformation) can be consumed by recovery [8] [10] [11].

Recovery is the earliest onset of re-arrangement of crystal defects within the deformed microstructure of the heated metal, and during recovery, some restoration of the original structure and properties may occur through annihilation of point defects and dislocations, and through spatial re-arrangement of dislocations, as a consequence the stored energy of the metal is lowered. Since dislocations re-arrange faster at higher temperatures, an increased annealing temperature can increase the extent of the recovery at the same holding time. Solute

atoms can also affect the recovery causing retardation by interactions with the dislocations in the alloy [10] [11].

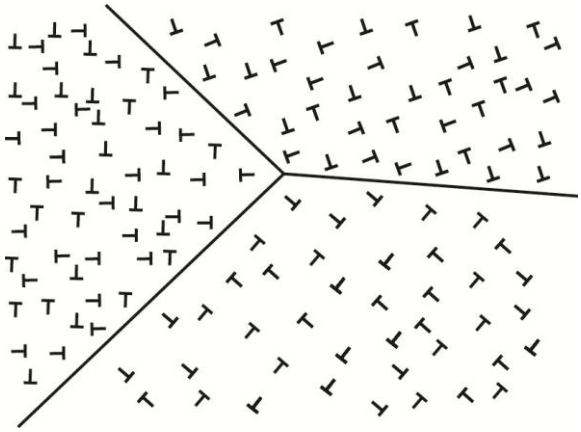

Fig. 2.9: Deformed Microstructure

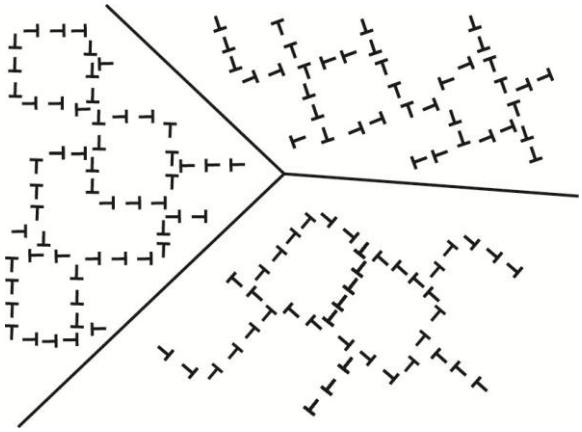

Fig. 2.10: Recovered Microstructure

In a simplified explanation of recovery, the re-arrangement of dislocations (that was mentioned above) begins with the dislocations arranging themselves from the deformed condition (Fig. 2.9) into cell networks (where the cell walls consist of complex dislocation structures) within the existing grains. The recovery process continues with the dislocations inside the cell walls re-arranging into more regular dislocation networks (low angle grain boundaries), and the cell structure becomes a sub-grain structure (Fig. 2.10). But this is (as mentioned) a highly simplified explanation of recovery in aluminium. In metals with high stacking fault energy the dislocations are typically already arranged in a cell formation after deformation. A well developed sub-grain formation might even be in place after deformation of aluminium, which makes the processes during recovery somewhat more complex than described above. However, recovery will continue with growth of the sub-grains either way, and as a consequence the stored energy in the material is further lowered [8] [10] [11].

The sub-grain growth may occur by two mechanisms; by growth of larger sub-grains at the expense of smaller ones, or by sub-grain coalescence where neighboring sub-grains rotate into one sub-grain by a boundary diffusion process. The later mechanism is only relevant after small deformations and low annealing temperatures. The driving force for both growth

mechanisms is the reduction of the total grain boundary area and the reduction of grain boundary energy [8] [10] [11].

The sub-grain growth plays an important role for nucleation of recrystallization, since large sub-grains works as nucleation sites for recrystallization (see Equation 2.5). It is therefore often difficult to make a division between recovery and the early stages of recrystallization [8].

2.5.3 Recrystallization

Recrystallization involves the nucleation and growth of new and dislocation free grains in certain areas of the material, which grow to consume the deformed or recovered microstructure. Even after considerable recovery, the microstructure still contains large amounts of stored energy, and further reduction is obtained by recrystallization. The normal process for recrystallization is the formation of a small region of nearly perfect nuclei and the growth of these into the surrounding deformed material.

Processing factors that influence recrystallization are temperature, heating rate, strain and strain rate. Increased temperature increases the rate of recrystallization, so does increased heating rate. If the material is rapidly heated, there is less time for recovery and greater driving force for recrystallization. Increased strain and increased strain rate will also generally result in increased rate of recrystallization [2] [8] [11] [24].

Microstructural factors that influence recrystallization are initial grain size, second phase particles (size, distribution and coherency), solute content and texture. Fine initial grain size increases recrystallization rate. Second phase particles can promote recrystallization through increasing the stored energy in the material and through PSN. Second phase particles (if small) can also retard recrystallization by pinning grain boundaries. Solute additions can retard grain boundary movement and inhibit recrystallization. Both starting texture and

deformation texture influence the overall recrystallization rate. Different texture components can lead to inhomogeneous recrystallization [2] [8] [11] [24].

The fraction recrystallized (X) can be calculated using the Johnson-Mehl-Avrami Equation:

$$X(t) = 1 - \exp(-kt^n) \tag{2.4}$$

Where k is a constant and n is the growth exponent. This is based on a constant growth rate, isotropically growth in three dimensions and a random distribution of nucleation sites [2] [8] [10]. In the case of site saturation nucleation kinetics (the nucleation rate decreases so rapidly that all nucleation events effectively occur simultaneously at the start of recrystallization) n is equal to 3, n is equal to 4 if a constant nucleation rate is applied [A]. However, for Al-alloys n-values are typically measured to be approximately 2 [25].

For recrystallization of aluminium alloys it is generally assumed that all the nuclei are present in the deformed state and that they are growing at a constant growth rate. The nuclei must be both thermodynamically stable and of a certain size in order to grow. The critical radius in order for a nucleus to form a strain free grain is given by the Gibbs-Thomson relationship [2] [8]:

$$R > R_c = \frac{2\gamma_{GB}}{P} \tag{2.5}$$

Where γ_{GB} is the specific grain boundary energy and $P = P_D - P_Z$ is the effective stored energy (see Equation 2.1, 2.2 and 2.3) [8]. Here P_z is the so-called Zener drag, a retarding force due to finely dispersed dispersoids (see Chapter 2.5.1). A grain fulfilling the requirement of Equation 2.5 will grow with a growth rate (v) given by [2] [8]:

$$v = M(P_D - P_Z) \tag{2.6}$$

Where M is the mobility of the grain defined by [2] [8]:

$$M = \frac{M_0}{RT}\exp\left(\frac{U_{GB}}{RT}\right) \tag{2.7}$$

And where M_0 is a material constant, U_{GB} is the activation energy for grain boundary mobility and R is the universal gas constant [2] [8].

The fraction recrystallized assuming site saturation is calculated by the following Equation [8]:

$$X(t) = 1 - \exp\left(-\frac{4}{3}\pi N_{tot}(vt)^3\right) \tag{2.8}$$

Further the final recrystallized grain size can be calculated by [8]:

$$D_{rex} = \left(\frac{1}{N_{tot}}\right)^{\frac{1}{3}} \tag{2.9}$$

Typical nucleation sites in deformed aluminium include; prior high angle grain boundaries, deformation zones around large particles, transition bands, shear bands and special texture components with a low energy configuration. All of these are more thoroughly presented below.

Strain Induced Boundary Migration (SIBM)

This phenomena occurs when an original grain boundary bulge out, leaving behind a dislocation free area. The driving pressure for the process is the difference in stored energy between the two sides of the high angle grain boundary, arising due to the difference in sub-grain size. The side with a large sub-grain size and lower stored energy will grow at the expense of the side with smaller sub-grain size and higher stored energy [2]. Somerday & Humphreys [26] have shown that SIBM is an important nucleation mechanism in an AlMn1,3-alloy cold rolled to 90% deformation. They also reported that this nucleation mechanism seems to be especially important in temperature ranges where recrystallization occurs simultaneously with precipitation of Al_6Mn-dispersoids. Fig. 2.11 shows an illustration of nucleation by SIBM.

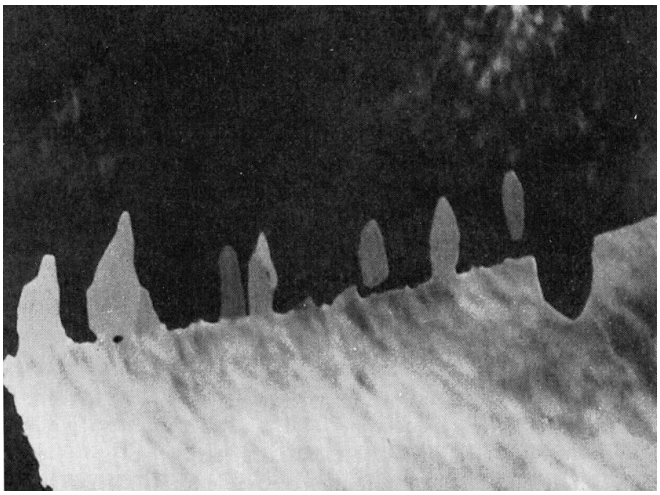

Fig. 2.11: Nucleation by SIBM at a prior high angle grain boundary in high purity aluminium compressed 40% [27]

Ordinary Grain Boundary Nucleation

Nucleation at grain boundaries where the new grains are separated from both its parent grains by sharp boundaries is what is meant by ordinary nucleation. An example of this is shown in Fig. 2.12 below. Hutchinson [28] obtained evidence of the operation of this mechanism in iron bicrystals. New grains where observed to differ in orientation from the original deformed grains by a rotation of approximately 30 degrees around the <111>-normal direction [2].

The nucleation of random oriented grains at grain boundaries compared to PSN in cold deformed aluminium where studied by Vatne et al. [29]. Their observations indicated that nucleation at prior grain boundaries results in a random recrystallization texture [2].

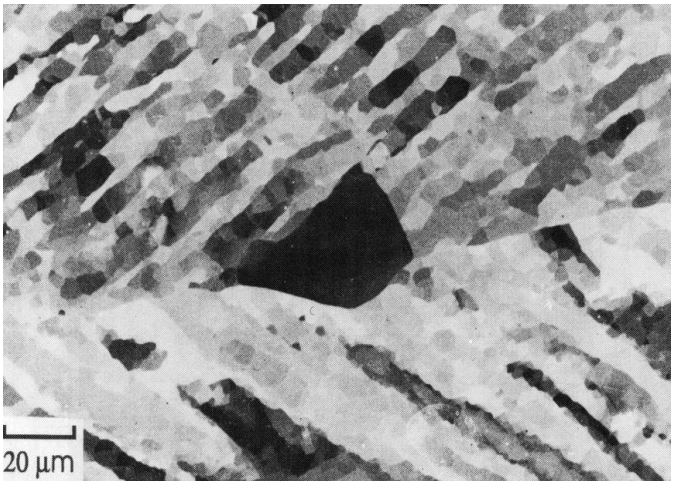

Fig. 2.12: Grain boundary nucleation in aluminium [11]

Nucleation from Cube-Oriented Bands

Nucleation from cube-oriented bands is often treated as a separate nucleation effect due to its importance for several commercial aluminium alloys. As Stian Tangen mentions in his work [2] several investigations of hot deformed aluminium alloys have demonstrated that nucleation of the cube orientation may be associated with cube grains that are metastable during deformation at high temperatures. In the investigations Stian Tangen [2] refers to, the original cube grains changed shape into long elongated bands of the cube orientation. The sub-grains inside the bands were observed to have a size advantage compared to the sub-grains of other orientations, which were believed to be due to a higher recovery rate for the cube orientation. This means that the cube grains reach an over-critical sub-grain size prior to other sub-grains and the cube bands are therefore very efficient as nucleation sites for recrystallization [2].

Transition Bands

A transition band is a region of sharp orientation gradients, and a sub-grain in the transition band can easily gain a boundary of high misorientation by growing into the surrounding areas. The recrystallized grains tend to have preferred orientations due to the fact that the

orientations of the sub-grains in the transition bands are a direct result of the slip process and the strain path. Hjelen and Nes [30] and Ørsund and Nes [31] showed that the nuclei of the cube orientation preferentially formed in transition bands located in bands of the copper orientation in aluminium. Hjelen [32] observed nucleation of both cube- and Goss oriented grains in transition bands in aluminium [2].

Shear Bands

A low local stored energy and a large sub-grain size in the shear band, in addition to a large misorientation gradient to the surroundings imply that nucleation in shear bands may easily take place [2]. The orientations of the nucleated grains seem to be very case dependent as reported by Nes and Hutchinson [33].

Particle Stimulated Nucleation (PSN)

Nucleation at deformation zones developed around coarse second phase particles is an important nucleation mechanism in commercial particle containing alloys, particularly after cold deformation. High stored energy and a large misorientation gradient are built up in the deformation zones around large non-deformable particles during deformation. The deformation zones are well defined as nucleation sites and the number of sites is controlled by alloy composition and processing, which makes it possible to control the recrystallized grain size [2].

Humphreys [34] showed that the orientation of the nucleus in deformation zones will be that of the area from which it grows. A random recrystallization texture is expected after nucleation at secondary particles in a polycrystalline material. But as showed by Engler et al. [35] [36] [37], Engler [38] and Knut Sjølstad [8] PSN might also in some special cases result in both strong P- and ND-rotated cube components.

2.6 Texture

Most common metals (like aluminium) have a polycrystalline structure, i.e. they are composed of a large number of grains of different orientations. The texture of a polycrystalline material denotes the statistical tendency of the crystals to be oriented in a particular way, and it is an important parameter that makes up the characterization of a material together with the measurements of grain and sub-grain sizes and misorientations. Control of the texture development in a material can be very important since texture gives rise to anisotropic material properties including strength, ductility, etc. Texture is usually represented graphically by pole figures and orientation distribution functions (ODFs). Both pole figures and ODFs will be thoroughly described below.

Pole Figures

The orientation of an individual crystallite is defined by the position of its unit cell in space with reference to a coordinate system (A, B, C). The unit cell of the face-centered-cubic aluminium is represented by a cube. It is common and convenient to represent an orientation in the stereographic projection. The stereographic projection is obtained by the following procedure [10]:

1. The unit cube is located in the origin of the coordinate systems and surrounded by the unit sphere.

2. To represent the cube faces in the stereographic projection, the point of intersection of the normal vector of each cube face with the surface of the unit sphere is determined.

3. Only the intersections (1, 2, and 3) on the northern hemisphere are taken into account.

4. Connecting the points of intersection with the south pole yields the intersecting points (1', 2', and 3') in the equatorial plane.

5. They are called poles of the respective cube faces.

Fig. 2.13 and Fig. 2.14 below shows the relationship between the orientation of the unit cell and the <100> poles and the <111> poles on the stereographic projection.

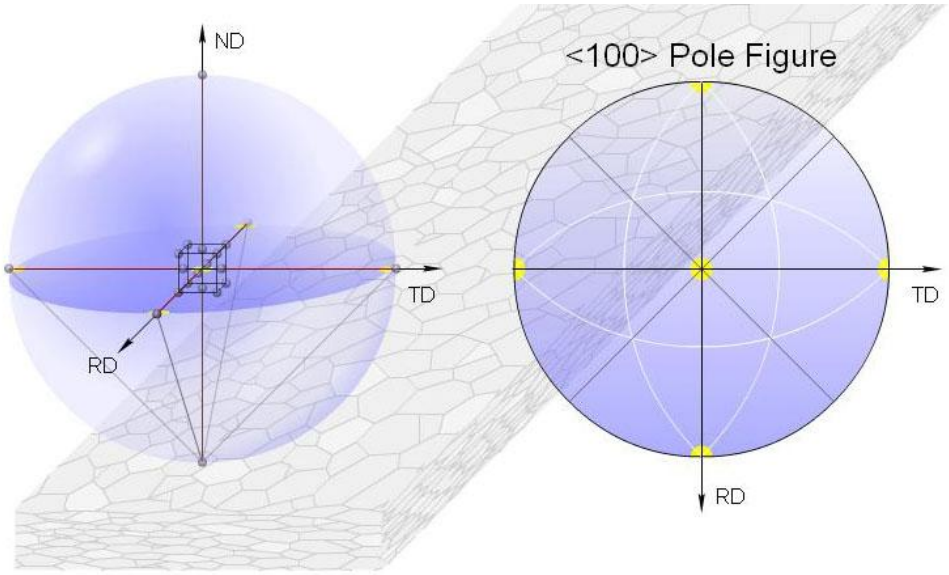

Fig. 2.13: The relationship between the orientation of the unit cell and the <100> poles [10]

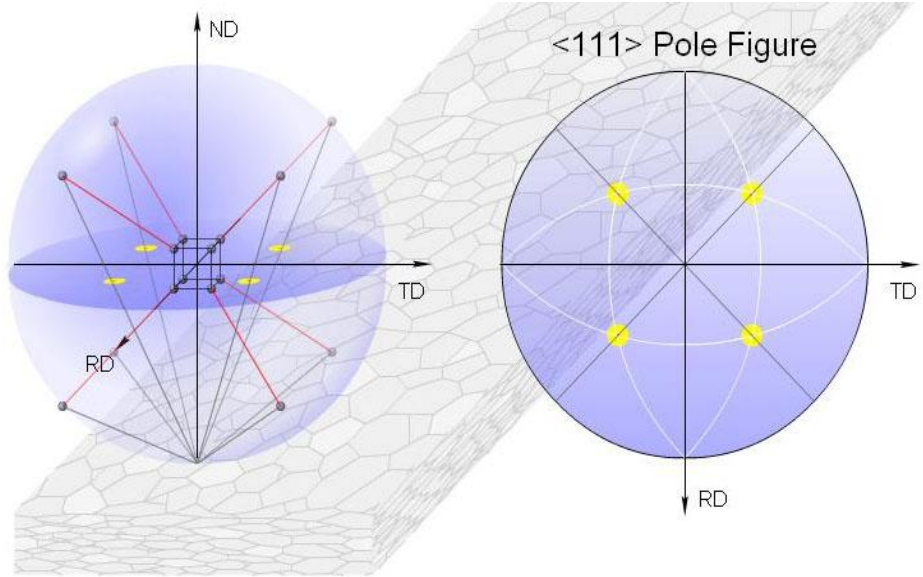

Fig. 2.14: The relationship between the orientation of the unit cell and the <111> poles [10]

The figures above represent the orientation of single crystallites. A set of this kind of poles can be plotted for each individual grain in a polycrystalline material to produce a pole figure.

If the grains are randomly oriented, then we should expect to see the poles distributed evenly over the pole figure. More often the grains are not randomly oriented, but tend towards particular orientations depending on the alloy composition and process history. This is called the "preferred" orientation, or crystallographic texture of the alloy. In this case the poles will be concentrated within certain areas of the pole figure. Unfortunately the pole figures have the limitation that the representation of orientations becomes ambiguous if there is more than one orientation because each orientation is determined by several poles which cannot be associated to a specific orientation in a unique way [10].

Orientation Distribution Functions (ODFs)

For an unambiguous representation of orientations one can take advantage of the fact that orientations can be described uniquely by a rotation; namely the rotation into the reference coordinate system. A set of Euler angles (which commonly are used to describe rotations) φ_1, Φ and φ_2 can therefore uniquely define an orientation. The three Euler angles can be represented by a single point on a 3D-graph – Euler space. Fig. 2.15 shows an illustration of Euler space [10].

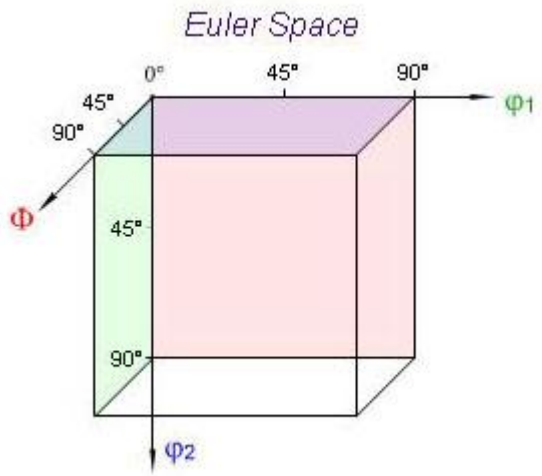

Fig. 2.15: Euler space [10]

In general the angles range over $0° \leq \varphi_1 \leq 360°$; $0° \leq \Phi \leq 180°$; $0° \leq \varphi_2 \leq 360°$. However, because of the cubic crystal symmetry of aluminium alloys, and because of the specimen symmetry at

rolling, one can reduce the angular range to $0°\leq\varphi_1\leq90°$; $0°\leq\Phi\leq90°$; $0°\leq\varphi_2\leq90°$ in which each orientation occurs at least once. Since 3D-graphs can be difficult to interpret it is usual to construct 2D-representations of Euler space. The Euler space are divided into slices of $\varphi_2 = 5°$ intervals as showed in Fig. 2.16 below. These slices are arranged into a grid called ODF, as shown in Fig. 2.17 [10].

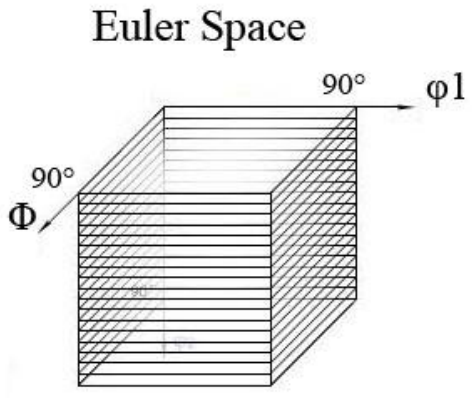

Fig. 2.16: Euler space divided into slices of $\varphi_2 = 5°$

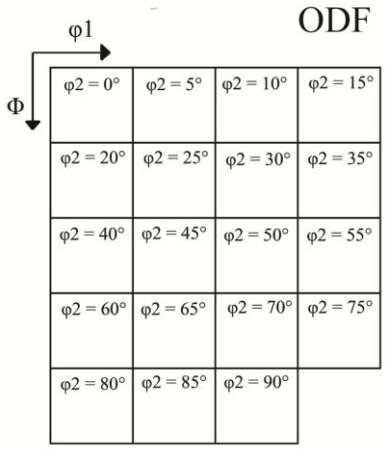

Fig. 2.17: Euler space slices arranged into an ODF

Miller indices and Euler angles of typical orientations of Al and Al-alloys after rolling and after recrystallization are presented in Table 2.1 below.

Table 2.1: Miller indices and Euler angles of typical orientations of Al and Al-alloys after rolling and after recrystallization [8]

Texture component	Miller indices	Euler angles (φ_1, Φ, φ_2)
Cu	{112}<111>	90°, 35°, 45°
S	{123}<634>	59°, 37°, 63°
Bs	{011}<211>	35°, 45°, 0/90°
G	{011}<100>	0°, 45°, 0/90°
Cube	{001}<100>	0°, 0°, 0/90°
$Cube_{RD}$	{013}<100>	22°, 0°, 0/90°
$Cube_{ND}$	{001}<310>	0°, 22°, 0/90°
P	{011}<122>	65°, 45°, 0°
Q	{013}<231>	45°, 15°, 10°
R	{124}<211>	53°, 36°, 60°

2.6.1 Deformation Textures

During plastic deformation the grains of a polycrystal change their shapes and orientations due to stress and strain. The mechanism of plastic deformation of aluminium and its alloys is dislocation-induced slip. This does not produce lattice rotation by itself; it is rather the accommodation of the new grain to its surroundings, which causes the change in orientation. When the deformation of FCC-metals are performed at relatively low temperatures slip occurs on the {111}<$\bar{1}$10>-slip systems. A short description of the typical deformation textures that appears in rolled aluminium are given below.

Cold rolling of aluminium alloys usually leads to an assembly of orientations along two fibers; the β-fiber, running from the Brass orientation (Bs), through S, ending up at the

Copper orientation (Cu), and the α-fiber, running from the Goss orientation (G), to the Brass orientation. A schematic representation of the FCC-rolling texture in Euler space is presented in Fig. 2.18 [8].

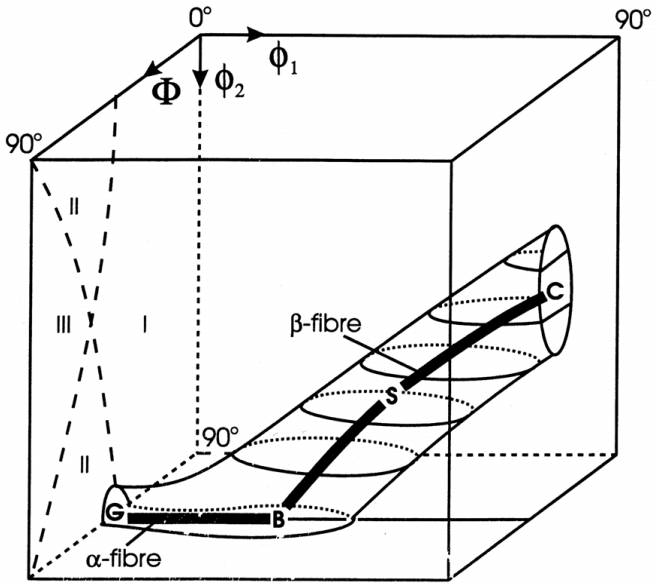

Fig. 2.18: FCC-rolling texture in Euler space [39]

Both the α- and the β-fiber are described by rotations about two different <110>-axis. The normal direction (ND) is parallel to a rotation axis of the α-fiber, and the β-fiber rotation axis has a 60° tilt from ND towards the rolling direction (RD) [39]. At higher strains the α-fiber deteriorates to a single peak at the Bs-orientation, while the β-fiber strengthens at increased strains. However, the β-fiber will deteriorate at reductions beyond 95%, and peaks at certain orientations are developed [8]. Fig. 2.19 below presents a typical rolling texture of an FCC-material where the typical rolling texture components are highlighted.

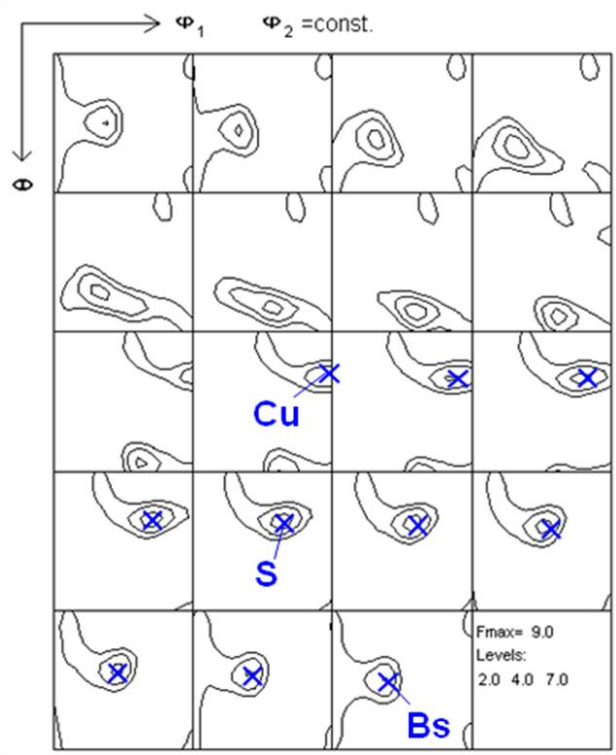

Fig. 2.19: A typical rolling texture of an FCC-material [40]

2.6.2 Recrystallization Textures

The most important recrystallization textures found in Al-alloys are described in the following. A φ_2 = 0° section of an ODF is illustrated in Fig. 2.20 below since all the dominating recrystallization components, except the R-texture, are found in this ODF-section. Three ODFs showing typical recrystallization textures are further presented in Fig. 2.21 – Fig. 2.23. The typical recrystallization components in each ODF are highlighted.

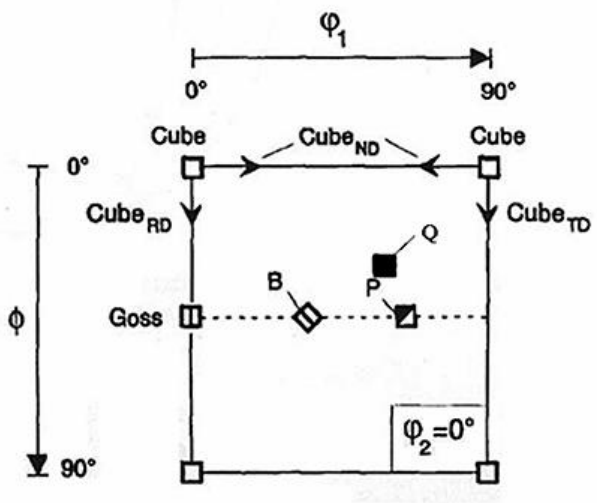

Fig. 2.20: The positions of different texture components in the φ_2-section of an ODF [2]

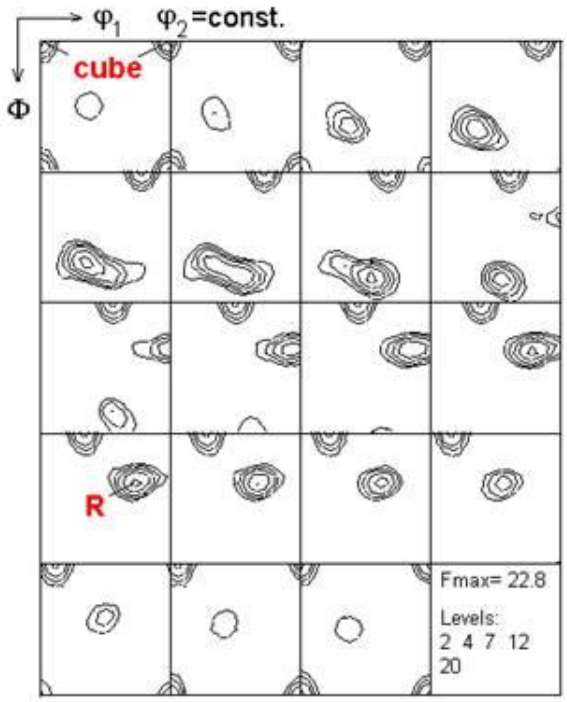

Fig. 2.21: Recrystallization texture example 1 [41]

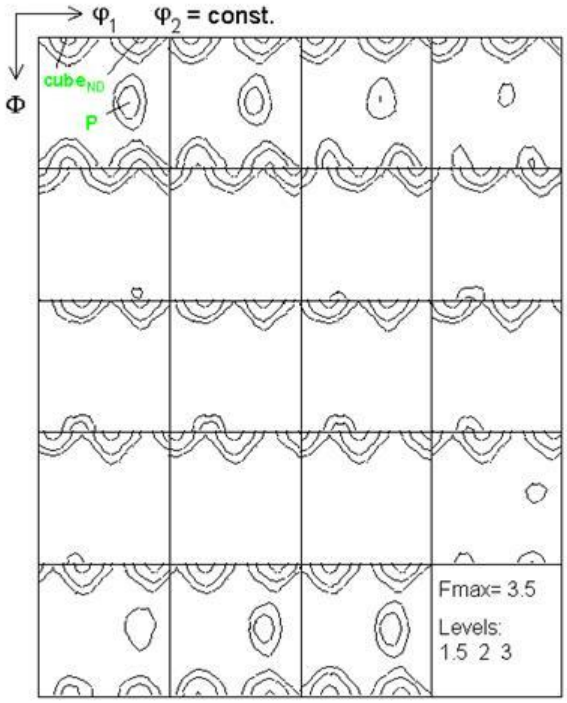

Fig. 2.22: Recrystallization texture example 2 [41]

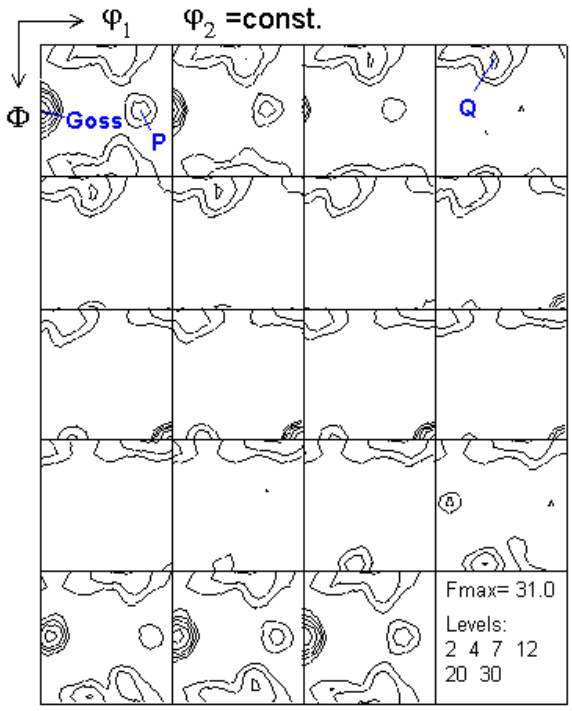

Fig. 2.23: Recrystallization texture example 3 [41]

Cube-Texture

The origin of the cube-texture has been a topic of debate for years. Dillamore and Katoh [42] suggests that crystallites of cube ought to exist in the deformed state as transition bands separating volumes of major rolling texture components. Cube bands have been observed to retain after deformation, especially at high deformation temperatures. The cube intensity is found to decrease with deformation since the metastable cube orientation is assumed to rotate around the RD-direction towards the Goss orientation. Another reason for the cube intensity to decrease with deformation is that more deformation leads to an increased stored energy, and an increased driving force for recrystallization, resulting in a larger number of nucleating sites competing, especially PSN- and grain boundary sites [2] [8].

The cube texture has an approximate 40°<111>-orientation relationship to the S-component (low energy ∑7-boundary) and from each S-variant there is one 40°<111>-rotation that yields

the cube texture. The S-component is often observed to be lower in intensity than the other common rolling components in an ODF. However, the actual volume fraction of S-oriented grains is usually higher than for the Bs- and Cu-orientations due to its low symmetry compared to Bs and Cu. This might be the reason why the cube texture is common in recrystallised Al-alloys. The compromise character of the highly symmetric cube orientation, which can grow into all the four S-variants, further enhances this [2] [8].

The ND-Rotated Cube Component

The ND-rotated cube component has an approximate 40°<111>-rotation relationship to the Cu-orientation. According to Daaland et al. [43] the ND-rotated cube has a growth rate advantage in case of concurrent precipitation compared to other orientations, due to the fact that these grains have a shorter incubation time than other orientations, resulting in less precipitation upon these nuclei [2] [8]. Stian Tangen [2] observed strong ND-rotated cube components when concurrent precipitation occurred during annealing. The strength of the ND-rotated cube texture was gradually reduced with higher annealing temperature (less precipitation).

P-Texture

The P-texture (also called the ND-rotated Goss texture) has been observed in cold rolled and subsequently annealed AlCu-, 3xxx- and 5xxx-alloys with a high supersaturation of alloying elements by Næss [44], Daaland & Nes [45], Vatne et al. [46], Engler et al. [37] and Sjølstad [8]. Similar to the ND-rotated cube, the P-orientation has an approximately 40°<111>-rotation relationship to the Cu-orientation. Both Engler et al. [35] [37] and Sjølstad [8] reported a preferred nucleation of the P- and ND-rotated components in the deformation zones around large particles by PSN. Due to the 40°<111>-orientation relationship with the Cu-component they both further suggested a preferred growth of these grains in the early stages of the annealing. This suggestion was further supported by Ryu & Lee [47] when they showed by TEM-work that nucleation of the P-orientation take place in the deformation zone surrounding large $FeAl_3$-particles [2] [8]. Stian Tangen [2] observed strong P-components

when concurrent precipitation occurred during annealing. The strength of the P-texture was gradually reduced with higher annealing temperature (less precipitation).

Goss-Texture

Usually the Goss orientation is present as a minor component in the deformation texture. However, poor formability is the result of a pronounced Goss orientation in the recrystallization texture. The Goss orientation has a 40°<111>-orientation relationship to the β-fiber orientation between S and Bs. According to Hutchinson et al. [28] the factors that favor the cube texture also favor the formation of Goss texture [2] [8].

R-Texture

After annealing of cold rolled commercial purity Al and certain alloys the R-texture is frequently observed. The R-texture is referred to as retained rolling texture due to its similarity to the S-deformation texture. This appellation is correct only if the recrystallization has occurred by extended recovery [2].

Q-Texture

The presence of particles can lead to inhomogeneous deformation, and both the P-texture and Q-texture seems to show up in cases where inhomogeneous deformation occurs. The Q-texture is also most often found in connection with the presence of P-texture [2].

2.7 Characterization Methods

2.7.1 Hardness Measurements

A cheap, quick and very effective way to follow softening reactions is hardness measurements. A constant compression load is applied on the sample through an indenter, and

the samples ability to withstand permanent plastic deformation can be characterized by studying the dimensions of the indentation caused by the compression load.

Recovered grains are softer than the deformed grains and hence hardness is a strong function of the degree of recrystallization. Hardness will decrease with the degree of recrystallization as seen in Fig. 2.4.

2.7.2 Electrical Conductivity Measurements

Measurements of the electrical conductivity are a suitable method to acquire knowledge about the elements in solid solution and the occurrence of precipitation reactions during annealing. Alloying elements in solid solution will through distortion of the atomic lattice reduce the conductivity of the metal. Semicoherent or incoherent precipitates will on the other hand have a much weaker effect on the conductivity. Various elements in solid solution will influence the conductivity to different degrees. The relationship between the electrical conductivity and the solid solution content in wt% for the alloy investigated can be found by neglecting the temperature dependent term in the Matthiessens rule [2] [8] [48]:

$$\frac{1}{\kappa} = 0{,}0267 + 0{,}036Mn + 0{,}032Fe + 0{,}0068Si \qquad (2.11)$$

The measurements will only give an estimate of the total solid solution content, and it is impossible to separate the contributions from each of the various alloying elements. However, due to the low solubility of iron in aluminium and the relative low total concentration of Si in the investigated alloy, their contribution of the change in electrical conductivity during heat treatment is often neglected in comparison to the Mn concentration [2] [8].

Li and Arnberg [9] have shown that for an AA3103-alloy a large amount of manganese and low amounts of Si and Fe are in solid solution after DC-casting. Hence, the electrical conductivity is predominantly controlled by the Mn in solid solution.

2.7.3 Light Optical Microscopy

The optical microscope is a type of microscope which uses visible light and a system of lenses to magnify images of small samples. It has a low resolution compared to other microscopy techniques like scanning electron microscopy (SEM) and transmission electron microscopy (TEM), but provides a large field of view, is relatively user friendly and a time effective characterization tool. Light optical microscopy (OM) is therefore a suitable method for investigating deformed, partly- and fully recrystallized materials with respect to grain structure. The light optical microscope can also be used to measure the average grain size of the studied material by applying the linear intercept method.

2.7.4 TTT-Diagrams

TTT-Diagrams can be used to illustrate how the precipitation and softening reaction interact with each other in determining overall transformation kinetics. The three T's correspond to time, temperature and transformation. In TTT-diagrams, T_C is defined as the temperature where the precipitation curve crosses the curve which indicates the onset of recrystallization. Concurrent precipitation has little effect on the recrystallisation process above this critical temperature, while at temperatures below T_C, concurrent precipitation will retard recovery and recrystallization.

2.7.5 Electron Back-Scatter Diffraction (EBSD)

EBSD is conducted using a SEM equipped with a phosphor screen, compact lens and a low light CCD camera. When the electron beam hits the specimen in a single point some of the electrons undergo elastic scattering with the atoms in the specimen. On their way out of the specimen a fraction of the electrons are diffracted according to Bragg's law. When some of these electrons hits the phosphor screen located near the specimen they create a typical diffraction pattern that reflects the orientation of the crystal planes for that specific point. A camera behind the phosphor screen images the pattern and sends it to a computer. The orientation of a specific grain or subgrain can be obtained from the EBSD-patterns by

indexing the displayed patterns. Thousands of orientations can be recorded in this manner and one can create an orientation map of the specimen [2].

In addition to providing information about the grain orientations the orientation maps can be combined with statistical tools to measure grain- and sub-grain sizes, misorientations, texture, etc. The EBSD is therefore an excellent tool for investigation and characterization of deformed and recrystallized structures.

3. Experimental

All experiments performed in this work, and how they were done, are described in detail in the following chapter. The chapter is divided into 5 parts, where the first part gives a description of the starting alloy and the following processing. The second part of the chapter describes the characterization of the starting alloy and the alloy variants created by processing of the starting alloy. The third part describes the annealing experiments (isothermal and non-isothermal) conducted in this work. The fourth part of this chapter describes the characterization of the alloy variants after the annealing experiments. The fifth and last part of this chapter describes in detail the texture measurements performed in this work.

As mentioned in the introduction (see Chapter 1), this work is directly based on, and an extension of my TMT4500-work [1] (completed in December 2010). Due to this fact some of the results presented in this work were produced during my TMT4500-work. The experimental procedures described below include both the procedures used during this work and the TMT4500-work, and no clear distinctions between the two are made. However, when the results are presented in Chapter 4, a clear distinction between new and old results will be made.

3.1 Material Selection and Processing

The present work has focused on a 3xxx-type model alloy, called C2, processed in various ways. The nominal chemical composition of the C2-alloy is presented in Table 3.1.

Table 3.1: Chemical composition of the C2-alloy

Alloy	Wt% Fe	Wt% Si	Wt% Mn
C2	0.5	0.15	1.0

The alloy was received in the as cast condition as extrusion ingots with diameter 228 mm from Hydro Sunndalsøra.

Homogenization of C2

The alloy has been homogenized at NTNU to produce materials with different distributions of alloying elements (Mn) between solid solution (ss), dispersoids and particles. The specific heating programs are presented in Table 3.2. The three different variants of the C2-alloy after homogenization are also presented in Table 3.2. The second homogenization procedure is presented in detail in Fig. 3.1, while the third homogenization procedure is presented in detail in figure 3.2. The homogenization procedures were all carried out in a laboratory oven (see fig 3.3 below).

Table 3.2: The three variants of the C2-alloy after homogenization

Name	Mn in ss	Dispersoids	Homogenization procedure
C2-A1	High	Low	(Nr. 1) - As cast
C2-B1	Medium	Low	(Nr. 2) – Heated 50 °C/h, held at 600 °C for 24 h, quenched
C2-C1	Low	High	(Nr. 3) – Heated 50 °C/h, held at 600 °C for 4 h, cooled 25 °C/h, held at 500 °C for 4 h, quenched

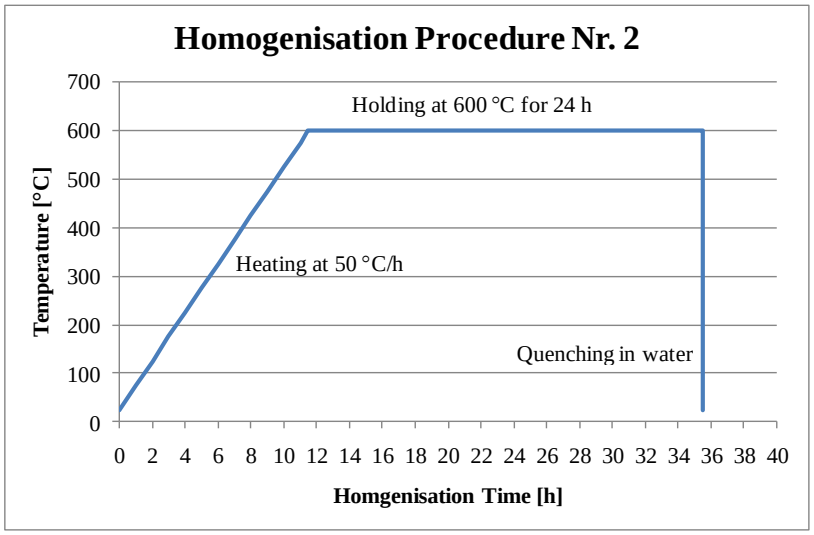

Fig. 3.1: The second homogenization procedure in detail

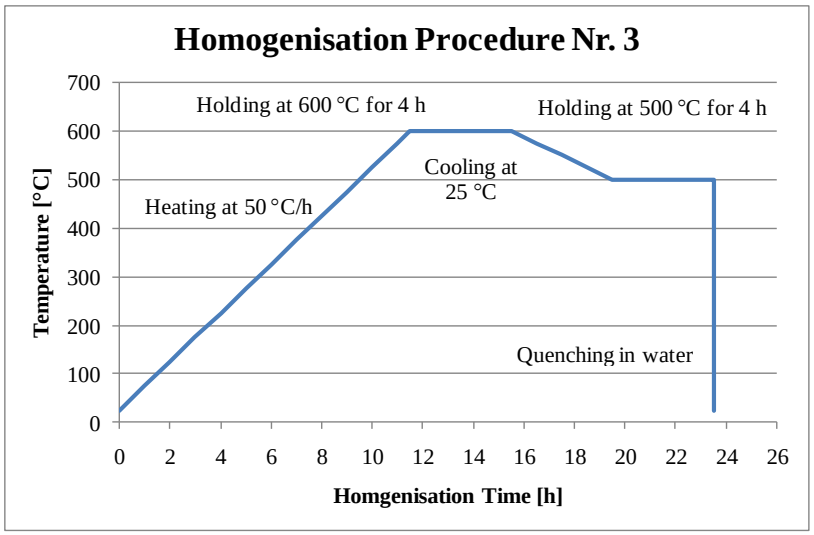

Fig. 3.2: The third homogenization procedure in detail

Fig. 3.3: The oven used for the homogenization procedure

Fig. 3.4: The machine used to perform cold rolling

Cold Rolling of C2

The material has been cut from the extrusion ingots in different initial thicknesses and laboratory cold rolled at NTNU to a thickness of about 1.5 mm, corresponding to equivalent strains of ε = 0.7 and 3. The two different cold rolling procedures are presented in Table 3.3. The cold rolling machine used in this work is presented in Fig. 3.4 above.

Table 3.3: The two different cold rolling procedures

Reduction	Initial thickness	Final thickness [mm]	Strain
50%	3	1.5	ε = 0.7
95%	30	1.5	ε = 3.0

The nine different variants of the C2-alloy after homogenization and cold rolling are presented in Table 3.4.

Table 3.4: The nine different variants of the C2-alloy after the cold rolling

Name	Homogenization procedure	Strain
C2-A1	Nr.1	ε = 0
C2-A2	Nr.1	ε = 0.7
C2-A3	Nr.1	ε = 3.0
C2-B1	Nr.2	ε = 0
C2-B2	Nr.2	ε = 0.7
C2-B3	Nr.2	ε = 3.0
C2-C1	Nr.3	ε = 0
C2-C2	Nr.3	ε = 0.7
C2-C3	Nr.3	ε = 3.0

3.2 Characterization of the Starting Alloy Variants

Alloy variants C2-C1, C2-C2 and C2-C3 were not initially characterized in this work, and any data later used in this work from initial characterization of these three alloy variants are obtained from Gavin Wangs PhD-work [49]. The other six variants of the C2-alloy presented in Table 3.4 were characterized according to the procedures described in the following.

3.2.1 Hardness Measurements

A Vickers hardness instrument, Matsuzawa DVK-1S, with a load of 1 kg, loading speed of 100 μm/s and 15 s loading time was used for the hardness measurements. A picture of the apparatus is presented in Fig. 3.5 below. The measurements were performed on a clean and planar sample surface after grinding the bottom side of the sample planar; to make sure the samples were lying flat in the apparatus. An average of minimum four hardness indentations on each sample of the C2-alloy was measured. All the hardness indentations were measured on the RD-TD-plane. A schematic illustration of a rolled sheet with given directions is presented in Fig. 3.7.

Fig. 3.5: Apparatus used for the hardness measurements

Fig. 3.6: Apparatus used for the electrical conductivity measurements

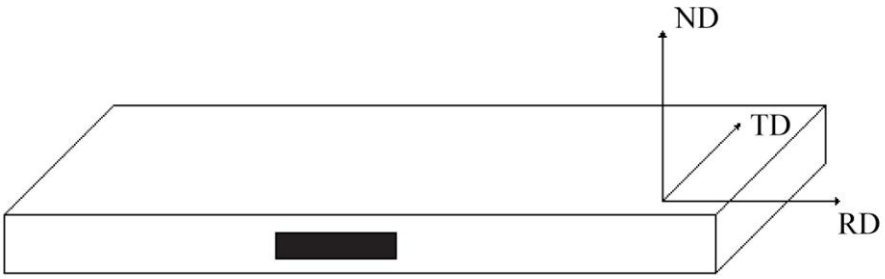

Fig. 3.7: Schematic illustration of a rolled sheet with given directions

3.2.2 Electrical Conductivity Measurements

The electrical conductivity of the six variants of the C2-alloy was measured with a Sigmascope EX8. A picture of the apparatus is presented in Fig. 3.6 above. The measurements were performed by mounting the contact probe on a clean and planar sample surface after grinding the bottom side of the sample planar, to make sure the samples were lying flat in the apparatus. Two measurements were taken on each sample and the two values corresponded for all six samples. The electrical conductivity is a temperature dependent parameter and the measuring equipment was found to be very sensitive to the room temperature. The temperature in the room was measured to be 21 ± 1 °C when the conductivity measurements were taken.

3.2.3 Optical Microscopy

A light optical microscope, Leica MEF4M, was used to investigate the microstructure of C2-A1 and C2-B1 in polarized light with the sub parallel λ-plate inserted. A picture of the microscope is presented in Fig. 3.8 below. Both specimens were investigated in the RD-ND-direction. Pictures were taken at different magnifications. Specimen preparation for the optical microscopy was carried out as shown in Table 3.5.

Table 3.5: Specimen preparation for optical microscopy

Step	Description	Details
1	Embedding	Embedding material: Clarokit
2	Grinding on SiC-paper	Mesh program: 320-500-800-1200-2400
3	Polishing on Al-discs	Polishing program: 6 µm – 3 µm – 1 µm
4	Electro polishing	10 s at 20 V in 20% $HClO_4$ 80% ethanol cooled down to -35 °C (Struers Lectropol-5)
5	Anodizing	100 s ± 40 s in 5% HBF_4 aqueous sol. at 20 V

Between each step of the polishing program the specimens were placed in an ultra sound bath for 30 s to remove loose particles in the surface of the specimens. Pictures of the grinding apparatus, the polishing apparatus, the ultra sound bath, the electro polishing equipment and the anodizing apparatus are presented in Fig. 3.9 – Fig. 3.13 below.

Fig. 3.8: Leica MEF4M

Fig. 3.9: Grinding apparatus

Fig. 3.10: Polishing apparatus

Fig. 3.11: Ultra sound bath

Fig. 3.12: Electro polishing apparatus

Fig. 3.13: Anodizing apparatus

3.3 Annealing Experiments

3.3.1 Isothermal Annealing Procedures

Isothermal annealing experiments with C2-A2, C2-A3, C2-B2 and C2-B3 were carried out by direct immersion into salt-baths at different temperatures. All four variants were annealed at 300°C, 350°C, 400°C, 450°C and 500°C and all the four variants were held at the three different temperatures for 6 different holding times (5 s, 10 s, 100 s, 1000 s, 10000 s and 100000 s) before they were subsequently quenched in water.

3.3.2 Non-Isothermal Annealing Procedures

Non-isothermal annealing experiments were carried out to see if non-isothermal annealing programs could result in significantly different grain structures and textures (different nucleation behavior) than the isothermal annealing programs. The non-isothermal experiments are thoroughly described in the following.

Non-isothermal annealing experiments with C2-A3, C2-B3 and C2-C3 were carried out in a Naberterm N11/R laboratory oven with a C19 program controller. The heating programs, including indications of when samples were taken out of the oven and quenched in water, are presented in Fig. 3.14 – Fig. 3.16. The temperature in the oven was measured by the C19 program controller and with an Amprobe TM45A.

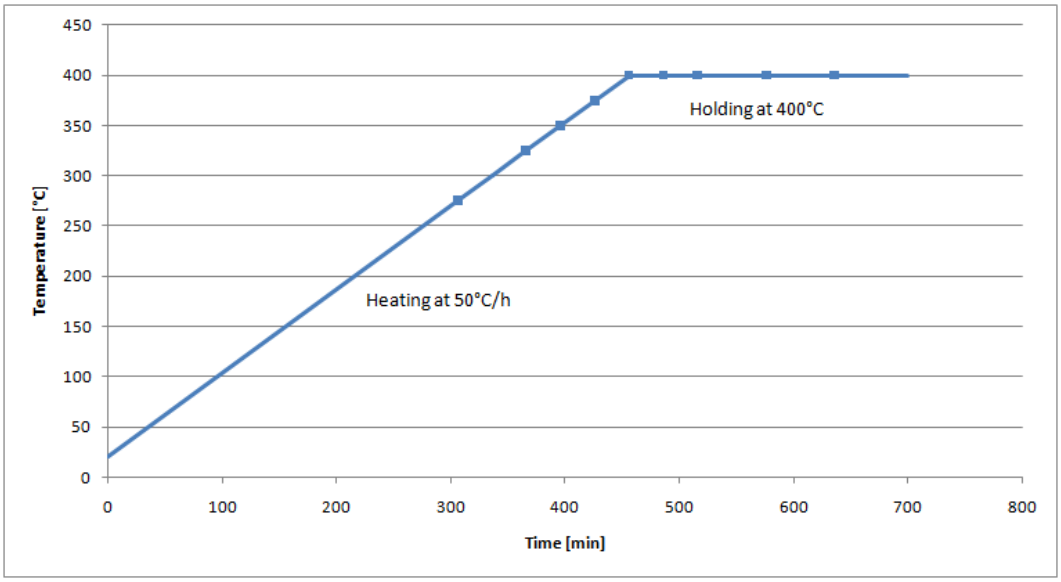

Fig. 3.14: Non-Isothermal annealing program for C2-A3

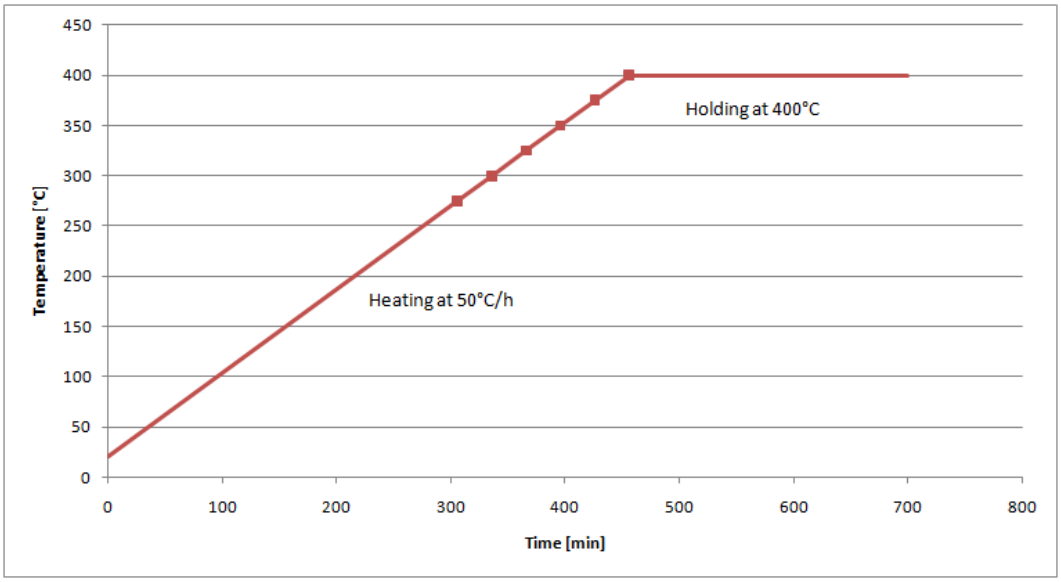

Fig. 3.15: Non-Isothermal annealing program for C2-B3

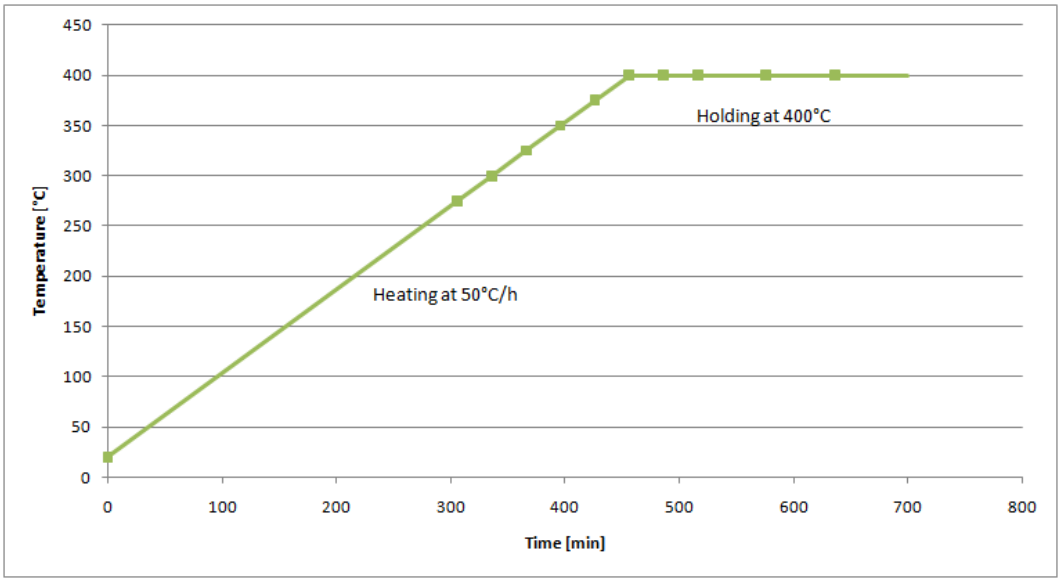

Fig. 3.16: Non-Isothermal annealing program for C2-C3

3.4 Post-Annealing Characterization

3.4.1 Hardness Measurements

The same Vickers hardness instrument as described in Chapter 3.2.1, with a load of 1 kg, loading speed of 100 µm/s and 15 s loading time, was used for the hardness measurements of all the specimens after the annealing experiments. The measurements were performed on a clean and planar sample surface after grinding the bottom side of the sample planar; to make sure the samples were lying flat in the apparatus. An average of minimum four hardness indentations on all specimens was measured. All the hardness indentations were measured on the RD-TD-plane.

3.4.2 Electrical Conductivity Measurements

The electrical conductivity of all the specimens after the annealing experiments was measured with the same apparatus as in Chapter 3.2.2. The measurements were performed by mounting the contact probe on a clean and planar sample surface after grinding the bottom side of the

sample planar, to make sure the samples were lying flat in the apparatus. Two measurements were taken on each sample and the two values corresponded for all samples. The temperature in the room was measured to be 21 ± 1 °C when the conductivity measurements were taken.

3.4.3 Optical Microscopy

A light optical microscope, Leica MEF4M, was used to investigate the microstructure of a selection of the annealed specimens in polarized light with the sub parallel λ-plate inserted. All specimens were investigated in the RD-ND-plane. Pictures were taken at different magnifications. The selection of isothermally annealed specimens that was studied in the optical microscope is presented in Table 3.6. The selection of non-isothermally annealed specimens that was studied in the optical microscope is presented in Table 3.7. Specimen preparation was carried out as presented in Table 3.5.

Table 3.6: The selection of isothermally annealed specimens investigated in the optical microscope

Homogenization	Strain	Annealing Procedure
Nr.1	ε = 0.7	500 °C for 100000 s
Nr.1	ε = 3.0	400 °C for 100000 s
Nr.1	ε = 3.0	450 °C for 100000 s
Nr.1	ε = 3.0	500 °C for 100000 s
Nr.2	ε = 0.7	400 °C for 100000 s
Nr.2	ε = 0.7	450 °C for 100000 s
Nr.2	ε = 0.7	500 °C for 100000 s
Nr.2	ε = 3.0	350 °C for 100000 s
Nr.2	ε = 3.0	400 °C for 100000 s
Nr.2	ε = 3.0	450 °C for 100000 s
Nr.2	ε = 3.0	500 °C for 100000 s

Table 3.7: The selection of non-isothermally annealed specimens investigated in the optical microscope

Homogenization	Strain	Annealing Procedure
Nr.2	ε = 3.0	See Fig. 3.15 – Sample taken out at 375 °C
Nr.2	ε = 3.0	See Fig. 3.15 – Sample taken out at 400 °C

3.4.4 Grain Size Measurements

The grain sizes of all specimens in Table 3.6 (except for nr.1 with strain 0.7 annealed at 500 °C for 10^5 s) and Table 3.7 were measured in both RD- and ND-direction using the linear intercept method on the images taken in the optical microscope (see Chapter 3.4.3). The measurements were performed in Adobe Photoshop CS5 using the "ruler tool". All measurements were performed on photos taken at 10X magnifications, and 10 measurements were performed in both RD- and ND-direction to achieve proper statistics.

3.4.5 TTT-Diagrams

Based on the hardness and conductivity measurements (see Chapter 3.4.1 and 3.4.2) TTT-diagrams were constructed for C2-A2, C2-A3, C2-B2 and C2-B3. The TTT-diagrams were constructed in the following way:

1. Recrystallization was assumed to start after a 25% drop of hardness when the overall hardness was set to be the difference between the as-deformed hardness and the before-deformation hardness. Time to 25% softening and time to complete recrystallization were found from the softening curves.

2. The starting point of precipitation was set to be after a 2.5% increase of conductivity. Knut Sjølstad [8] found this percentage to result in TTT-diagrams predicting microstructures comparable to the actual experimental results.

3.5 Global Texture Measurements

As previously mentioned (see Chapter 2.6) the texture is an important parameter that makes up the characterization of a material together with measurements of grain and sub-grain sizes and misorientations measurements. X-ray diffraction is the conventional method used to determine bulk textures, but the EBSD-technique has also developed into a powerful characterization tool for global texture measurements.

All global texture measurements in this work have been done with a Zeiss Ultra 55 – Limited Edition FESEM equipped with an EBSD-detector. This equipment is presented in Fig. 3.17.

Fig. 3.17: Zeiss Ultra 55 – Limited Edition FESEM equipped with an EBSD-detector

3.5.1 Specimen Preparation for EBSD

All measurements of global textures in this work were performed on specimens prepared according to Table 3.8 below. All specimens were prepared in the RD-ND-plane.

Table 3.8: Specimen preparation for global texture measurements

Step	Description	Details
1	Embedding	Embedding material: Clarokit
2	Grinding on SiC-paper	Mesh program: 320-500-800-1200-2400
3	Polishing on Al-discs	Polishing program: 6 µm – 3 µm – 1 µm
4	Electro polishing	10 s at 20 V in 20% $HClO_4$ 80% ethanol cooled down to -35 °C (Struers Lectropol-5)

3.5.2 FESEM Setup for EBSD

As previously mentioned a Zeiss Ultra 55 – Limited Edition FESEM equipped with an EBSD-detector was used for all measurements of global textures. The operating parameters used for the FESEM are summarized in Table 3.9.

Table 3.9: Operating parameters for FESEM-EBSD

FESEM-Parameter	Value
Acceleration Voltage	20 kV
Working Distance	20 mm
Tilt Angle	70 °
Magnification	40X – 500X

As can be seen from Table 3.9 a range of different magnifications were used. The magnification used for a specific specimen was selected based on the grain size of the specimen and whether or not the specimen was recrystallised, deformed, etc.

3.5.3 EBSD Software Setup

The NORDIF UF-390 software was used to gather the EBSD-patterns during offline-EBSD in the FESEM. The operating parameters used in the NORDIF UF-390 software are summarized in Table 3.10.

Table 3.10: Operating parameters for NORDIF UF-390

Scan Area	
Step size	0.15 – 4 μm
Calibration Settings	
Frame rate	100 fps
Resolution	240 x 240 px
Exposure time	9850 μs
Gain	5
Acquisition Settings	
Frame rate	300 fps
Resolution	96 x 96 px
Exposure time	3183 μs
Gain	2

As can be seen from Table 3.10 a range of different step sizes were used. The step size used for a specific specimen was selected based on the grain size of the specimen and whether or not the specimen was recrystallised, deformed, etc.

3.5.4 Post-Processing of EBSD-data

The EBSD-patterns collected by the NORDIF UF-390 software were indexed in the TSL OIM Data Collection 6 software. The indexed patterns were further post-processed in the OIM Analysis 5.31 software. OIM-maps, pole figures, ODFs and grain size distributions were

produced for all investigated specimens. The post-processing procedure performed in the OIM Analysis 5.31 is described in detail below. A detailed study of the effect of the post-processing procedure was also performed to make sure the post-processing did not affect the quality of the results. The results of this study are presented in Appendix A.

1. The OIM Analysis 5.31 software automatically assumes that all EBSD-maps are maps of the RD-TD plane. Since all EBSD-maps in this work are of the RD-ND-plane; this had to be corrected for in each analysis as a first step.

2. The second step of the post-processing was confidence index (CI) standardization (with default software settings). This is a clean up procedure recommended by the analyzation software producer [50]. This clean up method changes the CIs of all points in a grain to the maximum CI found among all points belonging to the grain. This method is useful when a minimum CI value greater than 0 is used in analyzing the data. It essentially enables a point with a low CI, yet having an orientation similar to that of the surrounding measurements (and thus likely representing a correct indexing of the corresponding EBSP), to be distinguished from a point with a low CI where no correlation exists between the point and its neighbors (most likely representing an incorrect orientation measurement) [50].

3. The next step in the post-processing was grain dilation (with default software settings). Similar to CI standardization, grain dilation is also a clean up procedure recommended by the analyzation software producer [50]. The grain dilation method is an iterative method. The grain dilation only works on points that do not belong to any grains; yet have neighboring points, which do belong to grains. A point may not belong to any grain due to the point either not being indexed or due to it belonging to a grain group having fewer members than the minimum grain size. If the majority of neighbors of a particular point belong to the same grain then the orientation of the particular point is changed to match that of the majority grain – otherwise the orientation is randomly changed to match any of the neighboring points, which belong to grains [50].

4. After the grain dilation clean up, neighbor CI correlation was performed. This clean up method was only performed on data points with CIs less than 0.1. If a particular point has a CI less than the minimum value then the CIs of the nearest neighbors are

checked to find the neighbor with the highest CI. The orientation and CI of the particular point are reassigned to match the orientation and CI of the neighbor with the maximum CI [50].

5. The fifth step of the post-processing was a second grain dilation procedure (with default software settings), recommended by the analyzation software producer [50].

After the fifth step of the post-processing procedure pole figures and ODFs were produced. These results were produced before the sixth and final step of the post-processing procedure since the final step was found to have an effect on the texture results (see Appendix A).

6. The sixth and final step of the post-processing was the single (average) orientation per grain clean up method (with default software settings). In deformed materials, changes in orientation between the individual measurements which constitute a grain are often observed. Some very slight misorientations are also sometimes observed in recrystallized materials. These slight misorientations may arise simply from minute differences in indexing of the patterns from individual measurement points. All measurements, which make up a grain, can be replaced by the average orientation for the grain, which results in the grain having a single orientation at each constituent measurement point [50].

After the sixth and final step of the post-processing procedure OIM-maps and grain size distributions were produced from the analyzation software. As can be seen from Appendix A, the single (average) orientation per grain method had no negative effect on the grain sizes, and improved the colors of the OIM-maps (see Appendix A).

3.5.5 EBSD-scans - Overview

An overview of all performed EBSD-scans in this work including information about magnifications and step sizes are presented in Table 3.11 – Table 3.14 below. Table 3.11

presents all EBSD-scans performed on C2-A3-specimens. Table 3.12 presents all EBSD-scans performed on C2-B2-specimens. Table 3.13 and 3.14 presents all EBSD-scans performed on C2-B3- and C2-C3-specimens.

Table 3.11: An overview of all performed EBSD-scans on C2-A3-specimens

Annealing Procedure	Magnification	Step size [µm]
Isothermal – 400 °C for 10^5 s	40X	4.000
Isothermal – 400 °C for 10^5 s	80X	2.000
Isothermal – 450 °C for 10^5 s	80X	2.000
Isothermal – 500 °C for 10^5 s	80X	3.000
Non-Isothermal – 3 h at 400 °C	80X	2.000

Table 3.12: An overview of all performed EBSD-scans on C2-B2-specimens

Annealing Procedure	Magnification	Step size [µm]
Before Annealing	80X	3.000
Isothermal – 450 °C for 10^5 s	60X	2.000
Isothermal – 500 °C for 10^5 s	90X	2.000

Table 3.13: An overview of all performed EBSD-scans on C2-B3-specimens

Annealing Procedure	Magnification	Step Size [µm]
-	500X	0.180
Isothermal – 350 °C for 10^5 s	80X	4.000
Isothermal – 350 °C for 10^5 s	200X	0.400
Isothermal – 400 °C for 10^5 s	80X	3.000
Isothermal – 400 °C for 10^5 s	200X	0.390
Isothermal – 450 °C for 10^5 s	80X	2.000

Isothermal – 500 °C for 10^5 s	80X	2.000
Non-Isothermal – 375 °C	80X	2.000
Non-Isothermal – 375 °C	200X	0.375
Non-Isothermal – 400 °C	80X	3.000
Non-Isothermal – 400 °C	200X	0.375

Table 3.14: An overview of all performed EBSD-scans on C2-C3-specimens

Annealing Procedure	Magnifications	Step Size [µm]
Non-Isothermal – 2 h at 400 °C	80X	2.000
Non-Isothermal – 3 h at 400 °C	80X	2.000

4. Experimental Results

The following chapter is divided into three parts, where the first part contains the experimental results obtained during the initial characterization of the different variants of the C2-alloy (see Chapter 3.1). The results from the isothermal annealing experiments (including softening curves, EC curves, grain size measurements, TTT-diagrams, OM-images, texture results, etc.) are presented in the second part of this chapter, while the softening curves, OM-images, EC curves, grain size measurements and texture results from the non-isothermal annealing experiments are presented in the third and final part of this chapter.

As mentioned in both Chapter 1 and Chapter 3, this work is directly based on, and an extension of my TMT4500-work [1]. Due to this fact some of the results from the TMT4500-work are presented in this chapter for completeness and for comparison reasons. These results include:

- The HV- and EC results for C2-A1, C2-A2, C2-A3, C2-B1, C1-B2 and C2-B3 presented in Table 4.1 in Chapter 4.1.1.
- The calculations of the amounts of Mn in solid solution for C2-A1 and C1-B1 presented in Table 4.2 in Chapter 4.1.2.
- All HV results presented in Chapter 4.2.1 for specimens isothermally annealed at 300 °C, 350 °C and 400 °C.
- All EC results presented in Chapter 4.2.2 for specimens isothermally annealed at 300 °C, 350 °C and 400 °C.

General descriptions of all the experimental results will be presented in this chapter. All discussions of the results are contained to Chapter 5.

4.1 Characterization of the Starting Alloy Variants

The experimental results obtained during the characterizations described in Chapter 3.2 are presented in the following. Texture results from the texture measurements on the starting C2-alloy variants described in Chapter 3.5 are also included in this chapter. The results from the optical microscope studies of the starting C2-alloy variants described in Chapter 3.2.3 are presented in Appendix E.

4.1.1 Electrical Conductivity- and Hardness Measurements

The results from the electrical conductivity measurements and hardness measurements described in Chapter 3.2.1 and 3.2.2 are presented in Table 4.1.

Table 4.1: Measured EC and HV values of the starting variants (homogenized and deformed) of the C2-alloy

Name	Hom. Proc.	Strain	EC [m/Ω mm^2]	HV
C2-A1	Nr.1	ε = 0	17.5	37.0
C2-A2	Nr.1	ε = 0.7	17.5	58.5
C2-A3	Nr.1	ε = 3.0	17.6	71.5
C2-B1	Nr.2	ε = 0	21.5	30.2
C2-B2	Nr.2	ε = 0.7	22.0	51.9
C2-B3	Nr.2	ε = 3.0	21.9	61.3
C2-C1	Nr.3	ε = 0	22.5	37.9
C2-C3	Nr.3	ε = 3.0	23.5	56.1

As can be seen from Table 4.1 the different degrees of deformation have little or no effect on the electrical conductivity for the first two homogenization variants, while the electrical conductivity increase from 22.5 to 23.5 for the third variant. Both homogenization procedure nr. 2 and nr. 3 increase the conductivity compared to the as cast material. The hardness increases substantially with increasing strain for all three variants. The measured increase in

hardness with increasing strain is largest for the as cast material (35 Vickers) and smallest for the nr. 3 variant (18 Vickers). The hardness of the unstrained alloy is reduced from 37.0 to 30.2 (C2-A1 to C2-B1) with homogenization procedure nr. 2, while the hardness of the unstrained alloy seems relatively unaffected by homogenization procedure nr. 3.

4.1.2 Amounts of Manganese in Solid Solution

By using the Matthiessens rule (Equation 2.11 in Chapter 2.7.2) and the results from the electrical conductivity measurements (see Table 4.1 in Chapter 4.1.1) a rough estimation of the manganese in solid solution for the three different homogenization variants of the C2-alloy were calculated. The results from these estimations are presented in Table 4.2, and a calculation example can be found in Appendix B.

Table 4.2: Estimations of the wt% Mn in solid solution

Name	Hom. Proc.	Strain	EC [m/Ωmm^2]	Mn in ss [wt%]
C2-A1	Nr.1	$\varepsilon = 0$	17.5	≈ 0.85
C2-B1	Nr.2	$\varepsilon = 0$	21.5	≈ 0.55
C2-C1	Nr.3	$\varepsilon = 0$	22.5	≈ 0.49

One of the primary goals of homogenization of 3xxx-alloys is to reduce the level of Mn in solid solution (see Chapter 2.3), and as can be seen from Table 4.2 both homogenization procedures reduce the wt% of manganese in solid solution. The reduction seems to be largest for homogenization procedure nr. 3. The values in Table 4.2 are only rough estimations. More sophisticated methods have been used to calculate the same values, which resulted in values of 0.69 wt%, 0.35 wt% and 0.23 wt% for C2-A1, C2-B1 and C2-C1 respectively [51]. All values significantly lower than the rough estimations presented in Table 4.2. The estimations in Table 4.2 still give an indication of the difference in Mn in solid solution content between the different alloy variants.

4.1.3 Texture Results

The results from the texture measurements on starting C2-alloy variants described in Chapter 3.5 are presented in the following. These measurements were performed to characterize the deformation texture introduced to the C2-alloy due to cold rolling. The textures of specimens C2-B2 and C2-B3 were investigated. Fig. 4.1 – Fig. 4.3 shows the OIM-map, the ODF and the pole figure for C2-B2, while Fig. 4.4 – Fig. 4.6 shows the OIM-map, the ODF and the pole figure for C2-B3.

The OIM-maps in Fig. 4.1 and Fig. 4.4 clearly show the development of the deformation structure introduced with cold rolling, where elongated grains in the direction of applied strain is the most obvious "macro" feature along with grain fragmentation at $\varepsilon = 3.0$. Correspondingly the pole figures in Fig. 4.3 and Fig. 4.6 show the development of a typical cold rolling texture in an FCC-metal. The development of a typical cold rolling texture can also be seen in the ODFs in Fig. 4.2 and Fig. 4.4 where strong Copper-, Brass- and S components dominates. A typical cold rolling ODF for an FCC-metal with highlighted deformation texture components is presented in Fig. 2.19 in Chapter 2.6.1 for comparison reasons.

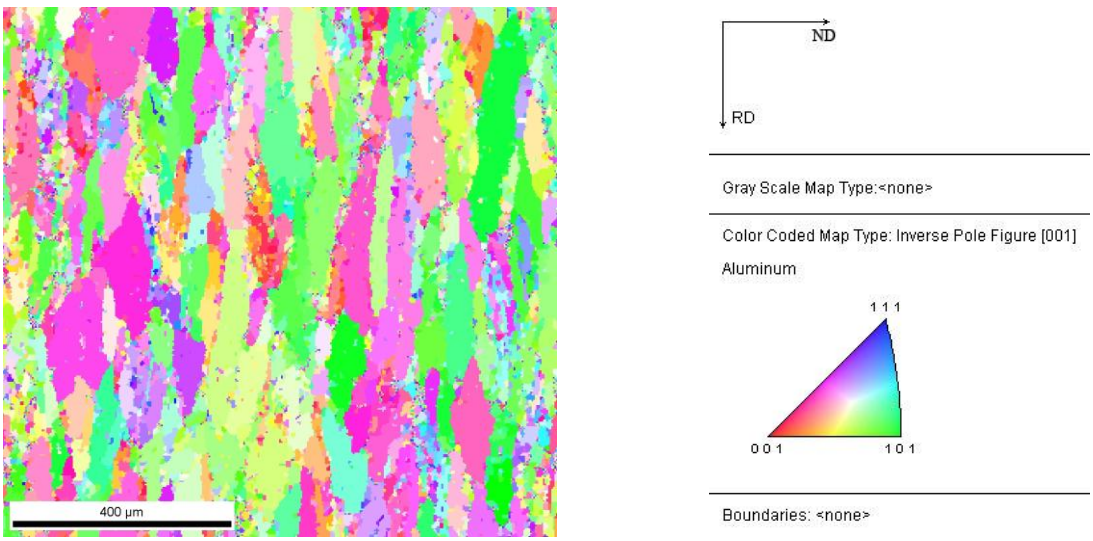

Fig. 4.1: OIM-map from a 80X EBSD-scan of C2-B2

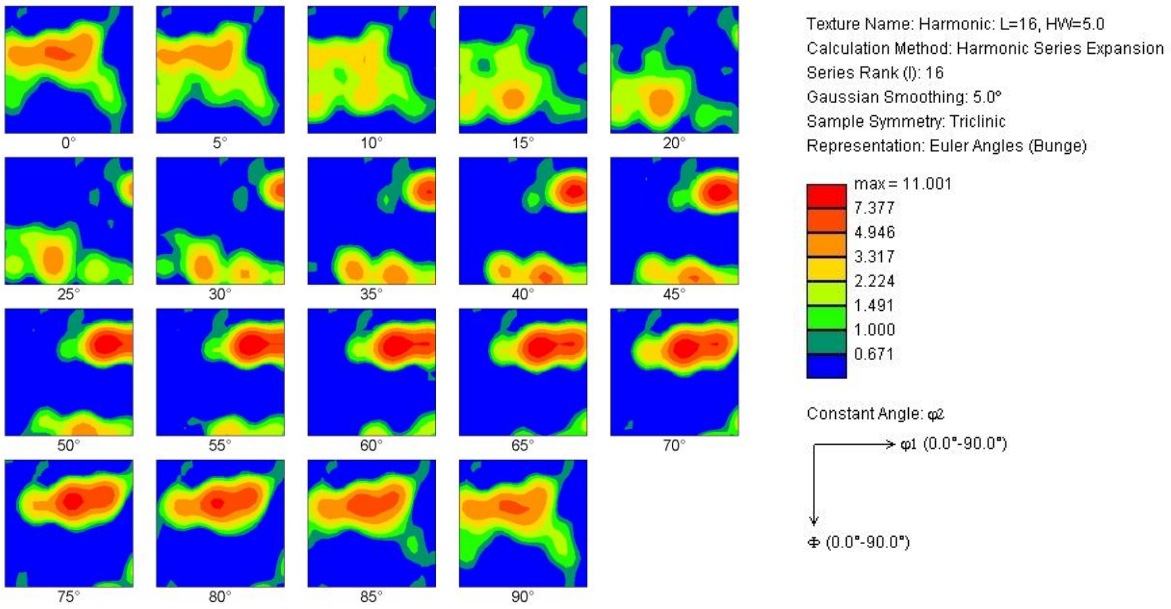

Fig. 4.2: ODF from a 80X EBSD-scan of C2-B2

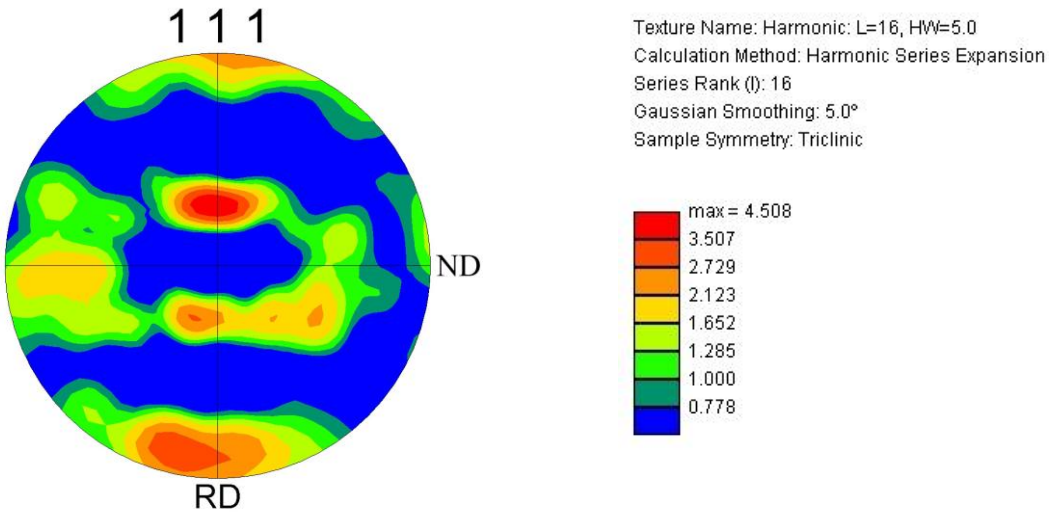

Fig. 4.3: Pole figure from a 80X EBSD-scan of C2-B2

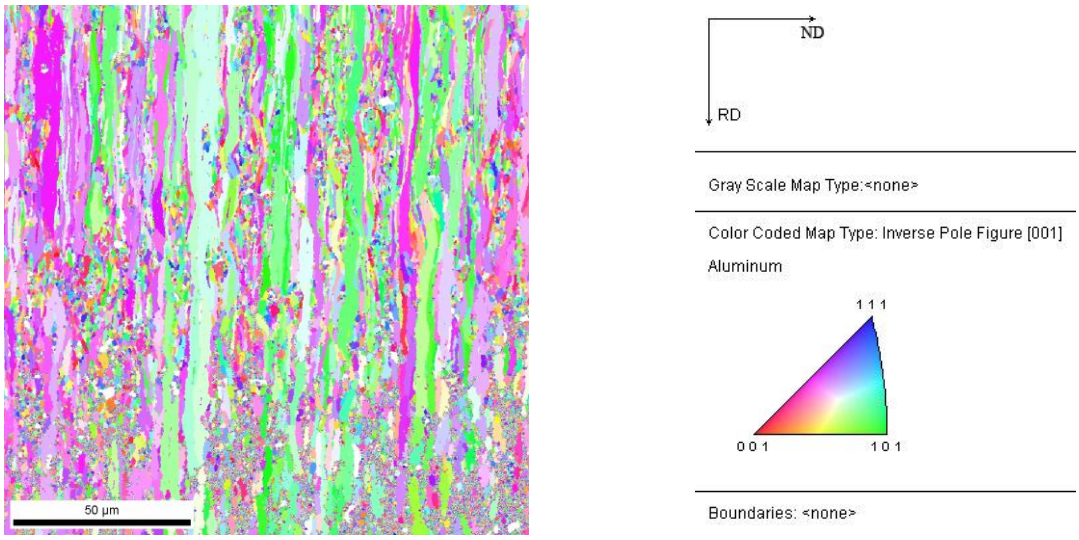

Fig. 4.4: OIM-map from a 500X EBSD-scan of C2-B3

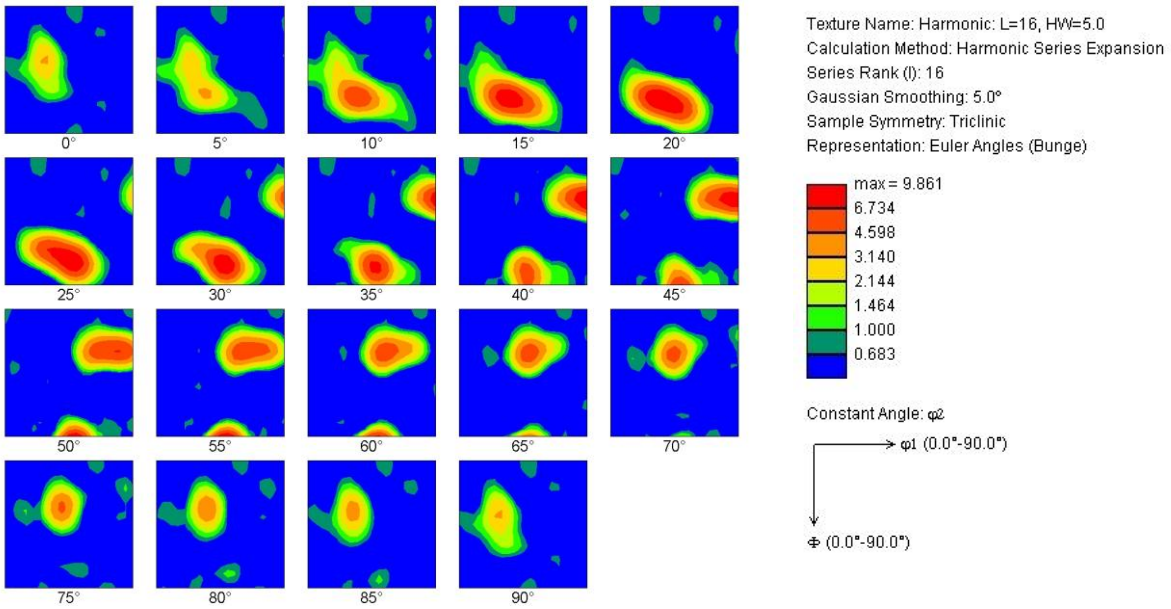

Fig. 4.5: ODF from a 500X EBSD-scan of C2-B3

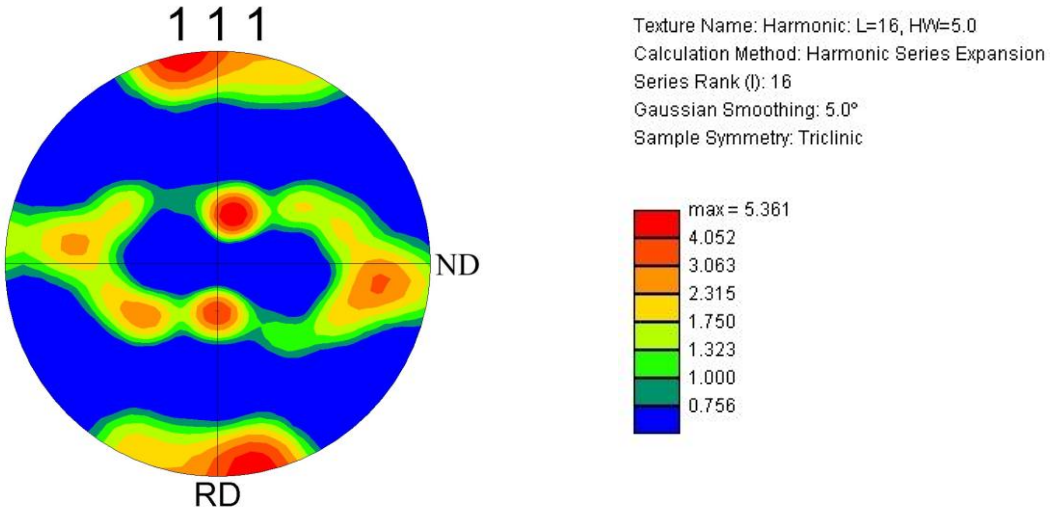

Fig. 4.6: Pole figure from a 500X EBSD-scan of C2-B3

4.2 Isothermal Annealing Experiments

The experimental results from the isothermal annealing experiments and the post-annealing characterization described in Chapter 3.3 and Chapter 3.4 are presented in this chapter. Also included in this chapter are the texture results from the texture measurements on the isothermally annealed specimens described in Chapter 3.5.

4.2.1 Softening Curves

Softening curves for C2-A2, C2-A3, C2-B2 and C2-B3 showing the hardness development during the isothermal annealing experiments described in Chapter 3.3 are presented in Fig. 4.7 – Fig. 4.10. The softening curves are presented as HV vs. annealing time plots. HV-values from the initial characterization (Table 4.1) of the C2-alloy variants are also included in the respective plots for comparison reasons.

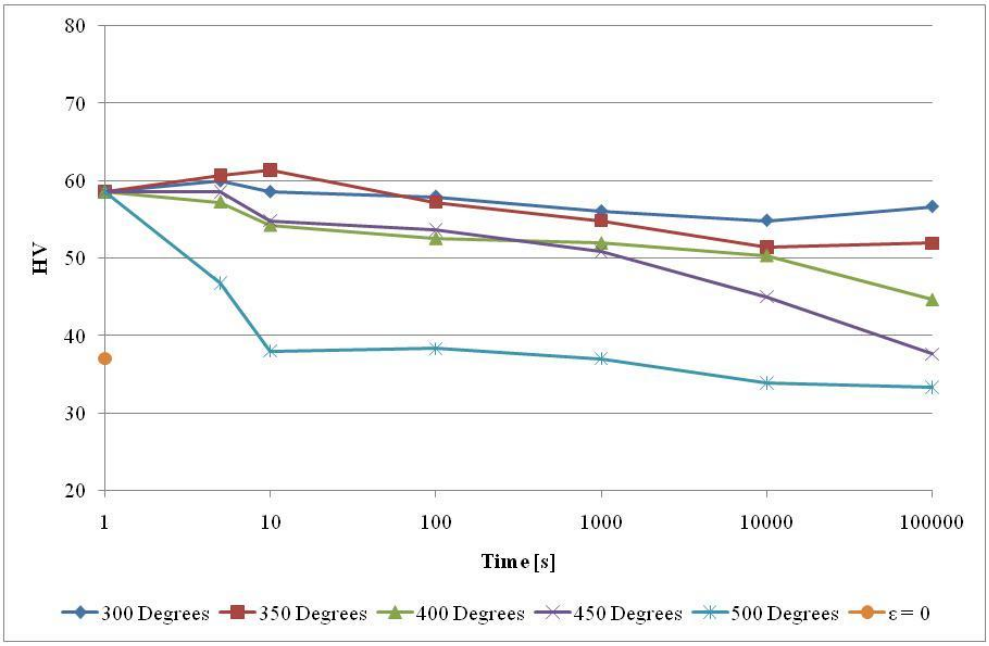

Fig. 4.7: Softening curve for C2-A2 (as cast – ε = 0.7)

By studying Fig. 4.7 above only small and relatively slow reductions of the hardness can be seen for the four lowest annealing temperatures and their respective curves, corresponding to typical recovery behavior (see Chapter 2.5). The hardness reduction increases with increasing annealing temperature, this since dislocations rearrange faster at higher temperatures (see Chapter 2.5.2). The curve for the highest annealing temperature (500 °C) show a large HV reduction early in the annealing and a subsequent leveling of the HV curve, corresponding to typical recrystallization behavior (see Chapter 2.5). The HV reduction increases towards the end of the annealing at both 400 °C and 450 °C possibly indicating a starting recrystallization. The small increase in HV at the end of the annealing procedure at 300 °C and 350 °C is probably due to measurement errors. A small increase in hardness can also be seen early in the softening curves for the annealing at 300 °C, 350 °C and 450 °C.

It can be seen from Fig. 4.8 below that the softening curves for 300 °C and 350 °C show the slow and steady decrease in hardness typical for recovery (see Chapter 2.5). As for C2-A2, the hardness reduction is larger with increasing annealing temperature. The curve representing the annealing at 400 °C also shows slow and steady reduction of hardness typical for recovery until around 1000 s at the annealing temperature. After 1000 s at 400 °C a large reduction of

the hardness typical for recrystallization occurs (see Chapter 2.5), before the softening curve levels out. The two highest annealing temperatures (450 °C and 500 °C) and their curves show a large HV reduction early in the annealing and a subsequent leveling of the curve, corresponding to typical recrystallization behavior (see Chapter 2.5). A relatively small increase in HV can be observed early in the softening curves for the annealing procedures at 300 °C and 350 °C.

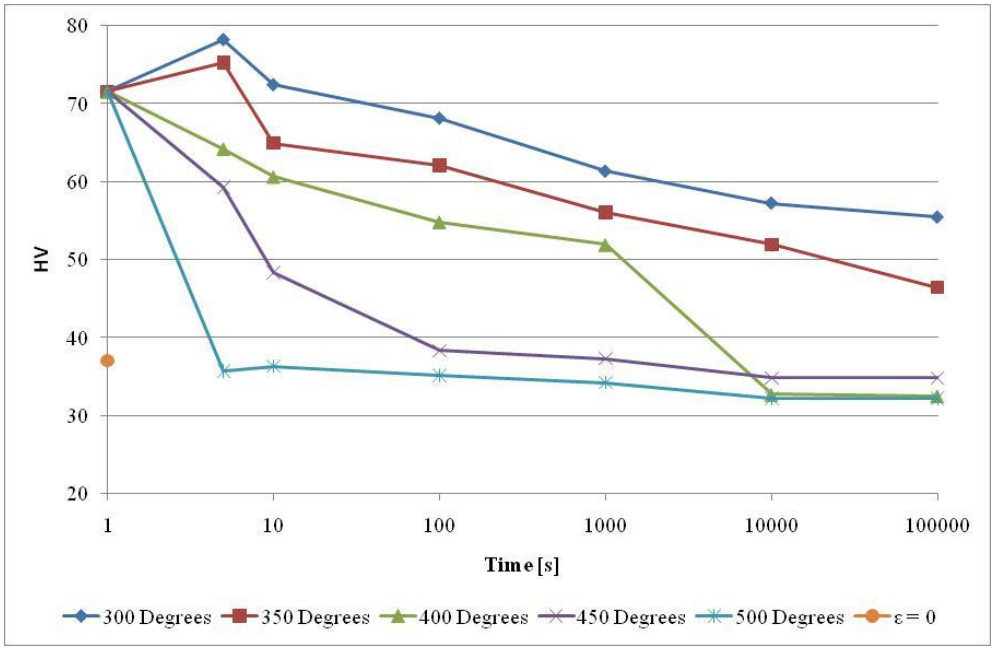

Fig. 4.8: Softening curve for C2-A3 (as cast – ε = 3.0)

The softening curves for 300 °C and 350 °C in Fig. 4.9 below show the slow and steady decrease in hardness typical for recovery (see Chapter 2.5). As for C2-A2 and C2-A3, the hardness reduction increases with increasing annealing temperature. The three highest annealing temperatures (400 °C, 450 °C and 500 °C) and their curves show a large HV reduction early in the annealing procedure and a subsequent leveling of the softening curve, corresponding to typical recrystallization behavior (see Chapter 2.5). As can be seen in Fig. 4.9, the large reduction in HV just mentioned occurs earlier in the annealing procedure with increasing temperature, this due to the fact that dislocations rearrange faster at higher temperatures (see Chapter 2.5.2). A relatively small increase in HV can be observed early in the softening curve for the annealing procedure at 300 °C.

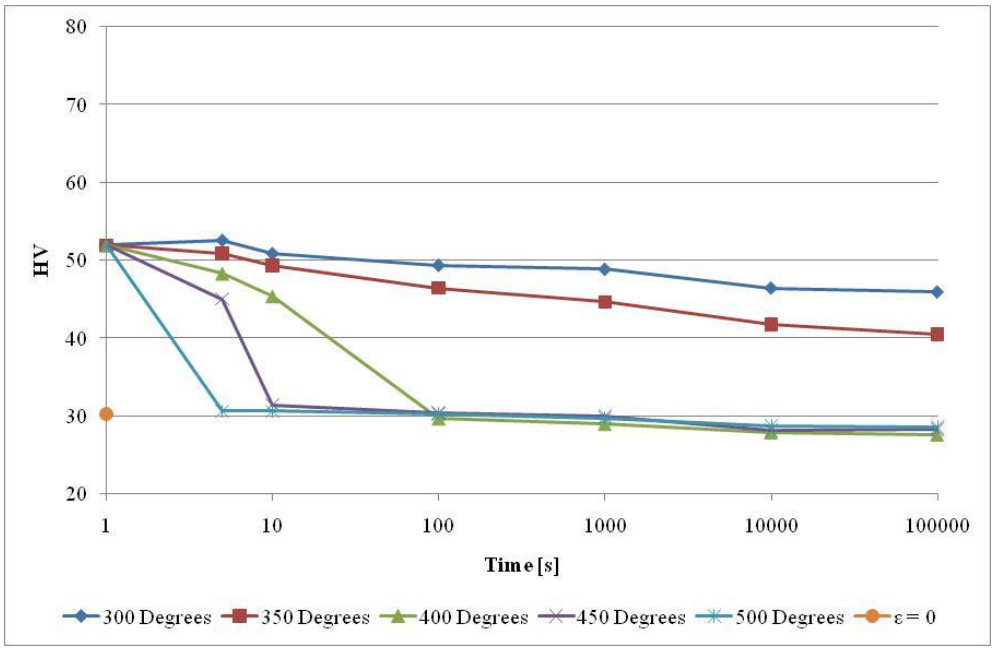

Fig. 4.9: Softening curve for C2-B2 (hom. nr. 2 – ε = 0.7)

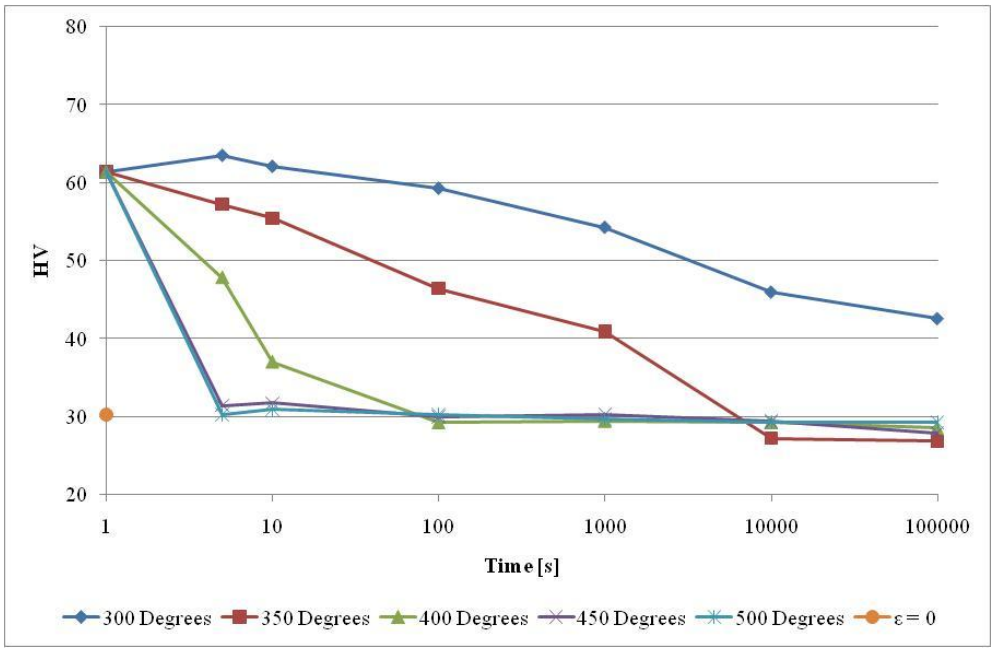

Fig. 4.10: Softening curve for C2-B3 (hom. nr. 2 – ε = 3.0)

It can be seen from Fig. 4.10 above that the softening curve for 300 °C shows the slow and steady decrease in hardness typical for recovery (see Chapter 2.5). As for C2-A2, C2-A3 and C2-B2, the hardness reduction increases with increasing annealing temperature due to

dislocations rearranging faster at higher temperatures (see Chapter 2.5.2). The curve representing the annealing at 350 °C shows a relatively fast but steady reduction of hardness (recovery) until around 1000 s at the annealing temperature. After 1000 s at 350 °C a large reduction of the hardness that is typical for recrystallization occurs (see Chapter 2.5), before the softening curve levels out. The three highest annealing temperatures (400 °C, 450 °C and 500 °C) and their curves show a large HV reduction early in the annealing procedure and a subsequent leveling of the curve, corresponding to typical recrystallization behavior (see Chapter 2.5). As can be seen in Fig. 4.10 the large reduction in HV just mentioned occurs earlier in the annealing procedure with increasing temperature, as for C2-B2. A relatively small increase in HV can be observed early in the softening curve for the annealing procedure at 300 °C.

4.2.2 Electrical Conductivity Measurements

Electrical conductivity curves for C2-A2, C2-A3, C2-B2 and C2-B3 showing the electrical conductivity development during the isothermal annealing experiments, described in Chapter 3.3, are presented in Fig. 4.11 – Fig. 4.14. The curves are presented as EC vs. annealing time plots. EC values from the initial characterization (Table 4.1) of the C2-alloy variants are also included in the respective plots for comparison reasons.

Manganese in solid solution distorts the atomic lattice of the alloy and consequently lowers the conductivity (see Chapter 2.7.2). Because of this, the development in electrical conductivity during annealing will be a good indication of the amount of precipitation during annealing (see Chapter 2.5.1); i.e. since the amount of manganese in solid solution is reduced during precipitation. This means that the clearly increasing conductivity of C2-A2 during the different annealing procedures indicates considerable precipitation. The slope of the EC curve representing the annealing at 500 °C is changing significantly several times early in the annealing procedure. By comparing Fig. 4.11 to the softening curve for C2-A2 in Fig. 4.7 the varying EC slope can be related to the significant softening early in the annealing at 500 °C. After 10000 seconds of annealing the slope of the EC curve for the annealing at 450 °C is slightly reduced. The final trend after 100000 seconds seems to be that the electrical conductivity increases with annealing temperature up to 400 °C. Annealing at 450 °C results

in a slightly reduced conductivity increase compared to annealing at 400 °C. Annealing at 500 °C results in a largely reduced conductivity increase compared to the annealing at 400 °C.

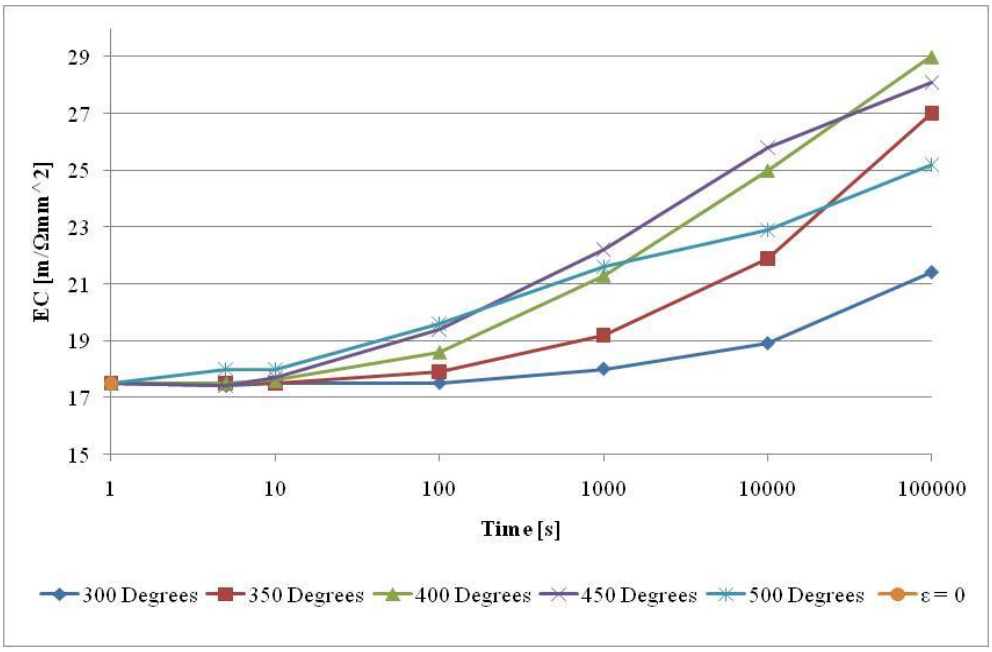

Fig. 4.11: EC curve for C2-A2 (as cast – ε = 0.7)

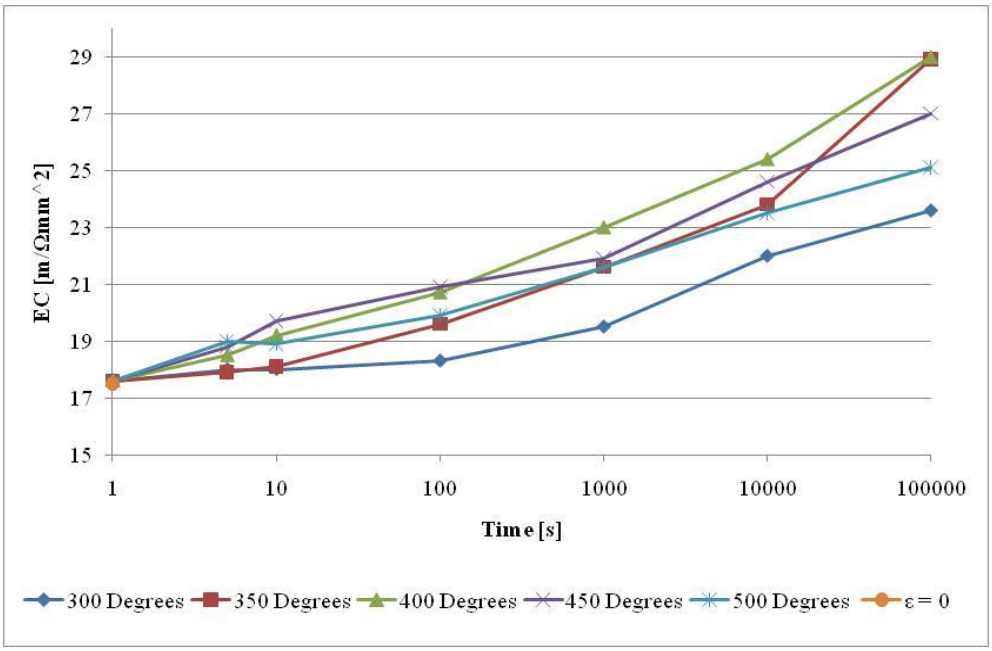

Fig. 4.12: EC curve for C2-A3 (as cast – ε = 3.0)

As for C2-A2, the EC curves for C2-A3 in Fig. 4.12 indicate considerable precipitation. And as for C2-A2, the final trend after 100000 seconds seems to be that the electrical conductivity for C2-A3 increases with annealing temperature up to 400 °C. Annealing at 450 °C results in a slightly reduced conductivity increase compared to the annealing at 400 °C. Annealing at 500 °C results in a largely reduced conductivity increase compared to the annealing at 400 °C. By studying Fig. 4.12 one can also see that the slope of the EC curve for the annealing at 500 °C is reduced after 5 seconds of annealing. By comparing Fig. 4.12 to the softening curve for C2-A3 in Fig. 4.8, the reduced EC slope can be related to the significant softening early in the annealing at 500 °C. The varying slope of the 450 °C EC curve can be explained in the same manner. The increase in conductivity during annealing of C2-A3 occurs faster and to a larger degree compared to C2-A2.

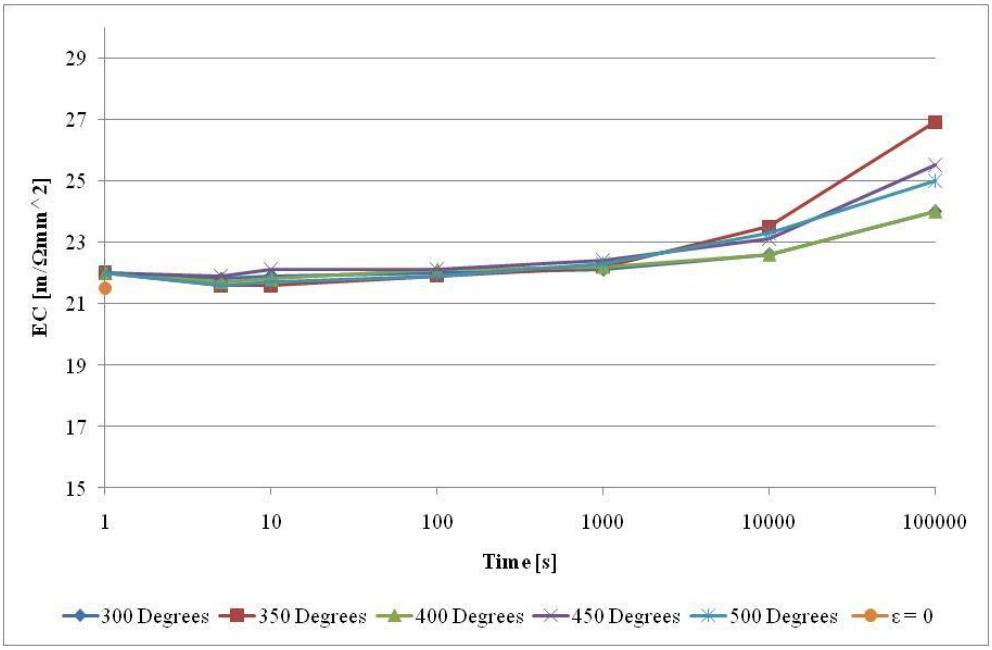

Fig. 4.13: EC curve for C2-B2 (hom. nr. 2 – ε = 0.7)

By studying Fig. 4.13 no clear development in the EC curves can be observed before towards the end of the annealing procedures. The increase in the conductivity observed for C2-B2 is both smaller and occurring slower than for C2-A2 and C2-A3, indicating less precipitation for C2-B2 during annealing. No general trends in the results are observed when studying the EC plot for C2-B2 alone or when the EC plot is compared with the softening curves for C2-B2 in

Fig. 4.9. The smallest conductivity increases occurred for the annealing at 300 °C and 400 °C while the annealing at 350 °C resulted in the highest final conductivity.

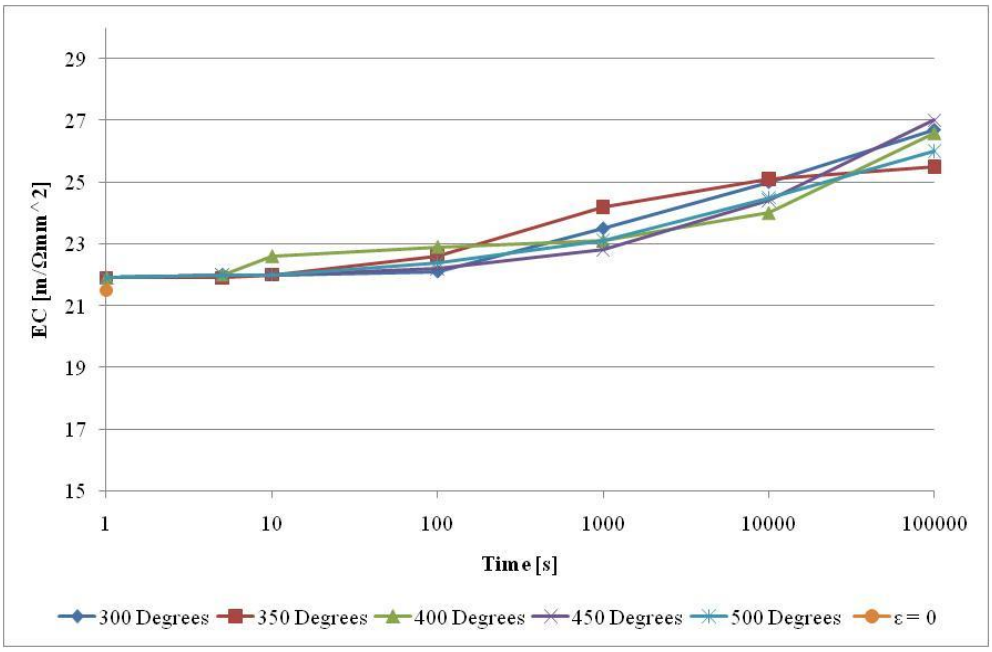

Fig. 4.14: EC curve for C2-B3 (hom. nr. 2 – ε = 3.0)

The increase in the conductivity observed for C2-B3 is, as for C2-B2, both smaller and occurring slower than for C2-A2 and C2-A3, indicating less precipitation for C2-B2 during annealing. The increase in conductivity during annealing of C2-B3 occurs faster and to a larger degree compared to C2-B2. No general trends in the results are observed when studying the EC plot for C2-B3 alone, but when comparing the EC plot of C2-B3 with the softening curves for C2-B3 in Fig. 4.10 some trends can be seen. Precipitation seems to occur after completed recrystallization for the annealing at 400 °C, 450 °C and 500 °C. The slope of the EC curve is reduced at the start of recrystallization for the annealing at 350 °C. Both the softening (recovery) and the precipitation increase in magnitude after 100 s of annealing at 300 °C. The smallest final conductivity increase occurred for the annealing at 350 °C, while the annealing at 300 °C, 400 °C and 450 °C resulted in the highest final conductivities.

4.2.3 TTT-Diagrams

Based on the hardness and conductivity measurements presented in the two previous chapters TTT-diagrams were constructed for C2-A2, C2-A3, C2-B2 and C2-B3 as described in Chapter 3.4.5. These TTT-diagrams are presented in Fig. 4.15 – Fig. 4.18.

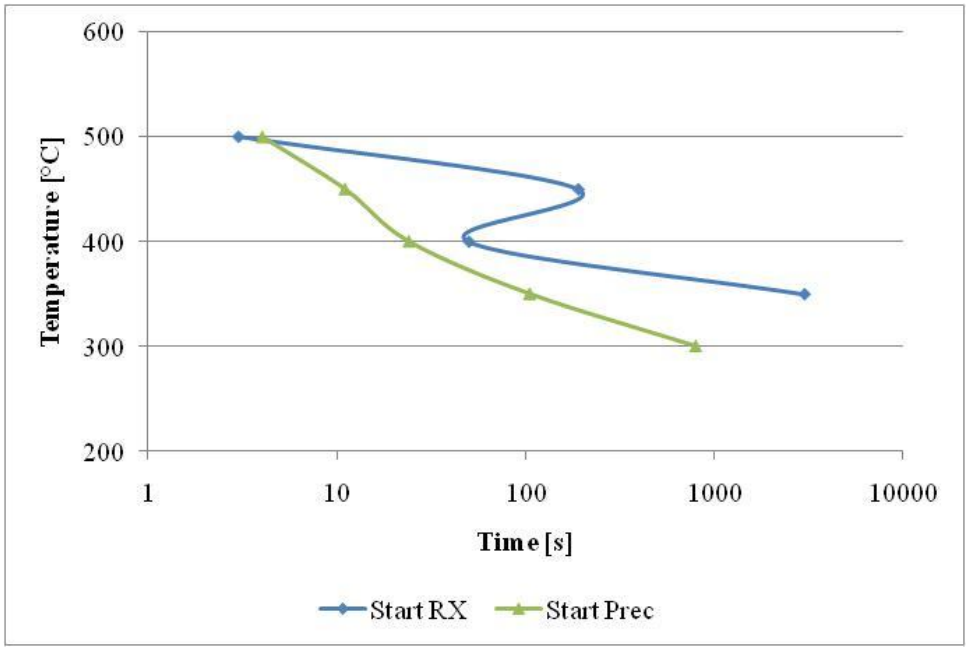

Fig. 4.15: TTT-diagram for C2-A2 (as cast – ε = 0.7)

In Fig. 4.15 and Fig. 4.16 the effect of strain can clearly be seen since both the recrystallization process and the precipitation process are promoted with increasing strain. As an example the precipitation for C2-A3 (ε = 3.0) at 350 °C seems to be starting after approximately 10 seconds of annealing, while for C2-A2 (ε = 0.7) the precipitation starts after 100 seconds of annealing at 350 °C. In Fig. 4.15 and 4.16 the precipitation process is also observed to shift the start and end of the recrystallization process to longer annealing times when precipitation occurs simultaneously or previous to recrystallization.

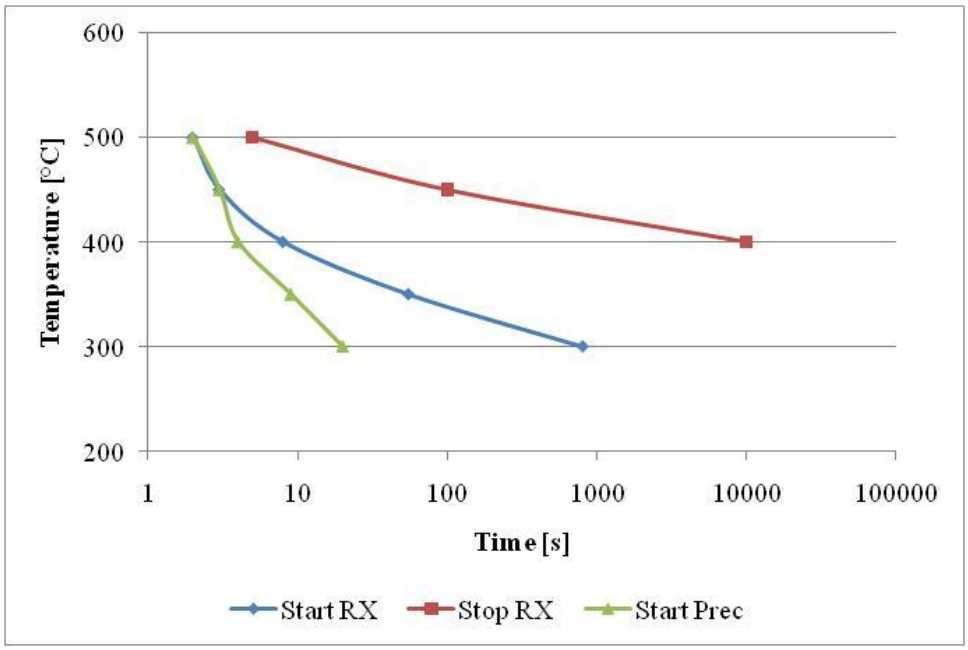

Fig. 4.16: TTT-diagram for C2-A3 (as cast – ε = 3.0)

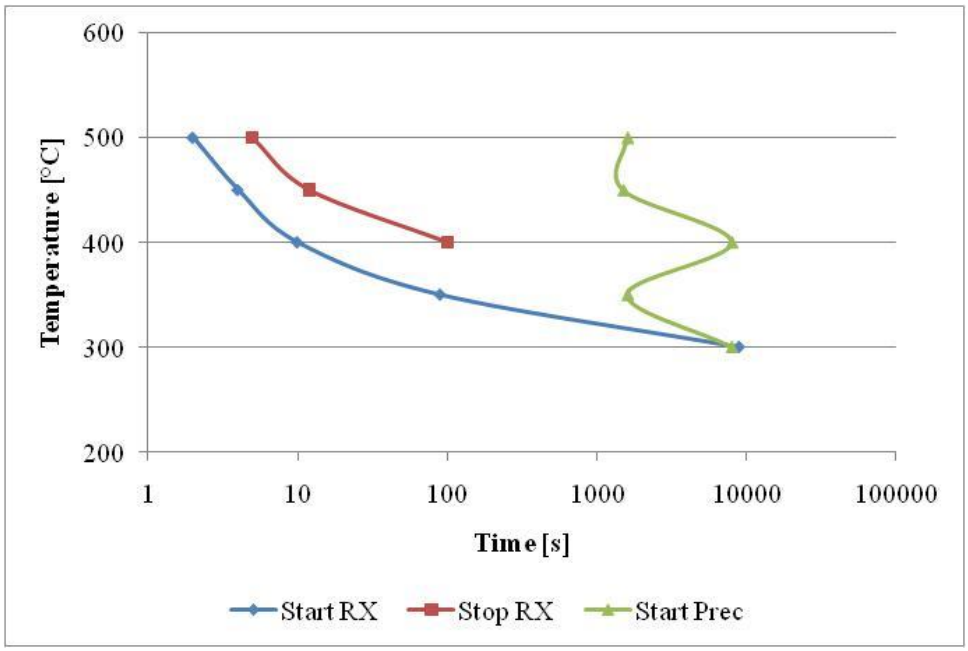

Fig. 4.17: TTT-diagram for C2-B2 (hom. nr.2 – ε = 0.7)

The effect of strain is also obvious in Fig. 4.17 and Fig 4.18 since both the recrystallization process and the precipitation process are promoted with increasing strain. As an example the precipitation for C2-B3 (ε = 3.0) at 500 °C seems to be starting after approximately 100

seconds of annealing, while for C2-B2 (ε = 0.7) the precipitation at 500 °C starts after over 1000 seconds of annealing. Further, the effect of homogenization procedure nr. 2 can clearly be seen in Fig. 4.15 – Fig. 4.18. Both the start and end of the recrystallization process have been moved to shorter annealing times for the hom. proc. nr. 2 variants in Fig. 4.17 and Fig. 4.18 compared to the as cast variants in Fig. 4.15 and Fig. 4.16. In addition the start of the precipitation process has been moved to significantly longer annealing times for both the hom nr. 2 variants compared to the as cast variants. Both as cast variants seems to be affected by precipitation for all annealing temperatures, while C2-B2 is not affected by precipitation above 350 °C, and C2-B3 is not affected by precipitation above 400 °C.

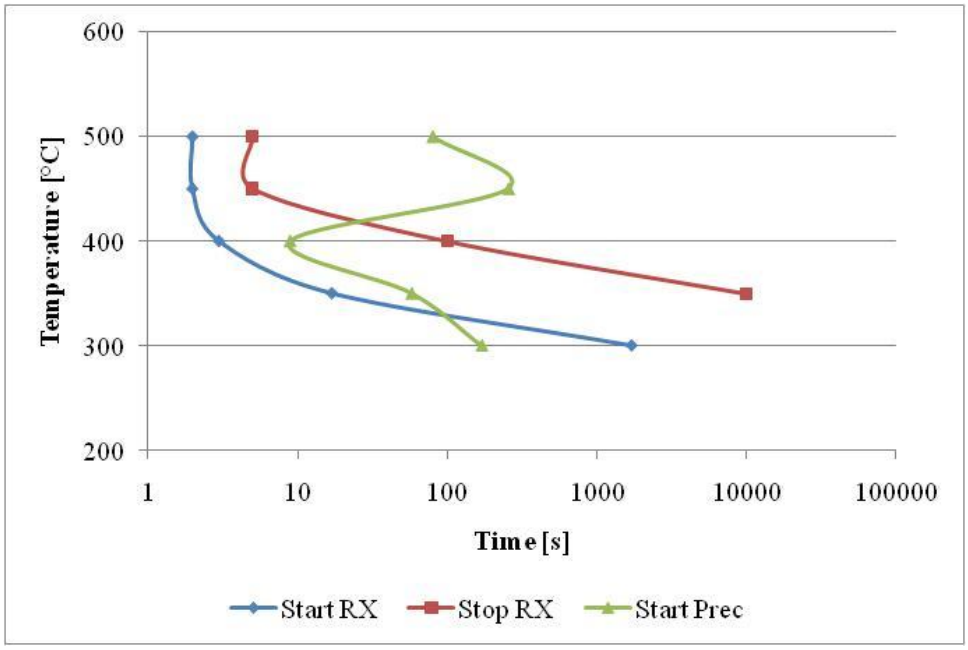

Fig. 4.18: TTT-diagram for C2-B3 (hom. nr.2 – ε = 3.0)

4.2.4 Optical Microscope Images

The optical microscope images of the selection of isothermally annealed specimens listed in Table 3.6 in Chapter 3.4.3 are presented in Fig. 4.19 – Fig. 4.29 below. The selection of specimens that was looked at was chosen based on the softening curve results presented in Chapter 4.2.1. All selected specimens were expected to be recrystallised.

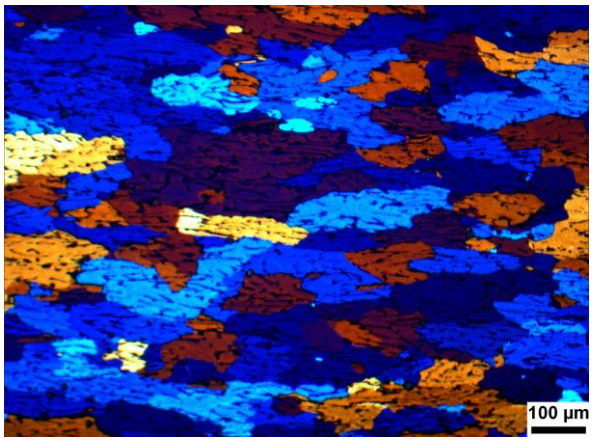

Fig. 4.19: OM-image of C2-A2 annealed at 500 °C for 10^5 s

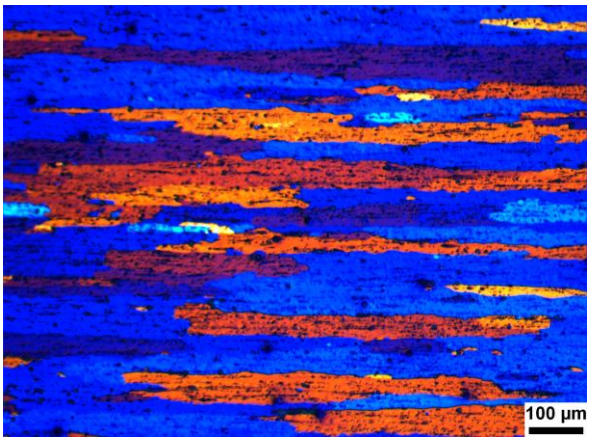

Fig. 4.20: OM-image of C2-A3 annealed at 400 °C for 10^5 s

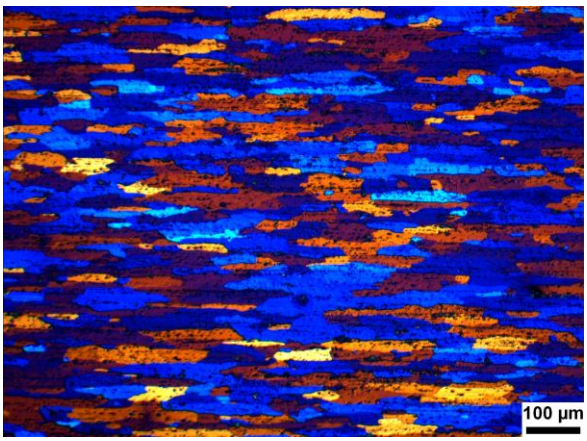

Fig. 4.21: OM-image of C2-A3 annealed at 450 °C for 10^5 s

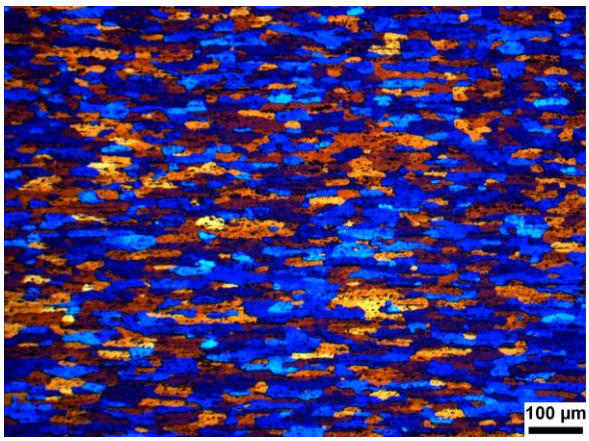

Fig. 4.22: OM-image of C2-A3 annealed at 500 °C for 10^5 s

The OM-image in Fig. 4.19 show a grain structure very similar to a slightly deformed grain structure, and the image reveals that C2-A2 annealed at 500 °C for 10^5 s was not recrystallised. Due to this no further measurements were conducted on this specimen. Fig. 4.20 – Fig. 4.22 show C2-A3 annealed at increasing temperatures. All three figures show recrystallised specimens, where the grain size is gradually reduced with increasing temperature.

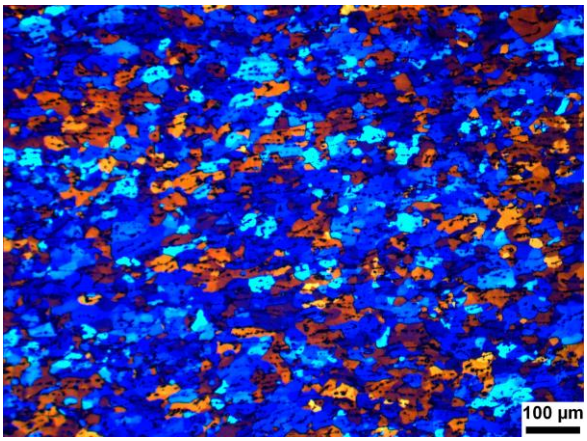

Fig. 4.23: OM-image of C2-B2 annealed at 400 °C for 10^5 s

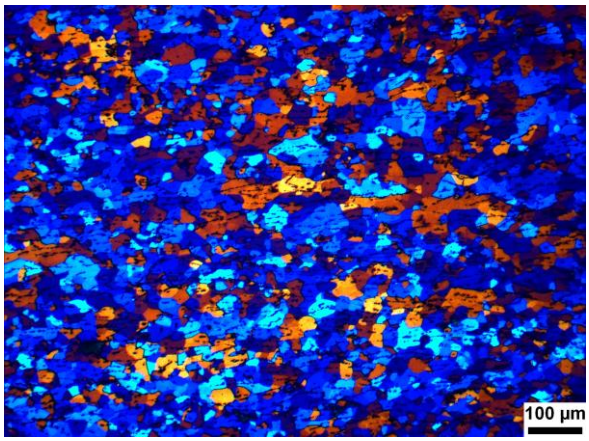

Fig. 4.24: OM-image of C2-B2 annealed at 450 °C for 10^5 s

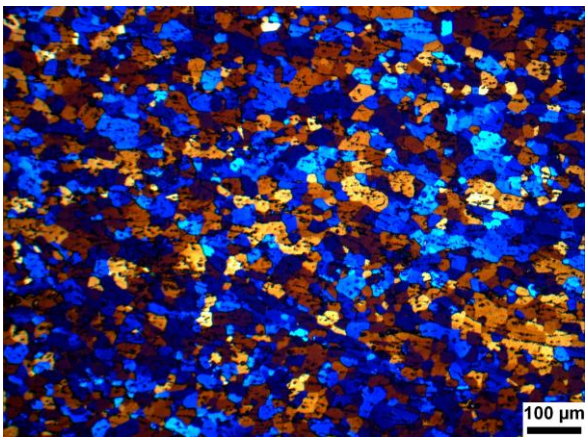

Fig. 4.25: OM-image of C2-B2 annealed at 500 °C for 10^5 s

Fig. 4.23 – Fig. 4.25 show C2-B2 annealed at increasing temperatures. All three figures show recrystallised specimens, where the increasing temperature seems to have had little effect since no large differences can be seen in the grain structures based on the OM-images.

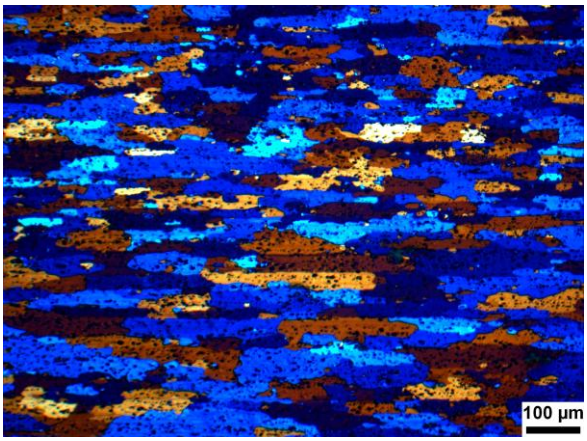

Fig. 4.26: OM-image of C2-B3 annealed at 350 °C for 10^5 s

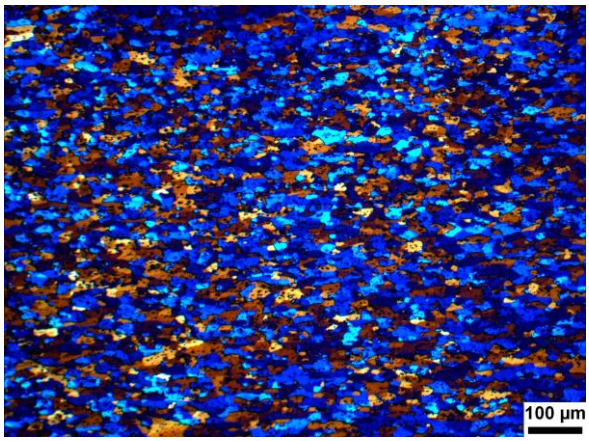

Fig. 4.27: OM-image of C2-B3 annealed at 400 °C for 10^5 s

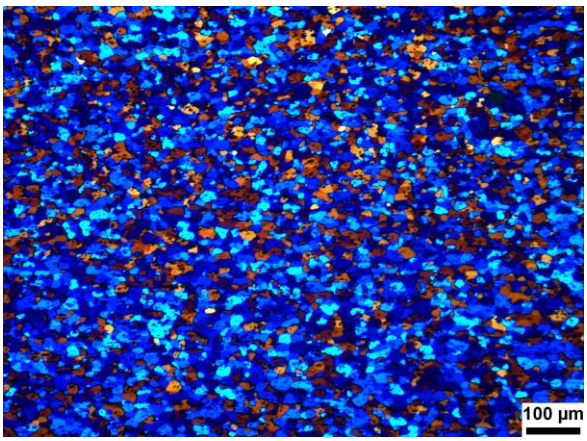

Fig. 4.28: OM-image of C2-B3 annealed at 450 °C for 10^5 s

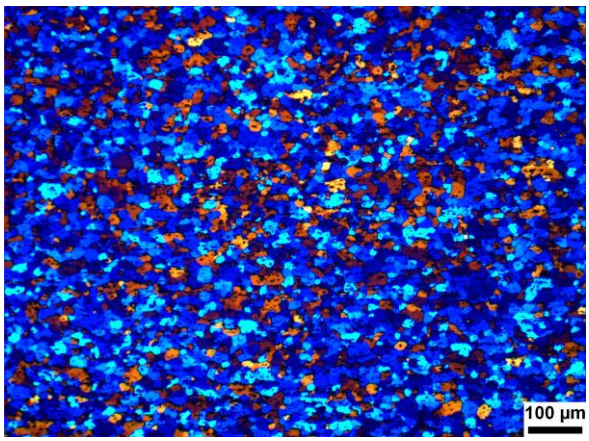

Fig. 4.29: OM-image of C2-B3 annealed at 500 °C for 10^5 s

Fig. 4.26 – Fig. 4.29 show C2-B3 annealed at increasing temperatures. All four figures reveal recrystallised specimens, where the grain size is gradually reduced with increasing temperature.

4.2.5 Recrystallized Grain Size Measurements from OM-images

The grain sizes of all specimens presented with OM-images in the previous chapter, except for C2-A2 annealed at 500 °C for 10^5 s (see Fig. 4.19) were measured in both RD- and ND-

direction using the linear intercept method, as described in Chapter 3.4.4. The results are presented in Table 4.3 below. The grain size of C2-A2 annealed at 500 °C for 10^5 s was not measured by the linear intercept method since the specimen was not recrystallized during annealing, as mentioned in the previous chapter.

Table 4.3: Grain size measurements from OM-images by the linear intercept method

Name	Ann. T. [°C]	Gr. Size – RD-dir. [µm]	Gr. Size – ND-dir. [µm]	RD/ND	Ann. Time [s]
C2-A3	400	285	37	7.7	10^5
C2-A3	450	81	21	3.9	10^5
C2-A3	500	52	19	2.8	10^5
C2-B2	400	37	24	1.6	10^5
C2-B2	450	28	22	1.3	10^5
C2-B2	500	31	24	1.3	10^5
C2-B3	350	86	25	3.4	10^5
C2-B3	400	27	15	1.8	10^5
C2-B3	450	19	15	1.2	10^5
C2-B3	500	21	16	1.3	10^5

The general trend that can be seen from Table 4.3 is that the grain sizes were reduced with increasing annealing temperature for all variants of the C2-alloy. The largest grain size was measured for C2-A3 annealed at 400 °C for 10^5 s, and the smallest grain size was measured for C2-B3 annealed at 450 °C for 10^5 s.

4.2.6 Recrystallized Grain Size Distributions from EBSD-data

As described in Chapter 3.5.4, grain size distributions were produced from the software used to analyze the EBSD-data. A selection of the grain size distributions produced for the recrystallized isothermally annealed specimens are presented in Fig. 4.30 – Fig. 4.34. The

complete datasets for the grain size distributions, with accurate grain sizes and corresponding area fractions, are presented in Appendix C. Grain size distributions for all specimens presented with OM-images in Chapter 4.2.4, except for C2-A2 annealed at 500 °C for 10^5 s and C2-B2 annealed at 400 °C for 10^5 s, are presented below. The grain size distribution of C2-A2 annealed at 500 °C for 10^5 s and C2-B2 annealed at 400 °C for 10^5 s were not measured since specimen C2-A2 was not recrystallized during annealing, and due to a lack of C2-B2 material.

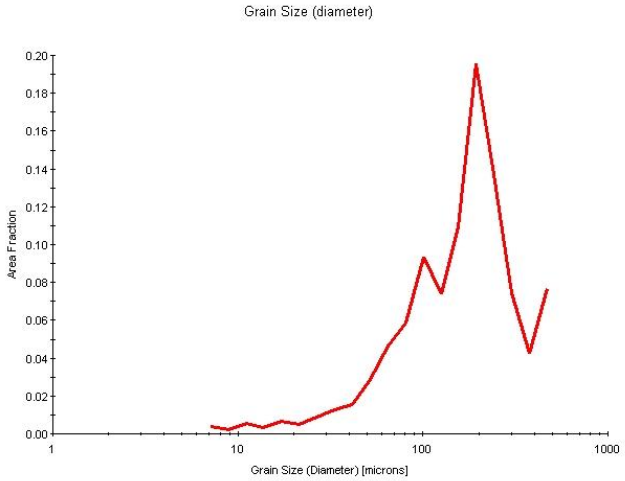

Fig. 4.30: Grain size distribution from a 40X EBSD-scan of C2-A3 annealed at 400 °C for 10^5 s

Fig. 4.30 shows the grain size distributions for C2-A3 annealed at 400 °C for 10^5 s. The grain size distributions for C2-A3 annealed at 450 °C and 500 °C for 10^5 s are presented in Appendix C. All three distributions show relatively homogeneous grain sizes, and the dominating grain size for all three distributions are in the same scale as the measured average grain sizes for the same specimens, presented in the previous chapter. Fig. 4.31 shows the grain size distributions for C2-B2 annealed at 450 °C for 10^5 s. The grain size distribution for C2-B2 annealed at 500 °C for 10^5 s is presented in Appendix C. Both distributions reveal relatively homogeneous grain sizes, and the dominating grain size for both distributions are in the same scale as the measured average grain size for the same specimens, presented in the previous chapter.

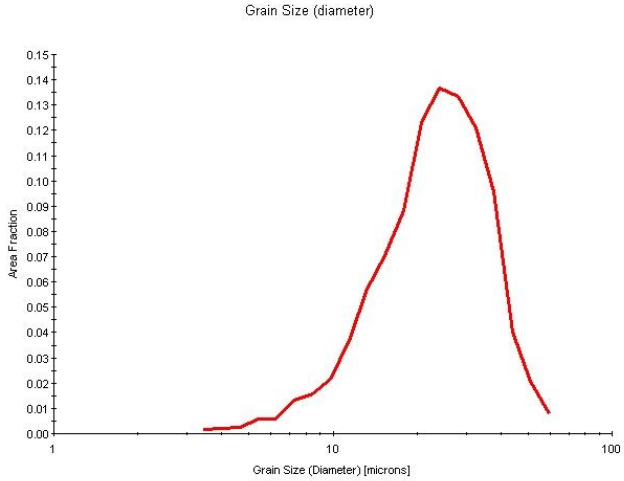

Fig. 4.31: Grain size distribution from a 60X EBSD-scan of C2-B2 annealed at 450 °C for 10^5 s

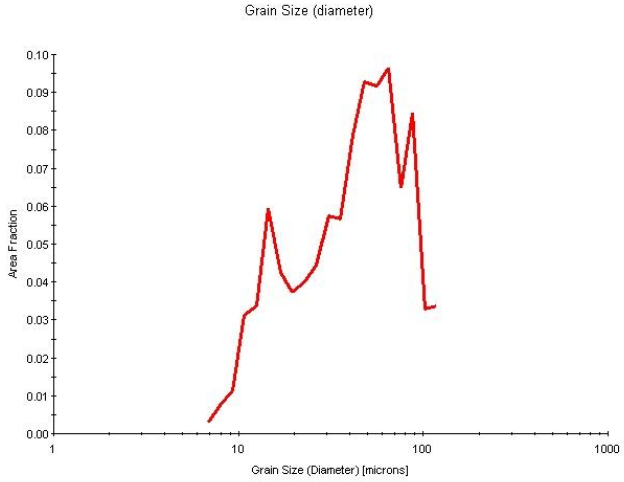

Fig. 4.32: Grain size distribution from a 80X EBSD-scan of C2-B3 annealed at 350 °C for 10^5 s

Fig. 4.32 – 4.34 show the grain size distributions for C2-B3 annealed at 350 °C, 400 °C and 450 °C for 10^5 s. The grain size distribution for C2-B3 annealed at 500 °C for 10^5 s is presented in Appendix C. The distribution for C2-B3 annealed at 350 °C is relatively inhomogeneous and the dominating grain size diameters seem to be between 10 μm and 100 μm. The grain size distribution for C2-B3 annealed at 400 °C also looks slightly inhomogeneous, but not to the same degree as the distribution for C2-B3 annealed at 350 °C.

The dominating grain size diameters are between 10 µm and 20 µm, which correspond well to the average grain size measurements on the same specimen in the previous chapter.

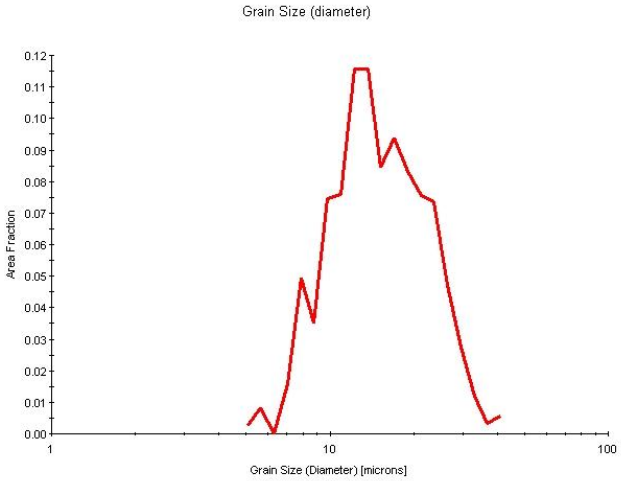

Fig. 4.33: Grain size distribution from a 80X EBSD-scan of C2-B3 annealed at 400 °C for 10^5 s

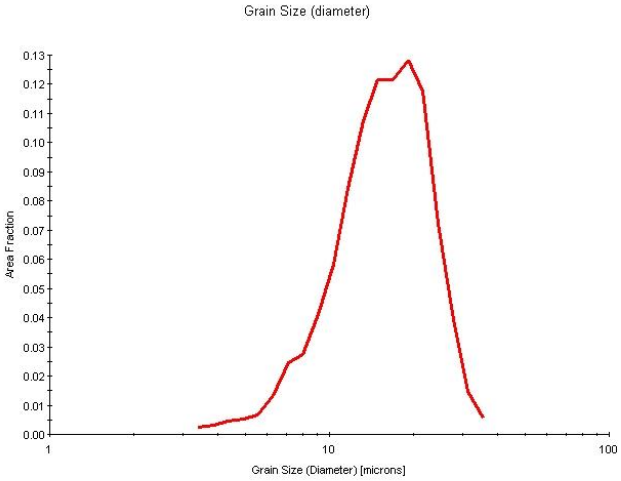

Fig. 4.34: Grain size distribution from a 80X EBSD-scan of C2-B3 annealed at 450 °C for 10^5 s

The grain size distributions for C2-B3 annealed at 450 °C and 500 °C are both showing a homogeneous grain size and the dominating grain size in both distributions correspond well to the average grain size measurements on the same specimens, presented in the previous chapter.

4.2.7 Texture Results

The results from the texture measurements of the isothermally annealed specimens, described in Chapter 3.5, are presented in the following. The pole figures from all texture measurements in this work are presented in Appendix D. The texture of C2-B2 annealed at 400 °C for 10^5 s was not investigated due to a lack of C2-B2 material, as also mentioned in the previous chapter. Fig. 4.35 shows the OIM-maps of C2-A3 annealed at 400 °C, 450 °C and 500 °C, where all the OIM-maps show recrystallised grains elongated in the rolling direction. The final grain size for C2-A3 can be seen to be reduced with a higher annealing temperature, consistent with the results in Chapters 4.2.4, 4.2.5 and 4.2.6.

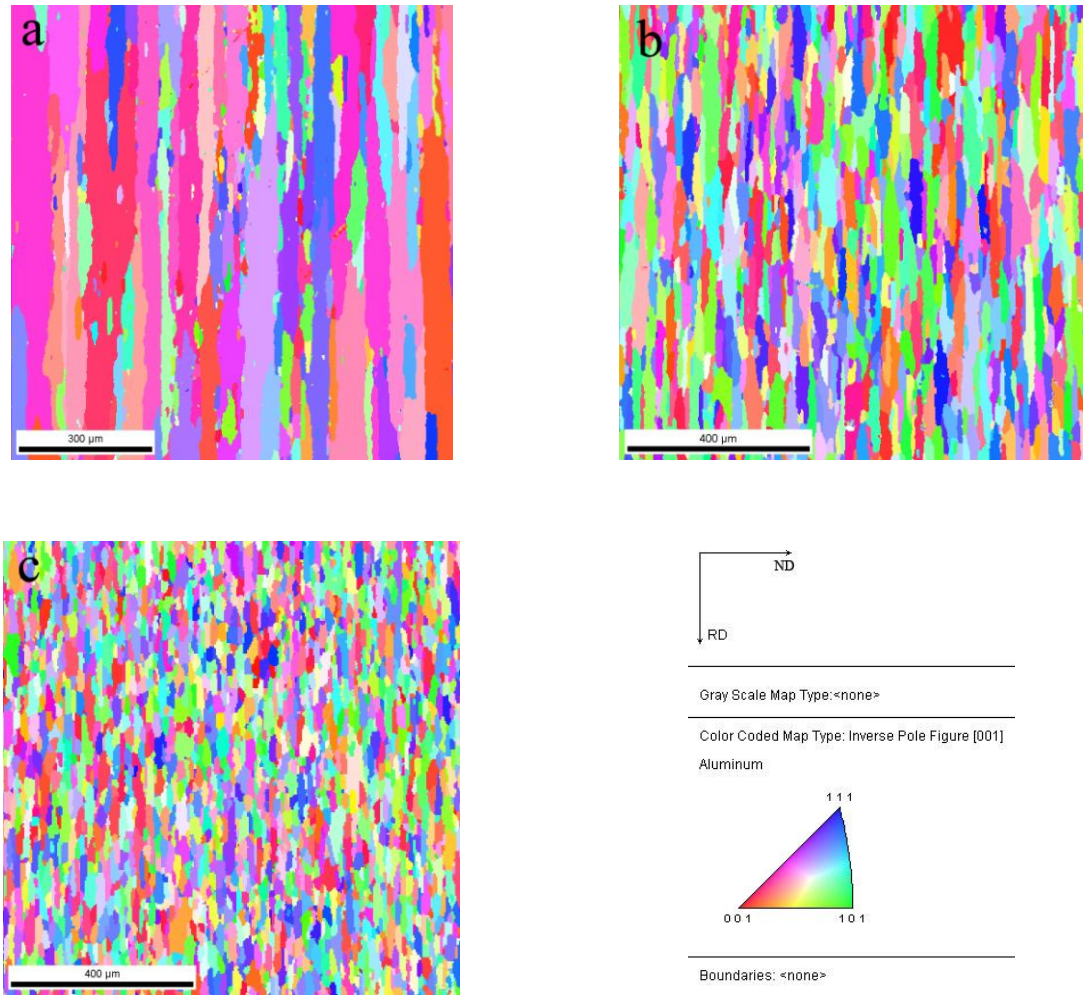

Fig 4.35: OIM-maps of C2-A3 annealed for 10^5 s at (a) 400 °C, (b) 450 °C and (c) 500 °C from 80X EBSD-scans

The ODF of C2-A3 annealed at 400 °C for 10^5 s is presented in Fig. 4.36. The texture in this ODF is strong, but not very easy to interpret. By studying the φ_2 = 0 ° section of the ODF, a possibly strong ND-rotated cube texture can be seen and also a relatively strong P-texture (see Fig. 2.20 and Fig. 2.22 in Chapter 2.6.2). By studying the φ_2 = 15 ° section of the ODF what might be Q-texture can also be observed (see Fig. 2.2.3 in Chapter 2.6.2).

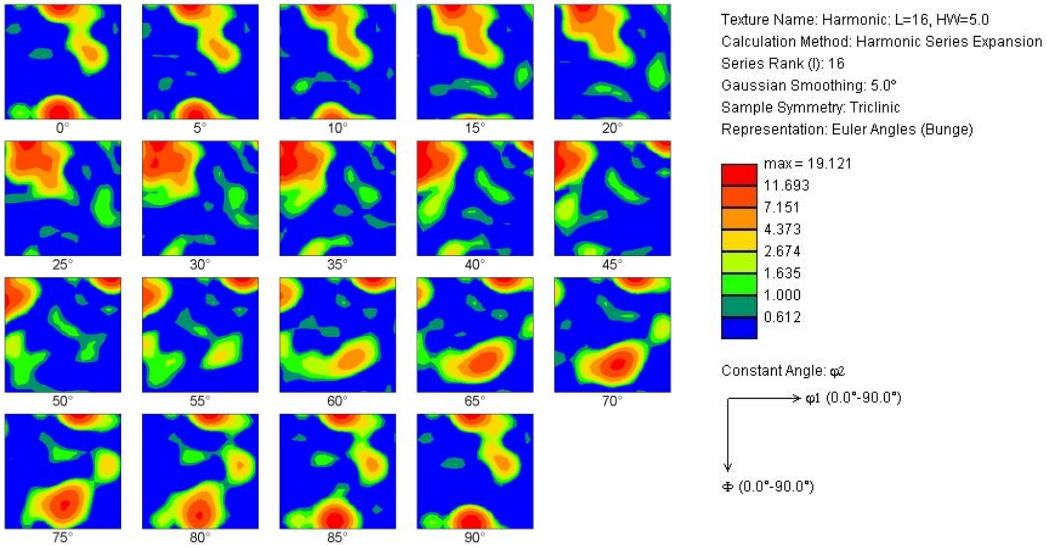

Fig. 4.36: ODF of C2-A3 annealed at 400 °C for 10^5 s from a 40X EBSD-scan

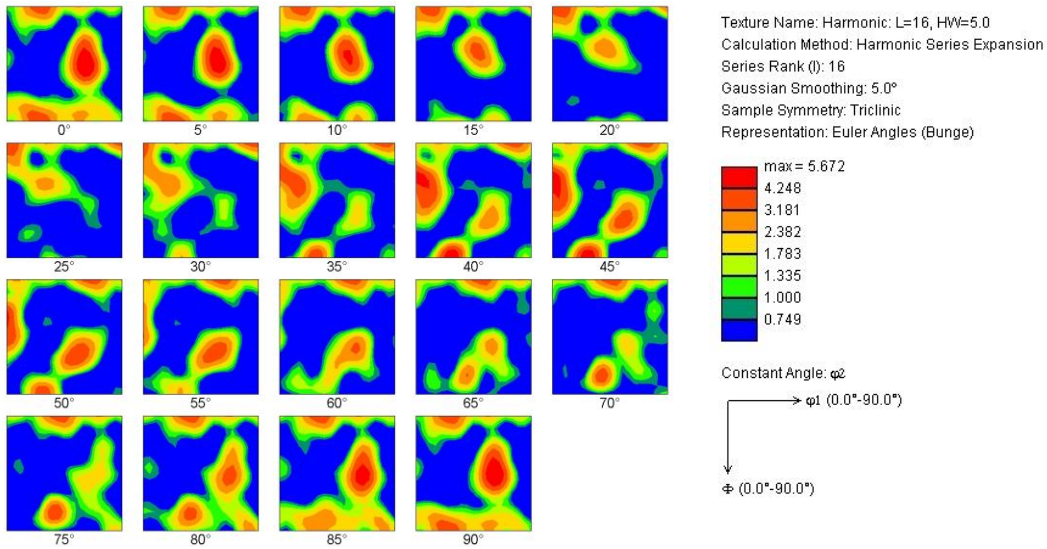

Fig. 4.37: ODF of C2-A3 annealed at 450 °C for 10^5 s from a 80X EBSD-scan

The ODF of C2-A3 annealed at 450 °C for 10^5 s is presented in Fig. 4.37. Section φ_2 = 0 ° in this ODF show a relatively strong ND-rotated cube texture and P-texture (see Fig. 2.20 and Fig. 2.22 in Chapter 2.6.2). Fig. 4.38 show the ODF of C2-A3 annealed at 500 °C for 10^5 s. The texture seems relatively weak, but as for C2-A3 annealed at 450 °C, section φ_2 = 0 ° shows ND-rotated cube texture and P-texture (see Fig. 2.20 and Fig. 2.22 in Chapter 2.6.2).

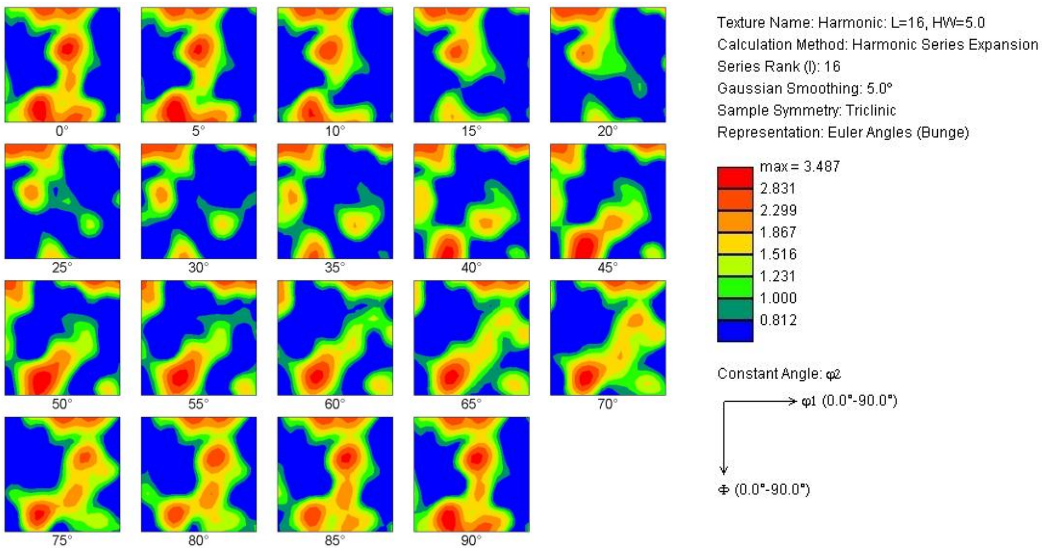

Fig. 4.38: ODF of C2-A3 annealed at 500 °C for 10^5 s from a 80X EBSD-scan

Fig. 4.39 shows the OIM-maps of C2-B2 annealed at 450 °C and 500 °C, where both OIM-maps show approximately equiaxed recrystallised grains with no remarkable size differences, consistent with the results in Chapters 4.2.4, 4.2.5 and 4.2.6.

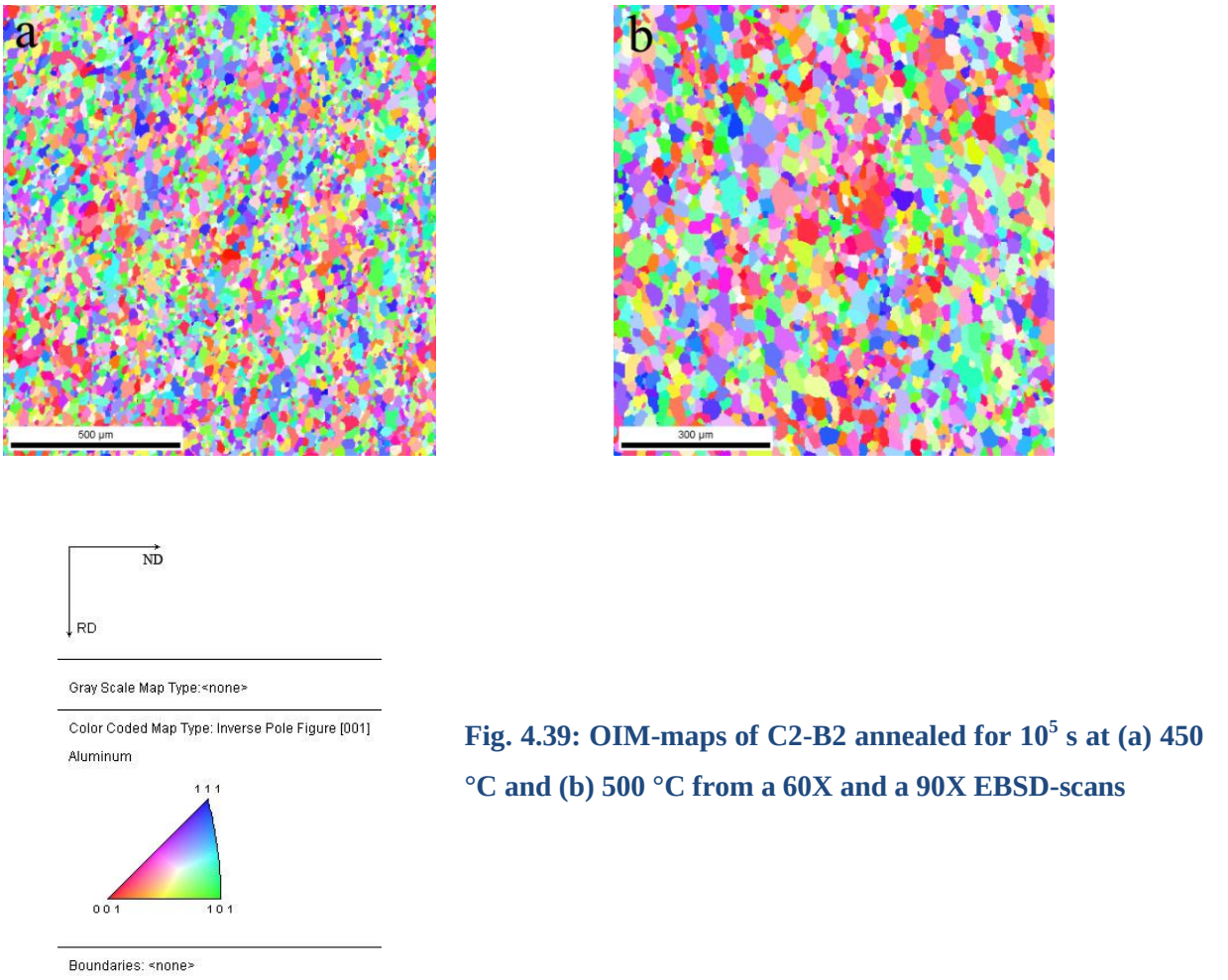

Fig. 4.39: OIM-maps of C2-B2 annealed for 10^5 s at (a) 450 °C and (b) 500 °C from a 60X and a 90X EBSD-scans

Fig. 4.40 presents the ODF of C2-B2 annealed at 450 °C for 10^5 s. The texture in this ODF is very weak and random. No clear recrystallised texture components can be seen in the different sections of the ODF. The ODF of C2-B2 annealed at 500 °C for 10^5 s is presented in Fig. 4.41. Compared to the ODF in Fig. 4.40 the texture is not much stronger, but the ND-rotated cube texture can be seen in the $\varphi_2 = 0°$ section of the ODF (see Fig. 2.20 and Fig. 2.22 in Chapter 2.6.2). However, the texture for C2-B2 annealed at 500 °C still seems somewhat random, just as for C2-B2 annealed at 450 °C.

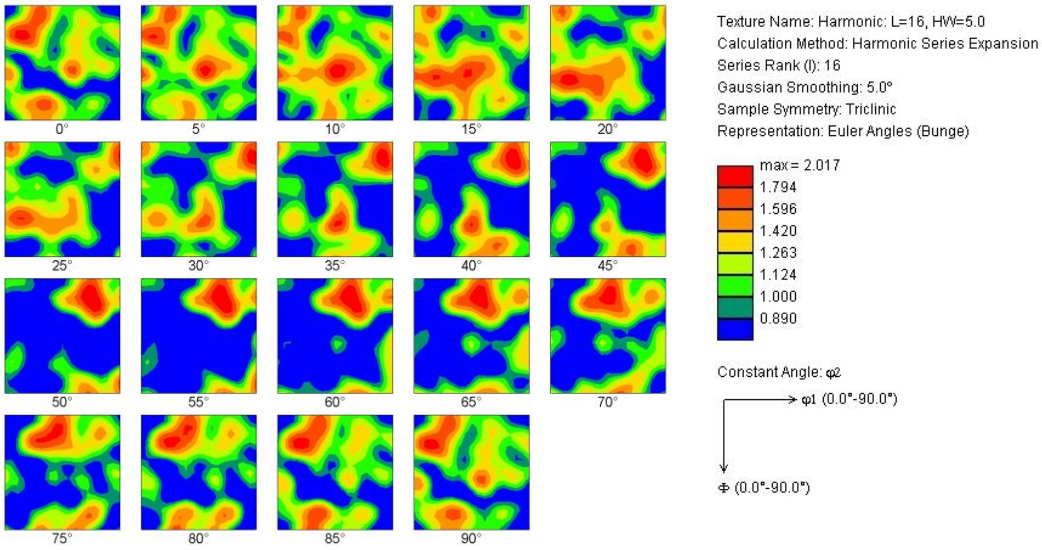

Fig. 4.40: ODF of C2-B2 annealed at 450 °C for 10^5 s from a 60X EBSD-scan

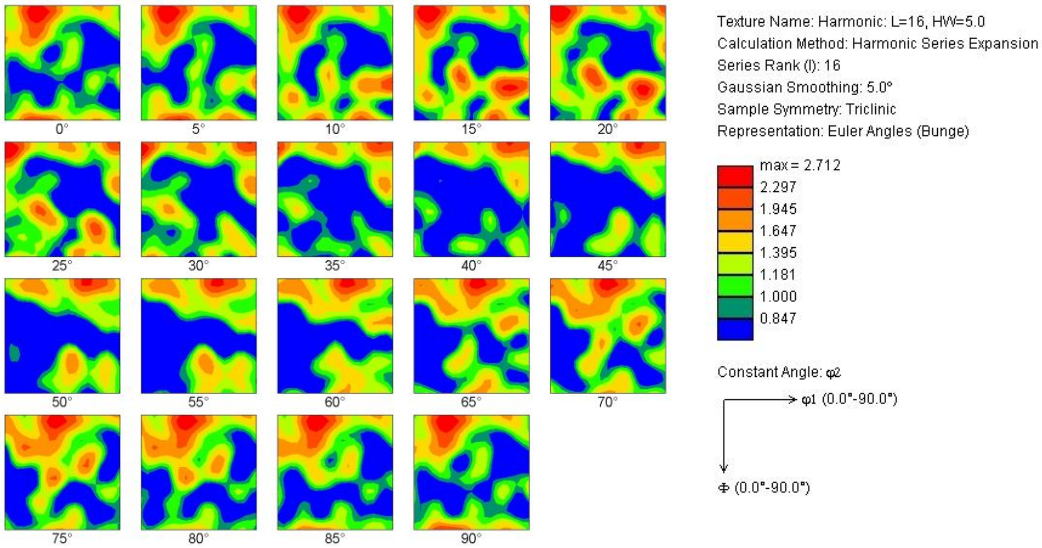

Fig. 4.41: ODF of C2-B2 annealed at 500 °C for 10^5 s from a 90X EBSD-scan

Fig. 4.42 presents the OIM-maps of C2-B3 annealed at 350 °C, 400 °C, 450 °C and 500 °C, where the OIM-maps of C2-B3 annealed at 350 °C and 400 °C show recrystallised grains elongated in the rolling direction, and the OIM-maps of C2-B3 annealed at 450 °C and 500 °C show approximately equiaxed recrystallised grains. The OIM-maps show a grain size gradually reduced with increased annealing temperature, consistent with the results in Chapters 4.2.4, 4.2.5 and 4.2.6.

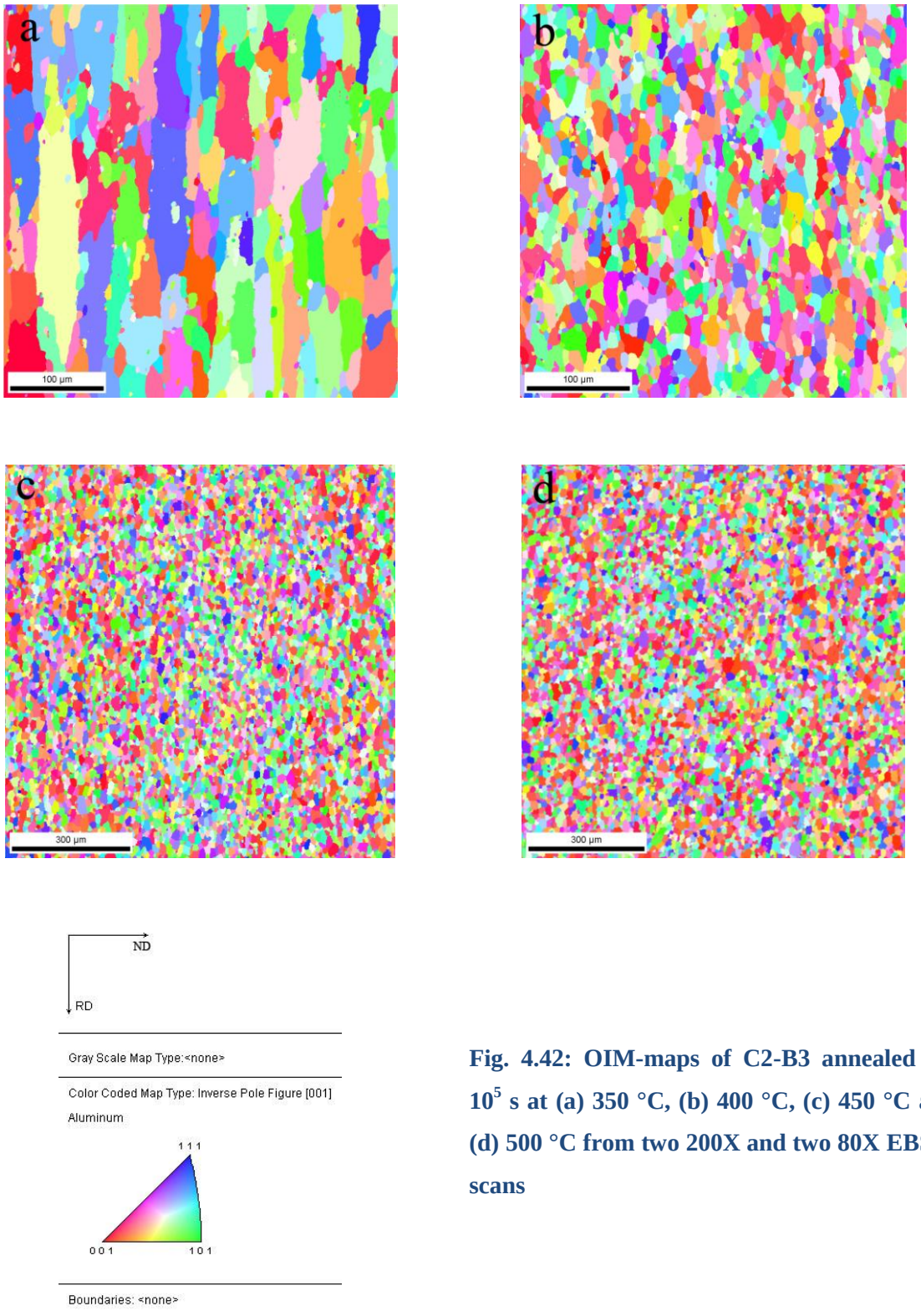

Fig. 4.42: OIM-maps of C2-B3 annealed for 10^5 s at (a) 350 °C, (b) 400 °C, (c) 450 °C and (d) 500 °C from two 200X and two 80X EBSD-scans

The ODF of C2-B3 annealed at 350 °C for 10^5 s is presented in Fig. 4.43. A relatively strong ND-rotated cube- and P-texture can be seen in section $\varphi_2 = 0°$ of the ODF (see Fig. 2.20 and Fig. 2.22 in Chapter 2.6.2).

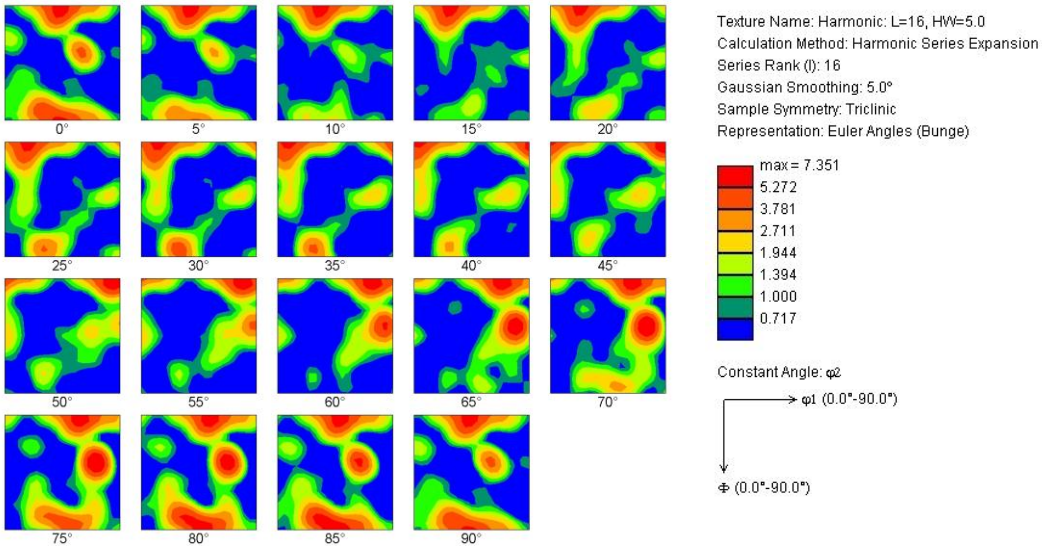

Fig. 4.43: ODF of C2-B3 annealed at 350 °C for 10^5 s from a 80X EBSD-scan

In Fig. 4.44 the ODF of C2-B3 annealed at 400 °C for 10^5 s is presented. The texture in this ODF is weaker compared to the ODF in Fig. 4.43 and no P-texture component can be seen in section $\varphi_2 = 0°$ of the ODF. The ND-rotated cube texture is still present.

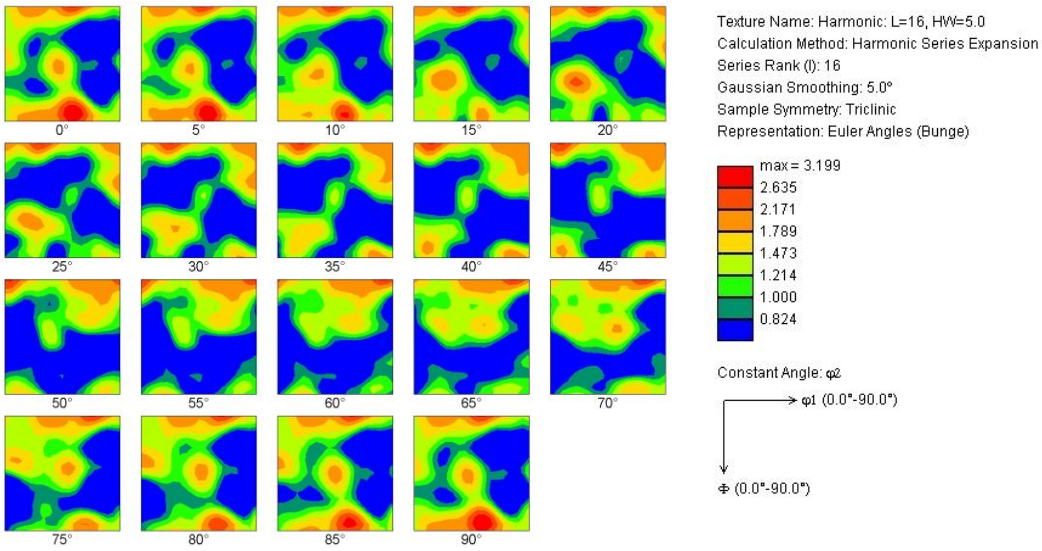

Fig. 4.44: ODF of C2-B3 annealed at 400 °C for 10^5 s from a 80X EBSD-scan

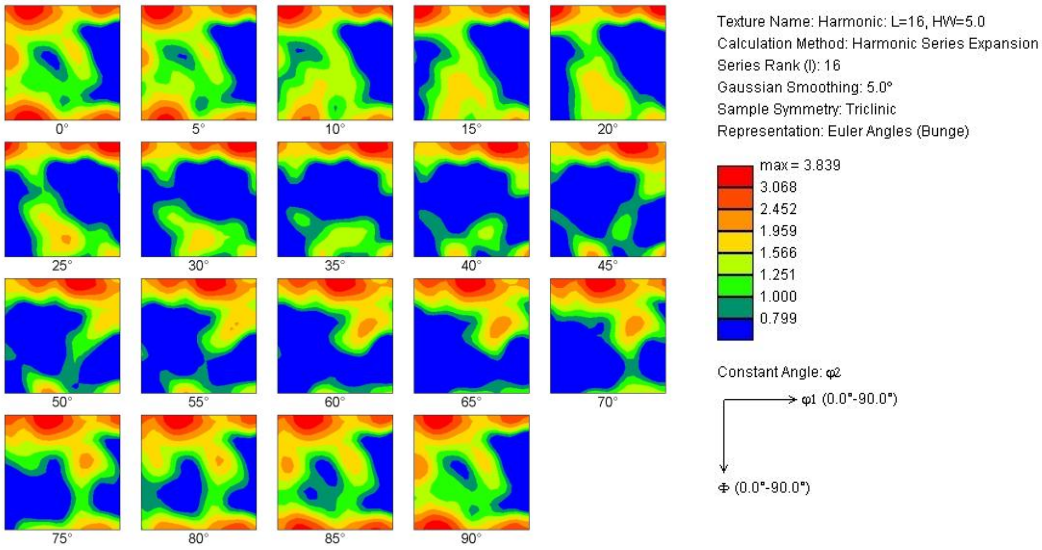

Fig. 4.45: ODF of C2-B3 annealed at 450 °C for 10^5 s from a 80X EBSD-scan

The ODF of C2-B3 annealed at 450 °C for 10^5 s is presented in Fig. 4.45. As for the ODF in Fig. 4.44, the texture is relatively weak, but clear. By studying the $\varphi_2 = 0°$ section of the ODF the texture seems to be a combination of a cube- and a ND-rotated cube texture (see Fig. 2.20, Fig. 2.22 and Fig. 2.23 in Chapter 2.6.2).

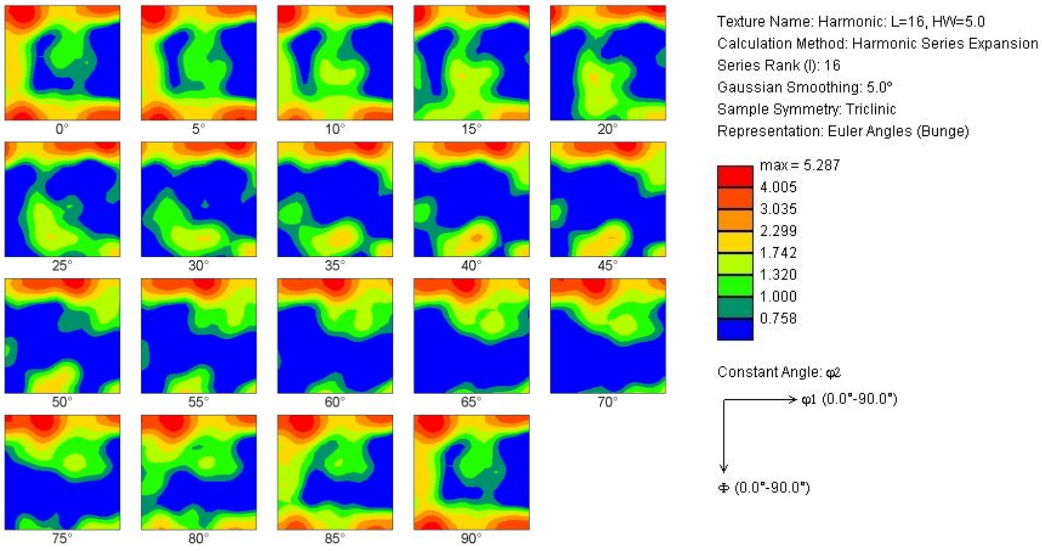

Fig. 4.46: ODF of C2-B3 annealed at 500 °C for 10^5 s from a 80X EBSD-scan

The texture in Fig. 4.46, showing the ODF of C2-B3 annealed at 500 °C for 10^5 s, is somewhat stronger compared to the two previously described ODFs. By studying the $\varphi_2 = 0°$ section of the ODF a clear cube texture can be seen (see Fig. 2.20 and Fig. 2.23 in Chapter 2.6.2).

4.3 Non-Isothermal Annealing Experiments

4.3.1 Softening Curves

Softening curves for C2-A3, C2-B3 and C2-C3 showing the hardness development during the non-isothermal annealing experiments described in Chapter 3.3 are presented in Fig. 4.47. The softening curves are presented in a HV vs. annealing time plot. HV values from the initial characterization (Table 4.1) of the C2-alloy variants are also included in the plot for comparison reasons. The first HV value for all three curves represents the HV value of the respective as deformed alloy variants before annealing.

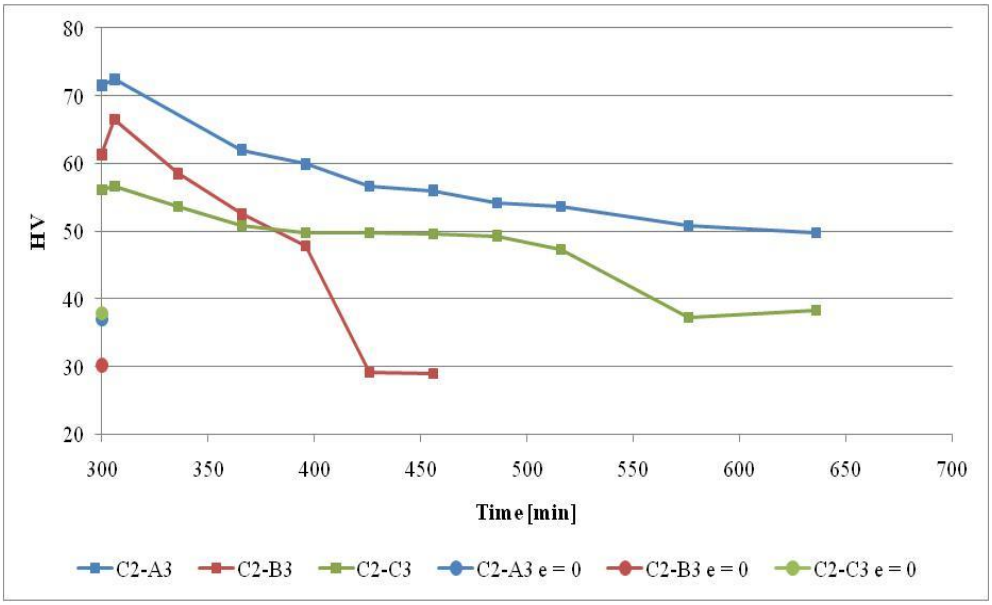

Fig. 4.47: Softening curves for C2-A3, C2-B3 and C2-C3 non-isothermally annealed

By studying Fig. 4.47, only a small and relatively slow reduction of hardness corresponding to typical recovery behavior (see Chapter 2.5) can be seen from the softening curve for C2-A3. The softening curve for C2-B3 shows a fast and steady reduction of hardness in the beginning

of the annealing procedure, consistent with recovery behavior, before a large hardness reduction with a subsequent leveling of the softening curve, consistent with recrystallization behavior (see Chapter 2.5). The softening curve of C2-C3 shows typical recovery behavior, with only a small and relatively slow reduction of hardness, for a long annealing period before a relatively large hardness reduction and subsequent leveling of the softening curve, consistent with recrystallization behavior. A relatively small increase in HV can be observed early in all three softening curves. The small hardness increase that can be seen at the end of the annealing procedure for C2-C3 is probably due to a measurement error.

4.3.2 Electrical Conductivity Measurements

Electrical conductivity curves for C2-A3, C2-B3 and C2-C3 showing the electrical conductivity development during the non-isothermal annealing experiments described in Chapter 3.3 are presented in Fig. 4.48. The curves are presented in an EC vs. annealing time plot. EC values from the initial characterization (Table 4.1) of the C2-alloy variants are also included in the plot for comparison reasons. The first EC value for all three curves represents the EC value of the respective as deformed alloy variants before annealing.

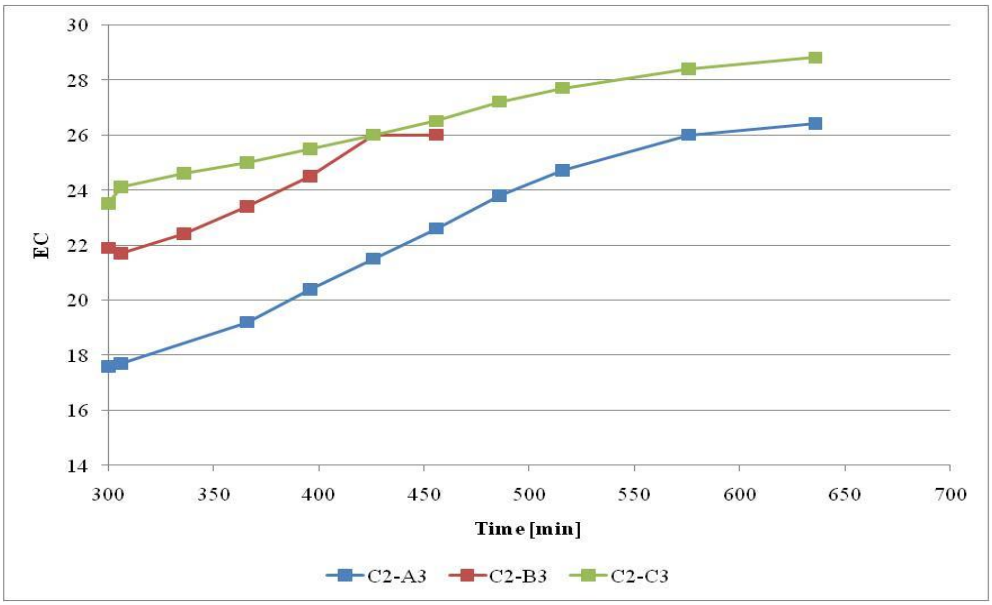

Fig. 4.48: EC curves for C2-A3, C2-B3 and C2-C3 non-isothermally annealed

As explained in Chapter 4.2.1, manganese in solid solution distorts the atomic lattice of the alloy and consequently lowers the conductivity (see Chapter 2.7.2). Because of this, the development in electrical conductivity during annealing will be a good indication of the amount of precipitation during annealing (see Chapter 2.5.1); i.e. since the amount of manganese in solid solution is reduced during precipitation. By studying Fig. 4.48 one can see that the electrical conductivity clearly increased with annealing time, which indicates considerable precipitation for all three specimen variants. The EC of C2-A3 increased the most and the EC of C2-B3 increased the least. All three EC curves seem to level out in the end of the annealing procedure, this especially for C2-B3. C2-C3 has the highest measured conductivity value at the end of the annealing procedure. The slopes of the EC curves for C2-A3 and C2-C3 seems to develop without any interference, indicating only recovery behavior, according to the results from the isothermal annealing procedures (see Chapter 4.2). The slope of the precipitation curve for C2-B3 levels out when the softening curve for C2-B3 (in Fig. 4.47) shows recrystallization softening behavior.

4.3.3 Texture Results

The results from the texture measurements of the non-isothermally annealed specimens described in Chapter 3.5 are presented in the following. All the non-isothermal specimens listed in Table 3.11, Table 3.13 and Table 3.14 were investigated. The pole figures from all texture measurements in this work are presented in Appendix D.

Fig. 4.49 and Fig. 4.50 show the OIM-map and the ODF for C2-A3 non-isothermally annealed and taken out of the oven after 3 h at 400 °C. The grain structure seen in the OIM-map is a combination of very large grains and small grains, all elongated in the rolling direction. The grain structure seems to be recovered and not recrystallised. The texture in the ODF is strong, but no typical recrystallised texture components can be seen, except for what might be a somewhat strong Q-component in the φ_2 = 15 ° section of the ODF (see Fig. 2.22 and Fig. 2.23 in Chapter 2.6.2). These results combined with the softening curve and the precipitation curve in Fig. 4.47 and 4.48 demonstrates that this specimen is not recrystallised, and due to this no more measurements were performed on this specimen.

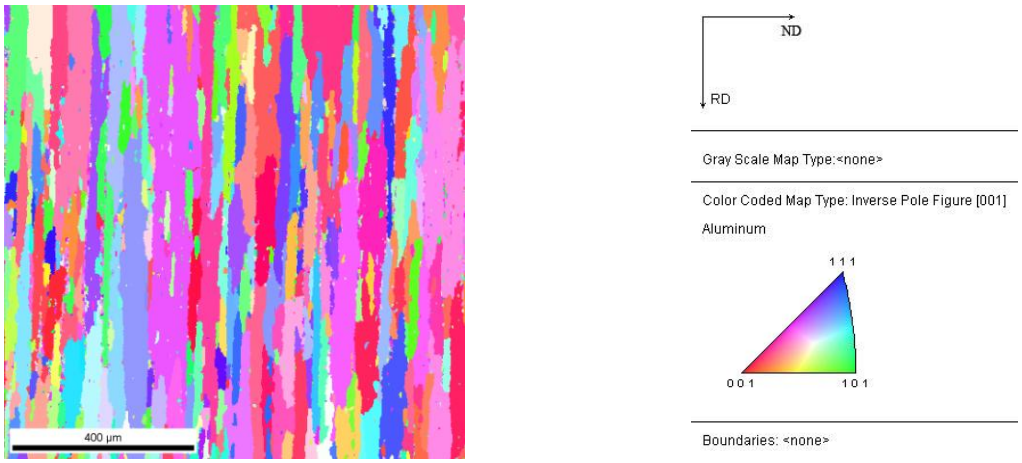

Fig. 4.49: OIM-map from a 80X EBSD-scan of C2-A3 non-isothermally annealed and taken out of oven after 3 h at 400 °C

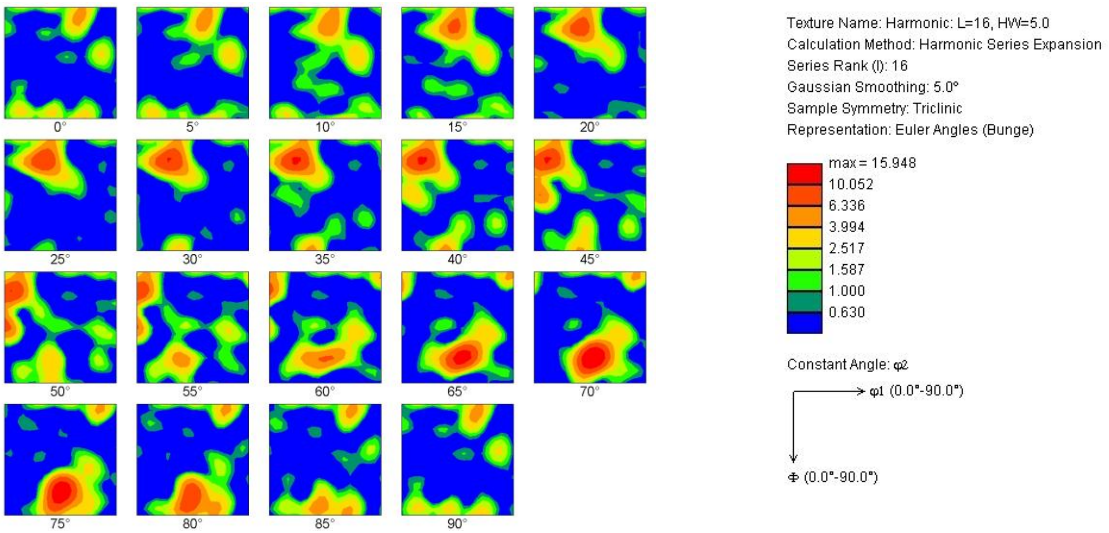

Fig. 4.50: ODF from a 80X EBSD-scan of C2-A3 non-isothermally annealed and taken out of oven after 3 h at 400 °C

Fig. 4.51 and Fig. 4.52 show the OIM-map and the ODF for C2-B3 non-isothermally annealed and taken out of the oven at 375 °C. The OIM-map shows a combination of relatively large recrystallised grains elongated in the rolling direction and some smaller equiaxed grains. By studying the φ_2 = 0 ° section of the ODF one can see ND-rotated cube- and P-texture of medium strength (see Fig. 2.20 and Fig. 2.22 in Chapter 2.6.2). The specimen

is clearly recrystallised consistent with the softening curve and the precipitation curve for the specimen in Fig. 4.47 and Fig. 4.48.

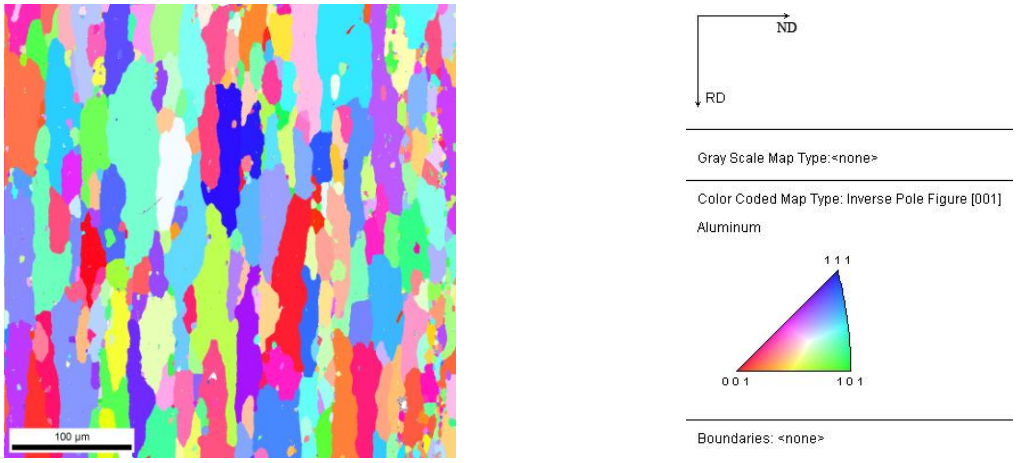

Fig. 4.51: OIM-map from a 200X EBSD-scan of C2-B3 non-isothermally annealed and taken out of oven at 375 °C

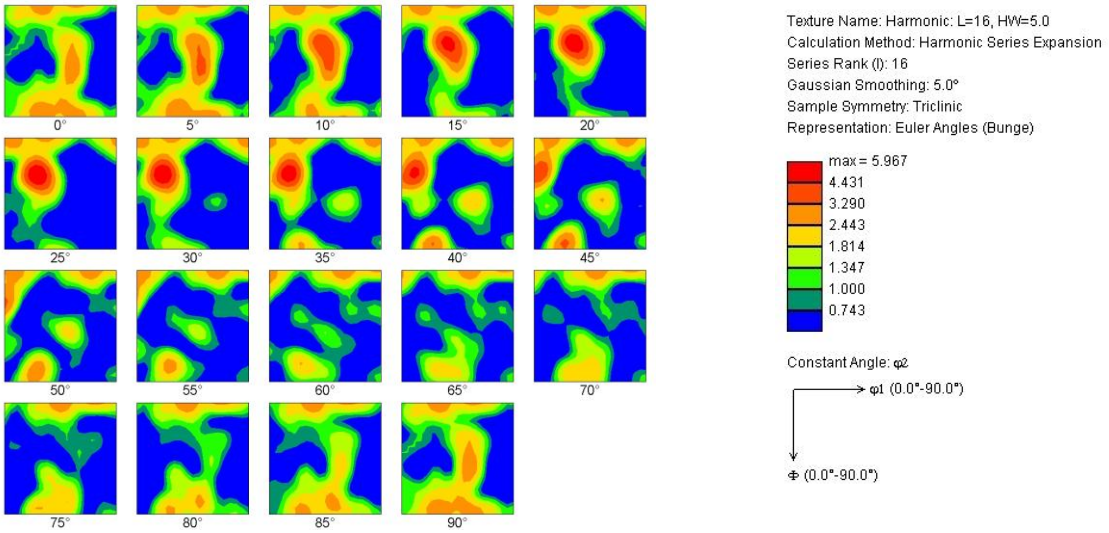

Fig. 4.52: ODF from a 80X EBSD-scan of C2-B3 non-isothermally annealed and taken out of oven at 375 °C

Fig. 4.53 and Fig. 4.54 present the OIM-map and the ODF for C2-B3 non-isothermally annealed and taken out of the oven at 400 °C. Much in the same way as the OIM-map in Fig. 4.51, the OIM-map in Fig. 4.53 shows a combination of relatively large recrystallised grains elongated in the rolling direction and some smaller more equiaxed grains. By studying the φ_2

= 0° section of the ODF one can see a ND-rotated cube texture of medium strength (see Fig. 2.20 and Fig. 2.22 in Chapter 2.6.2). The P-component seen in the 375 °C specimen is not present in the 400 °C specimen.

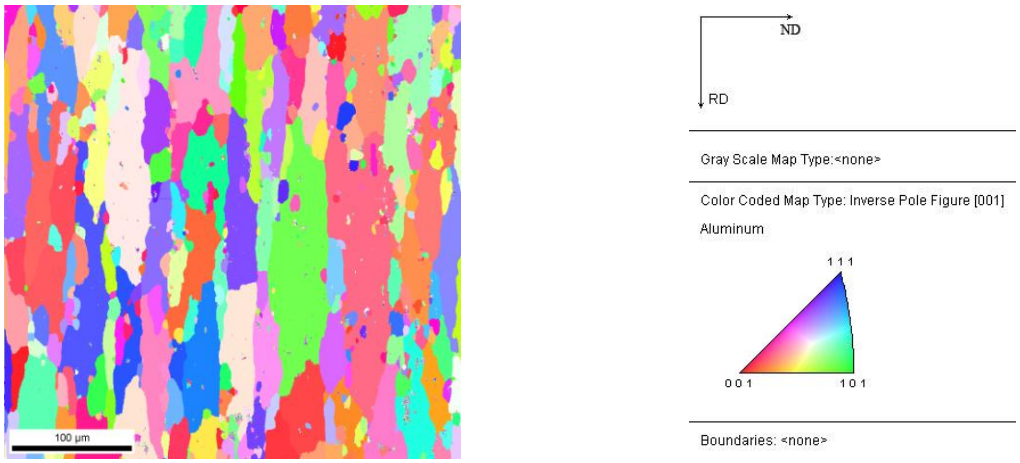

Fig. 4.53: OIM-map from a 200X EBSD-scan of C2-B3 non-isothermally annealed and taken out of oven at 400 °C

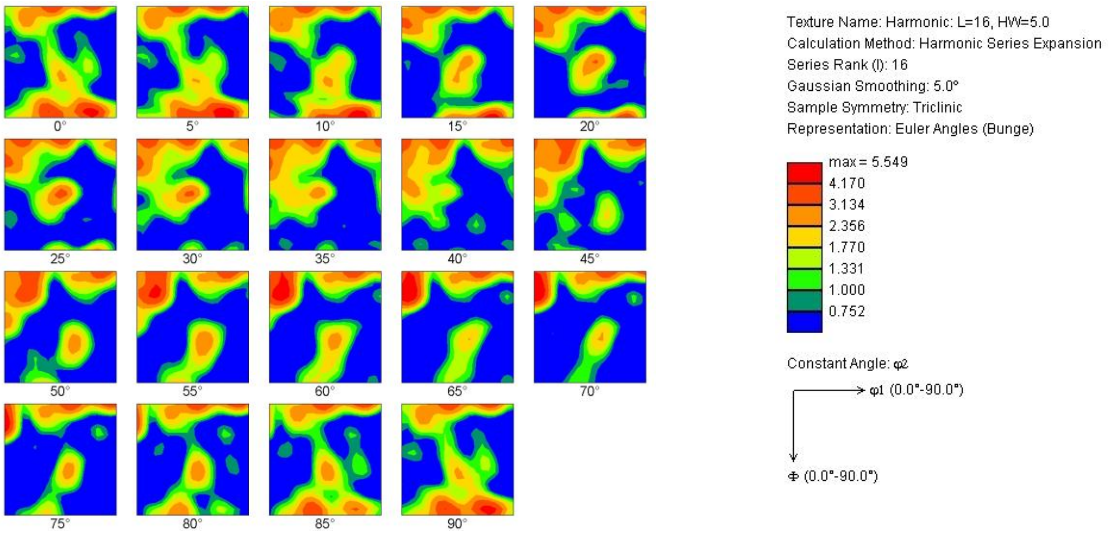

Fig. 4.54: ODF from a 80X EBSD-scan of C2-B3 non-isothermally annealed and taken out of oven at 400 °C

Fig. 4.55 and Fig. 4.56 show the OIM-map and the ODF for C2-C3 non-isothermally annealed and taken out of the oven after 2 h at 400 °C. The OIM-map reveals areas where a clear deformation structure still is present, while the $\varphi_2 = 45$ ° and $\varphi_2 = 65$ ° of the ODF reveal

strong Cu- and S-texture components (see Fig. 2.19 in Chapter 2.6.1). The specimen is clearly not fully recrystallised, partially consistent with the softening curve and the EC curve for the specimen in Fig. 4.47 and Fig. 4.48. The EC curve shows an uninterrupted precipitation process while the softening curve shows a possible recrystallization behavior in the end of the annealing procedure. No more measurements were performed on this specimen.

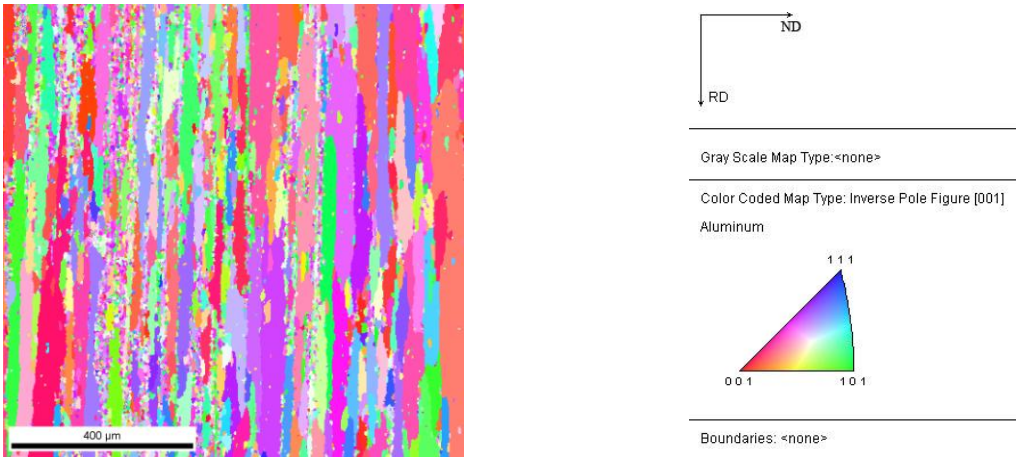

Fig. 4.55: OIM-map from a 80X EBSD-scan of C2-C3 non-isothermally annealed and taken out of oven after 2 h at 400 °C

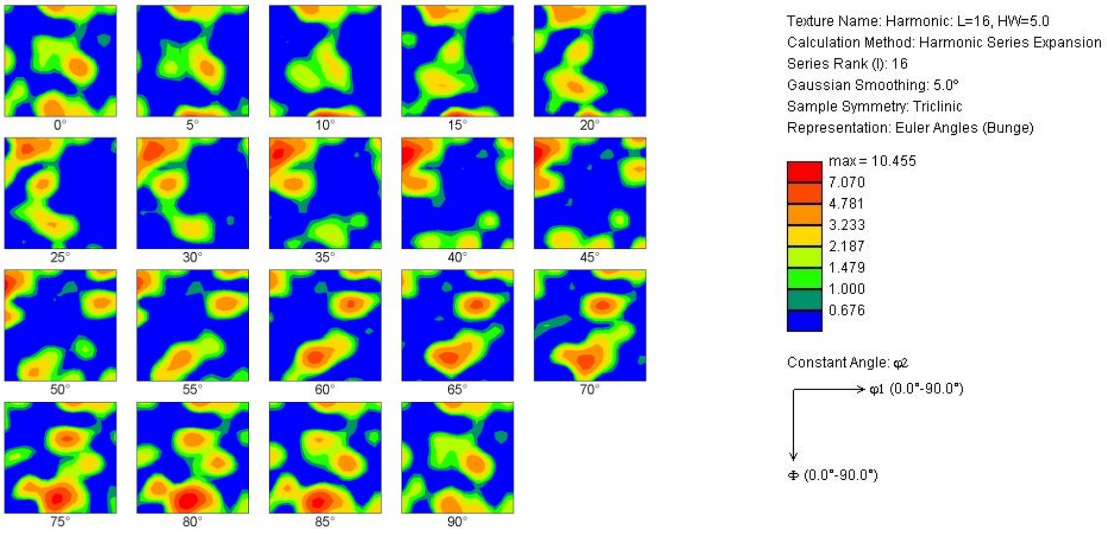

Fig. 4.56: ODF from a 80X EBSD-scan of C2-C3 non-isothermally annealed and taken out of oven after 2 h at 400 °C

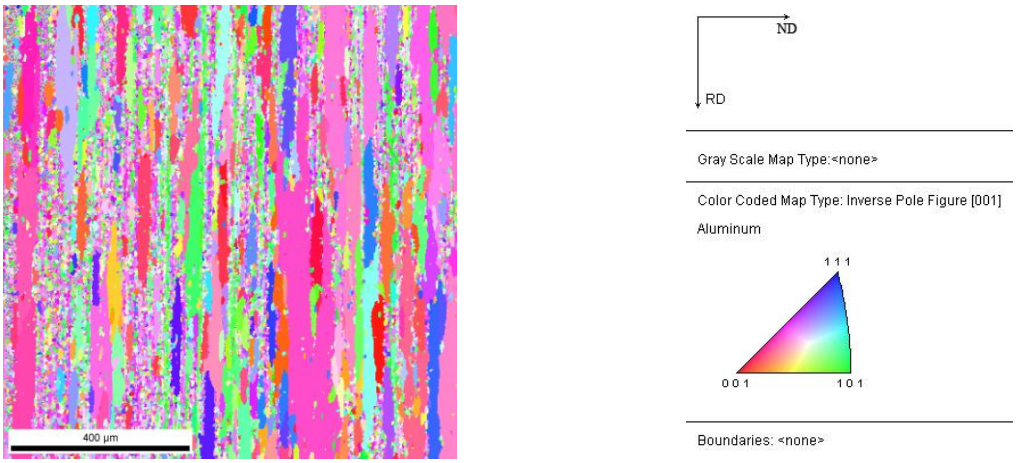

Fig. 4.57: OIM-map from a 80X EBSD-scan of C2-C3 non-isothermally annealed and taken out of oven after 3 h at 400 °C

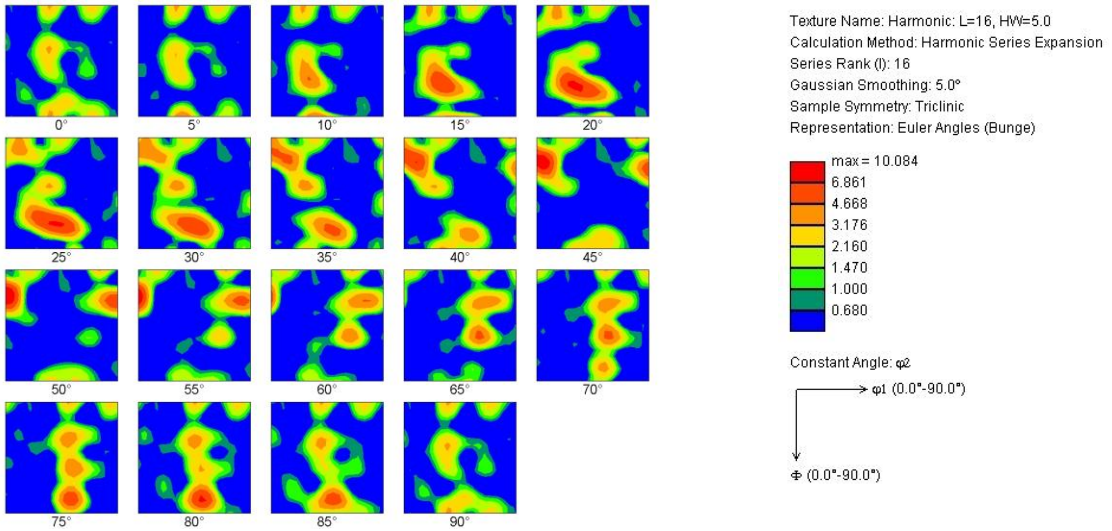

Fig. 4.58: ODF from a 80X EBSD-scan of C2-C3 non-isothermally annealed and taken out of oven after 3 h at 400 °C

Fig. 4.57 and Fig. 4.58 show the OIM-map and the ODF for C2-C3 non-isothermally annealed and taken out of the oven after 3 h at 400 °C. The OIM-map reveals areas where a clear deformation structure still is present, while the $\varphi_2 = 45$ ° and $\varphi_2 = 65$ ° of the ODF reveal relatively strong Cu- and S-texture components (see Fig 2.19 in Chapter 2.6.1). The specimen is clearly not fully recrystallised, partially consistent with the softening curve and the EC curve for the specimen in Fig. 4.47 and Fig. 4.48. The EC curve shows an uninterrupted

precipitation process while the softening curve shows a possible recrystallization behavior in the end of the annealing procedure. No more measurements were performed on this specimen.

4.3.4 Optical Microscope Images

The optical microscope images of the selection of non-isothermally annealed specimens listed in Table 3.7 in Chapter 3.4.3 are presented in Fig. 4.59 and Fig. 4.60. See Chapter 3.3.2 for detailed information about the non-isothermal annealing procedures. The specimen preparation is described in Chapter 3.4.3.

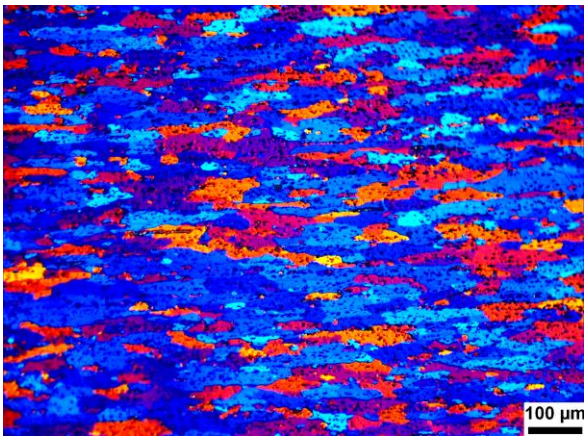

Fig. 4.59: OM-image of C2-B3 – sample taken out of oven at 375 °C

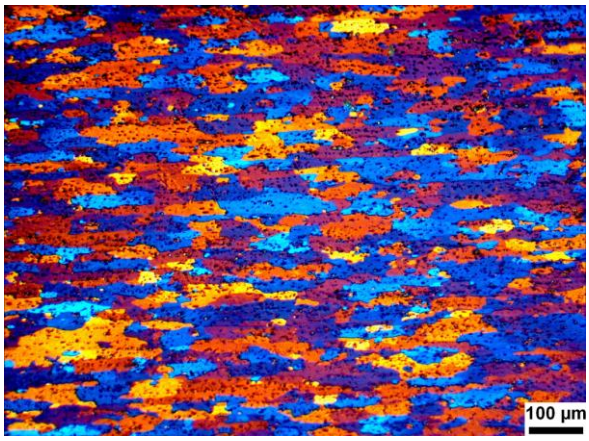

Fig. 4.60: OM-image of C2-B3 – sample taken out of oven at 400 °C

Both Fig. 4.59 and Fig. 4.60 show recrystallised grain structures where a combination of large grains elongated in the rolling direction and smaller grains can be seen. These results are consistent with the OIM-maps of the same specimens presented in the previous chapter (see Fig. 4.51 and Fig. 4.53).

4.3.5 Recrystallized Grain Size Measurements from OM-images

The grain sizes of the two specimens presented with OM-images in the previous chapter were measured in both RD- and ND-direction using the linear intercept method as described in

Chapter 3.4.4. The results are presented in Table 4.4 below. The non-isothermal annealing procedures are described in Chapter 3.3.

Table 4.4: Grain size measurements from OM-images

Name	Ann. Proc. Non-isothermal	Gr. Size – RD-dir. [µm]	Gr. Size – ND-dir. [µm]	RD/ND
C2-B3	Taken out of oven at 375 °C	56	22	2.5
C2-B3	Taken out of oven at 400 °C	68	23	3.0

By studying Table 4.4 above, one can see that the grain size has increased with the longer holding time for the specimen taken out at 400 °C compared to the specimen taken out at 375 °C, possibly indicating that the recrystallization process was not complete when the 375 °C was taken out of the oven.

4.3.6 Recrystallized Grain Size Distributions from EBSD-data

As described in Chapter 3.5.4, grain size distributions were produced from the software used to analyze the EBSD-data. The grain size distributions produced for the recrystallised non-isothermally annealed specimens are presented in Fig. 4.61 and Fig. 4.62. The complete datasets for the grain size distributions with accurate grain sizes and corresponding area fractions are presented in Appendix C. An overview of the non-isothermally annealed specimens studied by the EBSD-method can be found in Chapter 3.5.5.

Fig. 4.61 presents the grain size distribution for C2-B3 non-isothermally annealed and taken out of the oven at 375 °C. As can be seen from the figure, the grain size distribution reveals an inhomogeneous grain structure with dominating grain size diameters between 25 µm and 70 µm. This correspond well to the varying grain sizes observed in the OIM-map and OM-

image of this specimen (see Chapter 4.3.4 and 4.3.5) and the estimated average grain size for this specimen (see Chapter 4.3.5).

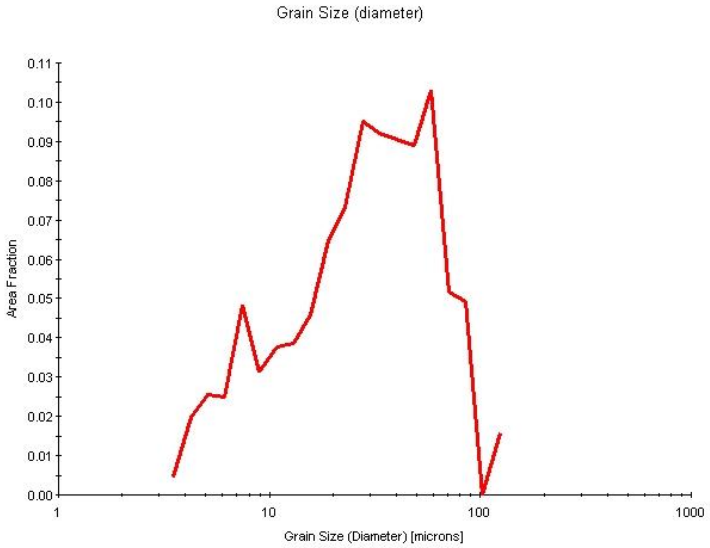

Fig. 4.61: Grain size distribution from a 80X EBSD-scan of C2-B3 non-isothermally annealed and taken out of oven at 375 °C

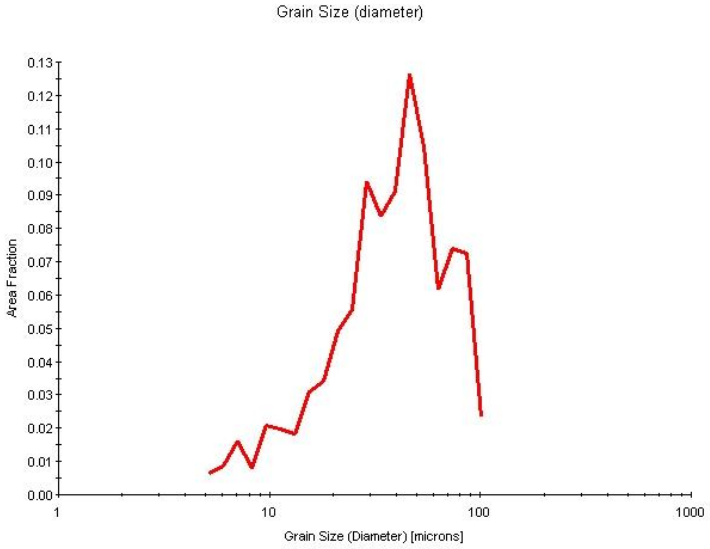

Fig. 4.72: Grain size distribution from a 80X EBSD-scan of C2-B3 non-isothermally annealed and taken out of oven at 400 °C

Fig. 4.62 presents the grain size distribution for C2-B3 non-isothermally annealed and taken out of the oven at 400 °C. The grain size distribution in Fig. 4.62 reveals a slightly inhomogeneous grain structure with dominating grain size diameters between 30 μm and 60 μm. This corresponds well to the varying grain sizes observed in the OIM-map and OM-image of this specimen (see Chapter 4.3.4 and 4.3.5) and somewhat to the estimated average grain size for this specimen (see Chapter 4.3.5).

5. Discussion

The following chapter is divided into 6 parts, where the results presented in Chapter 4 are discussed. The focus of the discussion in the first part of this chapter is on the results from the characterization of the starting alloy variants (with respect to deformation and homogenization). In the second part of this chapter a hardness phenomena observed in the softening curves is discussed. The effects of strain during the isothermal annealing procedures are discussed in the third part of this chapter, while the effects of homogenization are discussed in the fourth part. In the fifth part of this chapter the discussion is focused on the effects of concurrent precipitation during the isothermal annealing procedures. The non-isothermal annealing experiments are the topic of discussion in the sixth and final part of this chapter.

5.1 Characterization of the Starting Alloy Variants

The results from the characterization of the starting alloy variants are discussed in the following.

5.1.1 The Effects of Deformation

Electrical Conductivity

Usually it would be expected that increasing amounts of deformation would slightly reduce the conductivity due to introductions of defects, vacancies, etc. (see Chapter 2.4), which distorts the crystal lattice and consequently reduces the conductivity. But instead of a slightly reduced electrical conductivity, small inconsistent variations are observed for the first two homogenization variants (see Table 4.1 in Chapter 4.1.1.), and an increase in the conductivity for the third homogenization variant. The inconsistent variations for the first two homogenization variants can be explained by the measuring equipments sensibility to temperature (see Chapter 3.2.2), and by variations in the properties of the different specimens. The increase in electrical conductivity with increased strain for the third homogenization variant might also be due to the measuring equipments temperature sensibility, and due to variations in the properties of the different specimens. However, that will not be discussed

further since the EC values for the third homogenization variant were made available through G. Wangs PhD-work [49] as explained in Chapter 3.2.

Hardness

As described in Chapter 4.1.1, the hardness increased substantially with increasing strain for all three homogenization variants. Increasing deformation introduces increased amounts of plastic deformation and stored energy in the alloy (see Chapter 2.4), and consequently the hardness and strength of the material increased with increasing deformation.

5.1.2 The Effects of the Homogenization Procedures

As mentioned in Chapter 2.3, one of the main goals of homogenization is to reduce Mn in solid solution. Mn in solid solution has a strong influence on the mechanical properties of the alloy, and as can be seen from Table 4.2 in Chapter 4.1.2, there is a significant difference between the estimated amounts of Mn in solid solution in the three homogenization variants of the C2-alloy. The Mn content in solid solution was approximated to be reduced from 0.85 wt% to 0.55 wt% during homogenization procedure nr. 2 (see Chapter 3.3.1, Table 4.2 and Chapter 4.1.2). As a comparison, Knut Sjølstad [8] reduced the Mn content in solid solution from 0.80 wt% to 0.59 wt% in an alloy similar to the C2-alloy (see Chapter 2.3) by a homogenization procedure similar to homogenization procedure nr. 2 (see Chapter 2.3). The Mn content in solid solution was approximated to be reduced from 0.85 wt% to 0.49 wt% during homogenization procedure nr. 3 (see Chapter 3.3, Table 4.2 and Chapter 4.1.2). Homogenization procedure nr. 3 resulted in less Mn in solid solution than homogenization procedure nr. 2. The reason for this might be that homogenization procedure nr. 2 mainly resulted in growth of constituent particles, while the holding time at both 500 °C and 600 °C in homogenization procedure nr. 3 resulted in dispersoids and growth of constituent particles (with a larger total reduction of Mn in solid solution), this in accordance to the results of Li and Arnberg [9] (see Chapter 2.3).

The different amounts of Mn in solid solution in the three homogenization variants affected both the electrical conductivity and the hardness of the three variants, which is further discussed in the following.

Electrical Conductivity

There are obvious differences between the electrical conductivities of the different homogenization variants of the C2-alloy, as can be seen from Table 4.1 in Chapter 4.1.1 and Table 4.2 in Chapter 4.1.2. These differences are due to the different amounts of Mn in solid solution (see Table 4.2 in Chapter 4.1.2 for approximated values in wt%). Mn in solid solution lowers the electrical conductivity through distortion of the atomic lattice of the alloy (see Chapter 2.7.2). And since the amount of Mn in solid solution is reduced during homogenization, the electrical conductivity increases from the as cast specimens (C2-A1, C2-A2 and C2-A3) to the homogenised specimens (C2-B1, C2-B2, C2-B3, C2-C1 and C2-C3); less distortion of the atomic lattice and consequently a higher conductivity.

Homogenization procedure nr. 2 and homogenization procedure nr. 3 resulted in an increase in conductivity from 17.5 m/Ωmm^2 (as cast material with $\varepsilon = 0$) to 21.5 m/Ωmm^2 and 22.5 m/Ωmm^2 respectively. The difference in resulting electrical conductivity after hom. proc. nr. 2 and nr. 3 might be explained by that hom. proc. nr. 2 mainly results in growth of constituent particles, while hom. proc. nr. 3 results in dispersoids and growth of constituent particles (with a larger total reduction of Mn in solid solution), as discussed earlier in this chapter.

Hardness

As presented in Chapter 4.1.1, the hardness of the unstrained alloy variants was reduced from 37.0 HV to 30.2 HV when the as cast variant was homogenised with homogenization procedure nr. 2. This can be explained by the fact that the amount of Mn in solid solution has a significant influence on the hardness. The C2-B1 specimens have a smaller amount of Mn in solid solution (approx. 0.55 wt%) than the C2-A1 specimens (approx. 0.85 wt%), and this cause the C2-B1 specimens to be softer since Mn contributes to strength and hardness through

solid solution strengthening (see Chapter 2.2). According to Table 4.1 there is little difference between the hardness of C2-A1 (37.0 HV) and C2-C1 (37.9 HV) even though there is a large difference in the amount of Mn in solid solution. The lower amount of strength contributing Mn in solid solution should result in a lower hardness for C2-C1 compared to C2-A1, but since homogenization procedure nr. 3 is expected to result in a high amount of strength contributing dispersoids (see Chapter 2.1 and Chapter 3.1), the dispersoids negate the hardness reduction due to the lower amount of Mn in solid solution.

5.1.3 Deformation Texture

As described in Chapter 4.1.3, only C2-B2 and C2-B3 were investigated with respect to the deformation texture, which means that nothing can be said about the effect of the different homogenization procedures or the amount of Mn in solid solution on the deformation textures. However, something can be said about the effect of strain on the texture development in the nr. 2 homogenization variants. As already mentioned in Chapter 4.1.3, the OIM-maps in Fig. 4.1 and 4.4, representing C2-B2 and C2-B3, show a typical cold rolled grain structure development. Fig. 4.1 ($\varepsilon = 0.7$) show starting grain elongation in the rolling direction and small indications of grain fragmentation, while Fig. 4.4 ($\varepsilon = 3.0$) show a largely deformed grain structure with much grain elongation and much grain fragmentation. The development of a cold rolled microstructure can also be seen in the pole figures in Fig. 4.3 and 4.6. The pole figure in Fig. 4.3 (C2-B2) is relatively weak and a bit unclear, but it definitely has some of the characteristics of a rolling texture pole figure. These characteristics are much clearer in the pole figure in Fig. 4.6 (C2-B3) and the texture is also slightly stronger, as expected with the much higher degree of strain for C2-B3. The ODF in Fig. 4.2 (C2-B2) presents a strong but not very well defined texture. In addition to typical deformation texture components like strong Cu- and S-components, and a weak Brass component (see Chapter 2.6.1 for deformation texture examples), there is also some other undefined texture elements from before deformation due to a strain of only 0.7. These undefined texture elements are not present in the ODF in Fig. 4.5 (C2-B3), where the texture is strong and composed of strong Cu- and S-components, and some weak Brass texture (see Chapter 2.6.1 for deformation texture examples).

5.2 Cluster Formation

As described in Chapter 4.2.1, the hardness showed a tendency of increasing at the early stages of annealing at 300 °C and 350 °C, and also during the non-isothermal annealing procedures (see Chapter 4.3.1). This is an effect sometimes observed for AlMn-alloys and the effect is probably due to cluster formation of the solute atoms in the alloy (see Chapter 2.5 and the work by Sæter [14]). The effect is found to be less significant with increasing annealing temperatures, most probably due to an increased recovery rate. In this work, the effect is also observed to be less significant for C2-B2 and C2-B3 during isothermal annealing than for the as cast variants. This can probably be explained by the fact that the solid solution level before annealing is lower for C2-B2 and C2-B3, which means that there is less potential for cluster formation in these specimens.

5.3 The Effects of Strain during Isothermal Annealing

The effects of strain seen in this work are due to the different degrees of stored energy through plastic deformation in the different strain variants of the C2-alloy.

5.3.1 The Effect of Strain on Recovery and Recrystallization Behavior

The effective driving force for recovery and recrystallization (and also the rate and possibly the amount of precipitation) is increased with the introduction of more dislocations (see Chapter 2.4). The stored energy in the material (and the driving force for the reactions during annealing) is described by Equation 2.1 (see Chapter 2.4). The effective driving force for recrystallization is described by $P = P_D - P_Z$, where P_Z is the Zener drag (see Chapter 2.5.1). As can be seen from this equation the effective driving force for recrystallization will increase with the increased stored energy (P_D) introduced during deformation. This effect was observed for both the as cast variants (C2-A2 and C2-A3) and the hom. nr. 2 variants (C2-B2 and C2-B3) in the isothermal annealing experiments. As described in Chapter 4.2.1, the softening curves show faster and more extensive recovery- and recrystallization processes with increased strain. This effect of strain can also clearly be seen in the TTT-diagrams in Chapter 4.2.3, where both the start and end of recrystallization are shifted towards

significantly shorter annealing times for the high strain specimens. As an example, no recrystallization was observed for any of the isothermal annealing procedures for C2-A2 (ε = 0.7), while C2-A3 (ε = 3.0) was clearly recrystallised during the isothermal annealing at 400 °C, 450 °C and 500 °C.

5.3.2 The Effect of Strain on the Precipitation Behavior

Increased strain was also found to increase the rate and (generally) the amount of precipitation, as described in Chapter 4.2.2. The EC curves in Chapter 4.2.2 show a faster and more extensive increase in electrical conductivity for the high strain variants compared to the low strain variants. This effect of strain can also clearly be seen in the TTT-diagrams in Chapter 4.2.3, where the start of precipitation is shifted towards significantly shorter annealing times for the high strain specimens.

A larger number of dislocations cause the precipitation reactions to go faster because the diffusion goes faster (pipe diffusion along the dislocations). Moreover, more dislocations also provide more heterogeneous nucleation sites which increase the nucleation rate of precipitation (see Chapter 2.4 and Chapter 2.5.1).

5.3.3 The Effect of Strain on the Recrystallised Grain Size

By comparing the final recrystallised grain size for C2-B2 and C2-B3 at the same annealing temperatures, the grain size is seen to be reduced with increasing strain, as expected, since increased strain leads to a larger density of active nuclei (see Chapter 2.4).

Increased strain results in an increased stored energy in the material, which means that P_D is increased (see Equation 2.1). Consequently the effective driving force, $P = P_D - P_Z$, for recrystallization is increased. A higher P results in a smaller R_C, as can be seen from Equation 2.5. A smaller critical radius for nucleation leads to more nucleation of recrystallization, and

consequently a higher N_{TOT}. A higher N_{TOT} results in a smaller recrystallised grain size as seen from Equation 2.9.

5.4 The Effects of Homogenization during Isothermal Annealing

The effects of the homogenization procedures seen in the isothermal annealing experiments are due to the different final amounts of manganese in solid solution after homogenization.

5.4.1 The Effect of the Different Final Amounts of Manganese in Solid Solution on the Precipitation Behavior

As can be seen from Table 3.2 in Chapter 3.1, a high amount of Mn in solid solution was expected for the as cast variant, while a medium amount of Mn in solid solution was expected for the hom. nr. 2 variant of the C2-alloy. As described in Chapter 4.3, the amount of Mn in solid solution for the as cast variant and the hom. nr. 2 variant were estimated to be 0.85 wt% and 0.55 wt% respectively. This difference proved to be quite crucial for the annealing behavior of the two variants.

As described in Chapter 4.2.2, the conductivity increased extensively for the as cast variants during the isothermal annealing procedures, indicating considerable precipitation. The conductivity is observed to increase both less and at a lower rate for C2-B2 and C2-B3 compared to the as cast variants, indicating slower precipitation and also less precipitation for C2-B2 and C2-B3. This effect is also seen in the TTT-diagrams in Chapter 4.2.3, where the start of precipitation is shifted to significantly longer annealing times for C2-B2 and C2-B3 compared to the as cast variants, illustrated in Fig. 5.1 below.

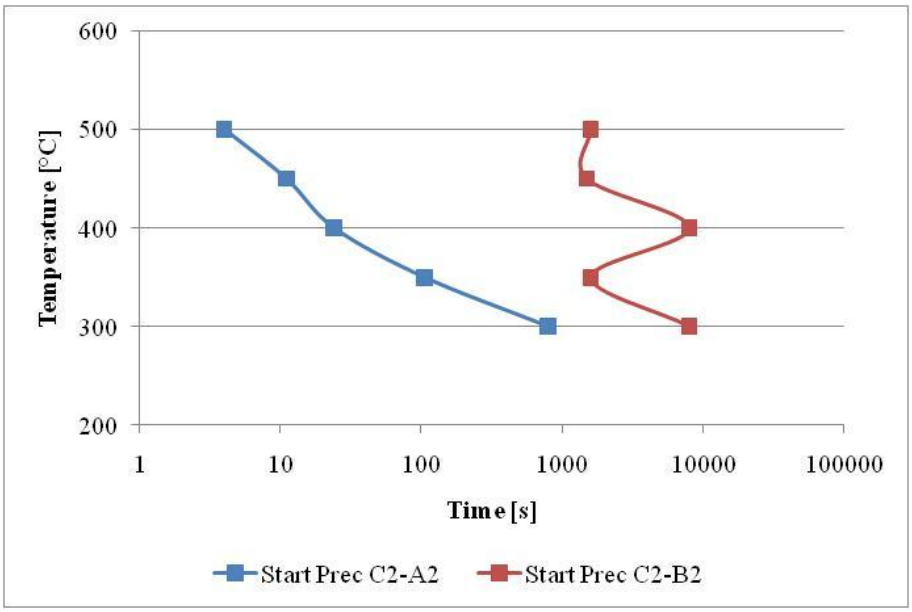

Fig. 5.1: TTT-diagram illustrating the difference in precipitation behavior for the as cast variants and the hom. nr. 2 variants

Precipitation occurs extensively during annealing for the as cast variants due to the high amount of manganese in solid solution; high supersaturation of Mn and thus a high potential for precipitation. The supersaturated solid solution decomposes during annealing, and the Mn contributes to the formation of dispersoids. Since homogenization procedure nr. 2 has reduced the amount of Mn in solid solution for C2-B2 and C2-B3, precipitation occurs to a much less significant degree during annealing of these specimens; less supersaturation and thus less potential for precipitation.

The effects of the difference in precipitation behavior between the as cast variants and the hom. nr. 2 variants are further discussed in Chapter 5.5.

5.5 Concurrent Precipitation during Isothermal Annealing

5.5.1 The Effects of Concurrent Precipitation on Recrystallization

As can be seen from the TTT-diagrams in Chapter 4.2.3, both the start and end of the recrystallization processes are shifted towards significantly longer annealing times (or are fully suppressed) in the case of concurrent precipitation. This is illustrated in Fig. 5.2, where the start of the recrystallization curves for C2-A2 and C2-B2 from the TTT-diagrams in Chapter 4.2.3 are plotted together. C2-A2 is severely affected by concurrent precipitation, while C2-B2 is practically not affected by concurrent precipitation (according to the TTT-diagrams in Chapter 4.2.3), due to the different amounts of Mn in solid solution, as discussed in Chapter 5.4.

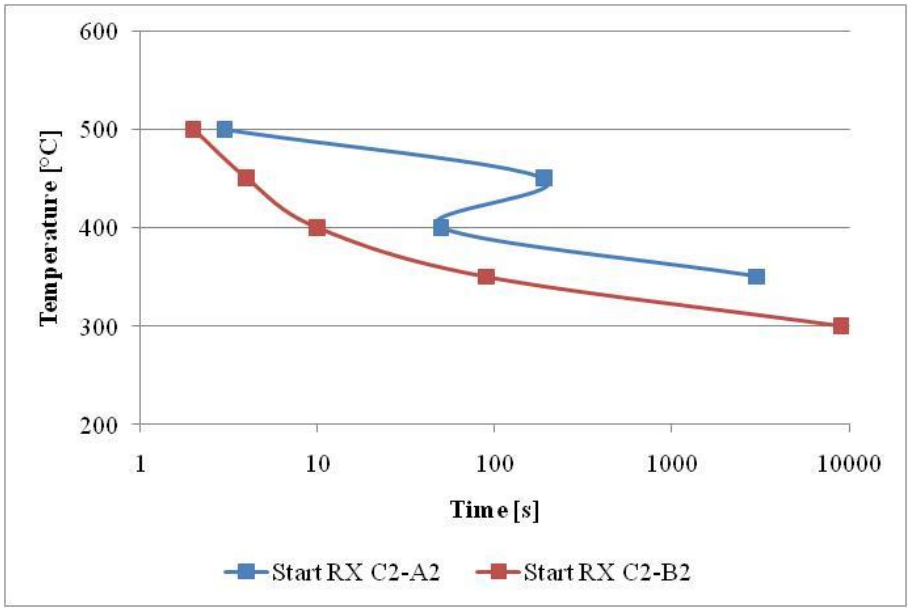

Fig. 5.2: The effect of concurrent precipitation illustrated by the start of recrystallization curves for C2-A2 and C2-B2 in a TTT-diagram

The dispersoids formed during concurrent precipitation prevents recrystallization by preventing subgrain-growth during recovery and they also slow down any occurring recrystallization by grain boundary pinning (see Chapter 2.5.1). The result is, as mentioned above, a recrystallization process shifted towards longer annealing times (or a fully suppressed recrystallization process). This is clearly observed for the as cast variants (C2-A2 and C2-A3) in the TTT-diagrams in Chapter 4.2.3. No (or less) concurrent precipitation (as

seen for C2-B2 in Fig. 5.2 above and for C2-B3 in Chapter 4.2.3) leads to a small P_Z (see Chapter 2.5.1), which further leads to a smaller critical nucleation radius for nucleation of recrystallization (see Equation 2.3) and less grain boundary pinning during recrystallization. And consequently a larger effective driving force ($P = P_D - P_Z$) for recrystallization.

5.5.2 The Effects of Concurrent Precipitation on the Recrystallised Grain Size, Grain Shape and Grain Size Distribution

The recrystallised grain sizes are presented in Table 4.3 in Chapter 4.2.5, the OM-images of the recrystallised specimens are presented in Chapter 4.2.4 and the grain size distributions are presented in Chapter 4.2.6. The effects of concurrent precipitation on the recrystallised grain size as a function of annealing temperature is summarized in Fig. 5.3 and Fig. 5.4 below.

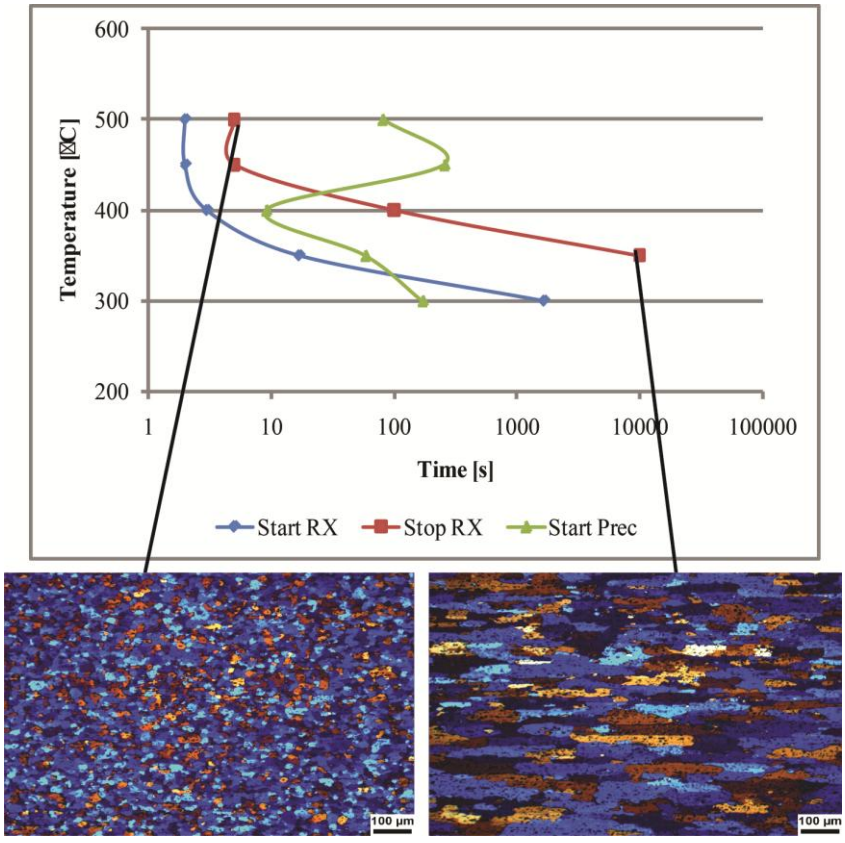

Fig. 5.3: Illustration of the effects of annealing temperature and concurrent precipitation on the resulting recrystallised grain structure (C2-B3)

Fig. 5.3 presents the TTT-diagram for C2-B3 and the recrystallised grain sizes after annealing at a high and a low temperature, where concurrent precipitation occurs at the low annealing temperature. Fig. 5.4 presents the TTT-diagram for C2-A3 and the recrystallised grain sizes after annealing at a high and a low temperature, where the high temperature annealing is done at T_C (where some concurrent precipitation occurs), while the low temperature annealing is performed at a temperature with considerable concurrent precipitation.

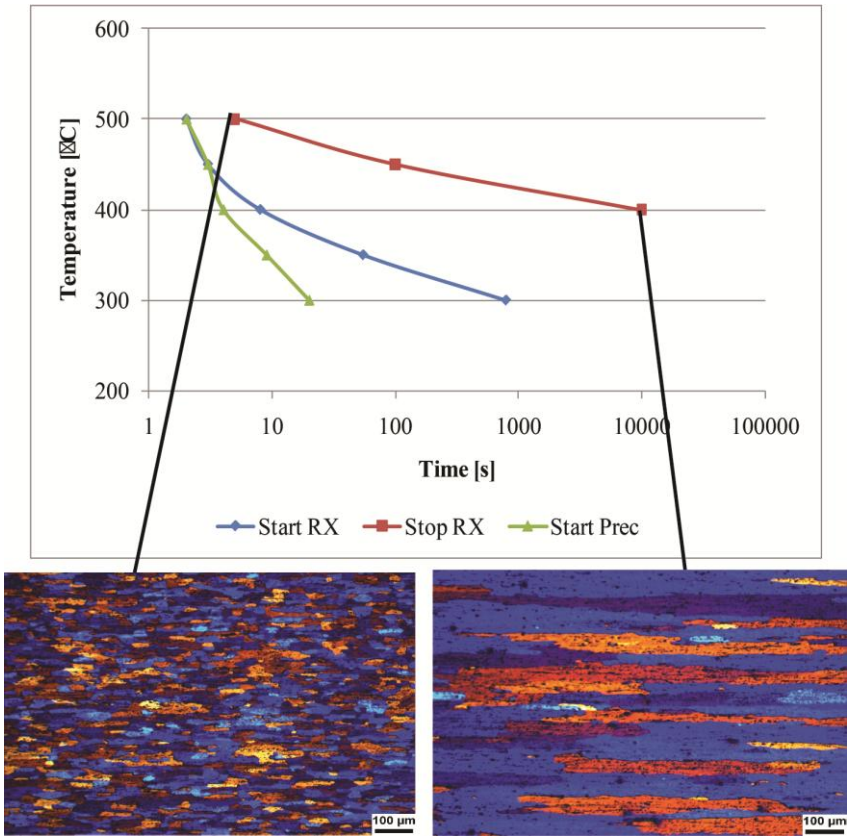

Fig. 5.4: Illustration of the effects of annealing temperature and concurrent precipitation on the resulting recrystallised grain structure (C2-A3)

From Fig. 5.3 and Fig. 5.4 it is clear that high temperatures and no (or little) concurrent precipitation resulted in fine grained and equiaxed grain sizes, while low temperatures and concurrent precipitation resulted in coarse grains elongated in the RD-direction. No (or little) precipitation results in a small value for the Zener drag, P_Z (see Chapter 2.5.1). Consequently the effective driving force, $P = P_D - P_Z$, for recrystallization remains high. A high value for P results in a small R_C, as can be seen from Equation 2.5. A small critical radius for nucleation leads to more nucleation of recrystallization, which leads to a small recrystallised grain size,

as seen from Equation 2.9. In the case of much precipitation, the result will be a large recrystallised grain size.

In addition, as can be seen from the recrystallised grain size distributions in Chapter 4.2.6, resulted low temperatures and concurrent precipitation in more inhomogeneous grain sizes than high temperatures and no (or little) concurrent precipitation. These results are consistent with what Stian Tangen reported in his Dr. Ing. thesis [2].

The very small recrystallised grain sizes (see Chapter 4.2.5) for C2-B3 annealed at 450 °C and 500 °C indicates no concurrent precipitation consistent with the TTT-diagram for C2-B3 (see Chapter 4.2.3), while the slightly increased grain size for C2-B3 annealed at 400 °C indicates some concurrent precipitation, also consistent with the TTT-diagram for C2-B3. The equiaxed (very) small grains for C2-B2 annealed at 400 °C, 450 °C and 500 °C (see Chapter 4.2.4 and Chapter 4.2.5) indicates no concurrent precipitation consistent with the TTT-diagram for C2-B2. Due to the slightly elongated grains and slightly coarse grain structure of C2-A3 annealed at 500 °C some concurrent precipitation is expected, which is consistent with the TTT-diagram for C2-A3.

5.5.3 The Effects of Concurrent Precipitation on the Recrystallization Texture

The recrystallization textures are presented in Chapter 4.2.7 with OIM-maps and ODFs. All OIM-maps are, as previously described, consistent with the results in Chapters 4.2.4, 4.2.5 and 4.2.6 and will not be further commented or discussed. The effects of concurrent precipitation on the recrystallization textures seen in the ODFs are summarized in Fig. 5.5 – Fig. 5.7 below. The strengths of the textures are presented in Chapter 4.2.7 and are not included in Fig. 5.5 – Fig. 5.7.

Fig. 5.5 presents the TTT-diagram for C2-A3 and the $\varphi_2 = 0$ ° sections of the ODFs for C2-A3 annealed at 400 °C, 450 °C and 500 °C for 10^5 s. At 400 °C the precipitation starts before the

recrystallization and the effect is clearly seen in the φ_2 = 0 ° section of the ODF, where a relatively strong (see Chapter 4.2.7) P-texture can be seen and possibly also a relatively strong (see Chapter 4.2.7) Q-texture and a strong (see Chapter 4.2.7) ND-rotated cube texture. The annealing procedures at both 450 °C and 500 °C seem to be around the T_C temperature. Concurrent precipitation occurs at both temperatures, resulting in a medium strength (see Chapter 4.2.7) P- and ND-rotated cube texture for the annealing at 450 °C and a weak (see Chapter 4.2.7) P- and ND-rotated cube texture for the annealing at 500 °C. The strength of the P- and ND-rotated cube texture is reduced with increasing temperature; i.e. with less concurrent precipitation, this in accordance with Stian Tangens observations [2] (see Chapter 2.6.2).

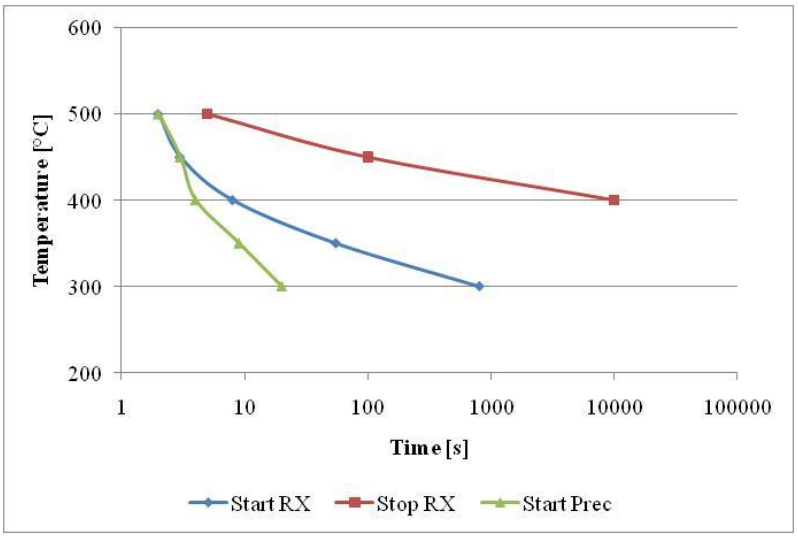

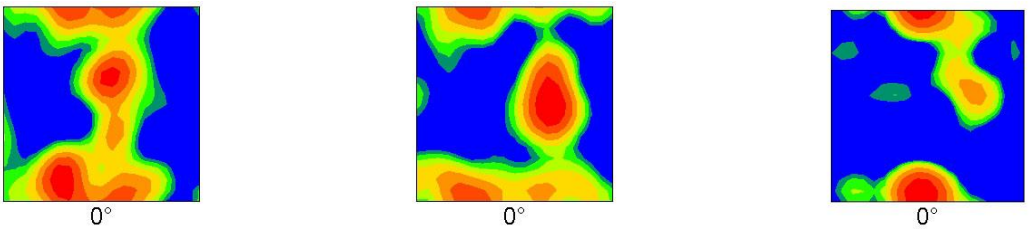

500 °C **450 °C** **400 °C**

Fig. 5.5: Illustration of the effects of annealing temperature and concurrent precipitation on the resulting recrystallization texture for C2-A3

Fig. 5.6 presents the TTT-diagram for C2-B2 and the $\varphi_2 = 0$ ° sections of the ODFs for C2-B2 annealed at 450 °C and 500 °C for 10^5 s. According to the TTT-diagram no precipitation is occurring at these temperatures, which is reflected in the texture results. Both $\varphi_2 = 0$ ° sections are showing weak and relatively random textures. A possible weak ND-rotated cube component can be seen in the $\varphi_2 = 0$ ° section of the ODF for the 500 °C, possibly indicating some concurrent precipitation. However, the general trend is clearly a weak and relatively random recrystallization texture, as expected due to the low strain (see Chapter 5.3), the low amount of Mn in solid solution (see Chapter 5.4) and consequently the reduced potential for precipitation.

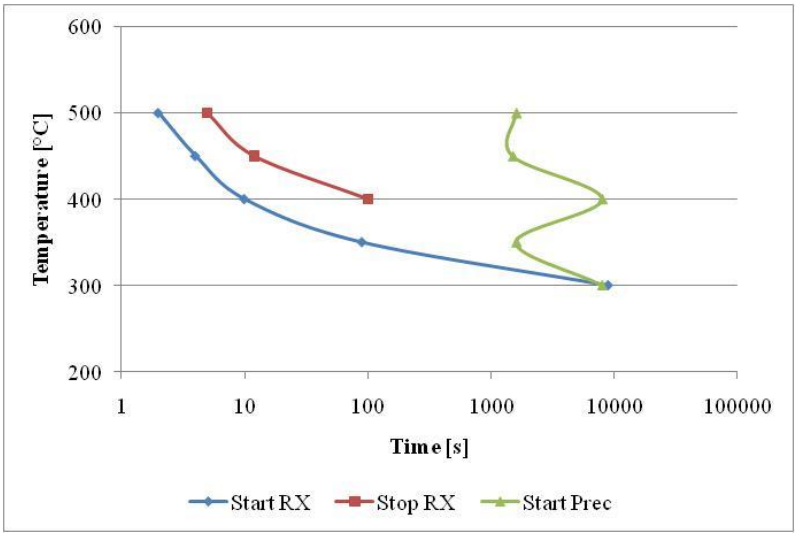

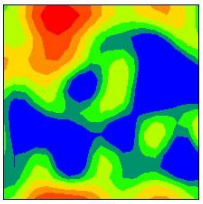

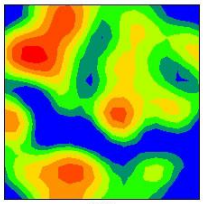

500 °C **450 °C**

Fig. 5.6: Illustration of the effects of annealing temperature and concurrent precipitation on the resulting recrystallization texture for C2-B2

Fig. 5.7 presents the TTT-diagram for C2-B3 and the $\varphi_2 = 0$ ° sections of the ODFs for C2-B3 annealed at 350 °C, 400 °C , 450 °C and 500 °C for 10^5 s. The $\varphi_2 = 0$ ° sections of the ODFs

presents a clear development from strong P- and ND-rotated cube components at 350 °C, where concurrent precipitation occurs to a large degree, as seen from the TTT-diagram, to weaker P- and ND-rotated cube components at 400 °C, where concurrent precipitation plays a smaller part, also as seen from the TTT-diagram. At 450 °C and 500 °C the relatively weak P- and ND-rotated cube texture has been replaced with a little stronger cube texture, indicating no concurrent precipitation, which is in accordance with the TTT-diagram.

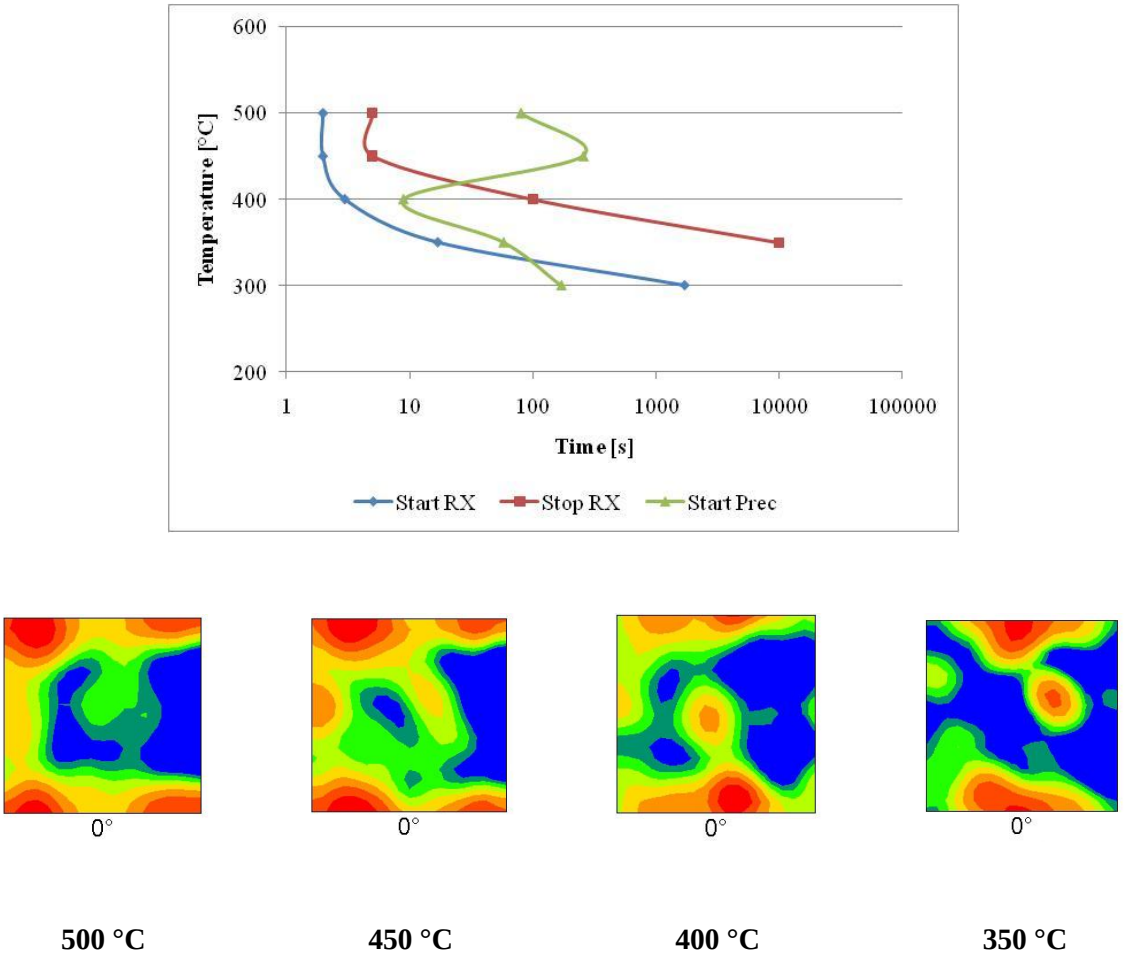

Fig. 5.7: Illustration of the effects of annealing temperature and concurrent precipitation on the resulting recrystallization texture for C2-B3

From the summarizing figures above, concurrent precipitation is seen to result in P- and ND-rotated cube texture. The P- and ND-rotated textures are also found to be stronger with increased concurrent precipitation. These results are in accordance with the observation of Daaland et al. [43] that the ND-rotated cube has a growth advance in the case of concurrent precipitation (see Chapter 2.6.2), and in accordance with the observations made by Stian

Tangen [2] (see Chapter 2.6.2). The results are also further in accordance with the previous observations of the P-texture in cold rolled and subsequently annealed 3xxx-alloys with a high supersaturation of alloying elements by Næss [44], Daaland & Nes [45], Vatne et al. [46], Engler et al. [37] and Sjølstad [8].

The high strain, the low amount of Mn in solid solution and consequently the less potential for precipitation, combined with the high annealing temperatures of 450 °C and 500 °C are seen to result in a cube texture of medium strength for C2-B3. The cube texture could also have been expected for the highest annealing temperatures for C2-B2, since C2-B2 also contains a low amount of Mn in solid solution and consequently a low potential for precipitation. But the low strain in C2-B2 compared to C2-B3 might be the reason why the cube texture does not appear in the recrystallised specimen for C2-B2.

The possible Q-texture observed for the C2-A3 might be a result of inhomogeneous deformation due to the presence of particles (see Chapter 2.6.2). Q-texture is often found in connection with the presence of P-texture, which is the case for the C2-A3 specimens.

5.6 Non-Isothermal Annealing Experiments

Non-isothermal annealing experiments were carried out to see if non-isothermal annealing programs could result in significantly different grain structures and textures (different nucleation behavior) than the isothermal annealing programs. Compared to the isothermal annealing programs the most significant difference is the much slower heating rate for the non-isothermal annealing experiments. C2-A3, C2-B3 and C2-C3 (three different homogenization variants with $\varepsilon = 3.0$) were subjected to the non-isothermal annealing procedure described in Chapter 3.3.2. The results of the non-isothermal annealing experiments are presented in Chapter 4.3 and discussed in the following.

5.6.1 The Effects of Homogenization

The effects of the homogenization procedures seen in the non-isothermal annealing experiments are due to the different final amounts of manganese in solid solution after homogenization, and due to the high amount of dispersoids in C2-C3 after homogenization.

As can be seen from Table 3.2 in Chapter 3.1, a high amount of Mn in solid solution was expected for the as cast variant, a medium amount of Mn in solid solution was expected for the hom. nr. 2 variant of the C2-alloy and a low amount of Mn in solid solution was expected for the hom. nr. 3 variant of the C2-alloy. As described in Chapter 4.3, the amount of Mn in solid solution for the as cast variant, the hom. nr. 2 variant and the hom. nr. 3 variant were estimated to be 0.85 wt%, 0.55 wt% and 0.49 wt% respectively. In addition, a high amount of dispersoids was expected for the hom. nr. 3 variant due to the homogenization procedure. These differences proved to be quite crucial for the annealing behavior of the three variants.

As described in Chapter 4.3.2, the conductivity increased extensively for C2-A3 during the non-isothermal annealing procedure, indicating considerable precipitation. The conductivity was observed to increase both less and at a lower rate for C2-C3 and C2-B3 compared to the as cast variant, indicating slower precipitation and also less precipitation for C2-C3 and C2-B3. As discussed in Chapter 5.4.1 (for the isothermal annealing procedures), precipitation occurs extensively during annealing for the as cast variant due to the high amount of manganese in solid solution; high supersaturation of Mn and thus a high potential for precipitation. The supersaturated solid solution decomposes during annealing, and the Mn contributes to the formation of dispersoids. Since homogenization procedures nr. 2 and nr. 3 have reduced the amount of Mn in solid solution for C2-C3 and C2-B3, precipitation occurs to a less significant degree during annealing of these specimens; less supersaturation and thus less potential for precipitation.

The effects of the difference in precipitation behavior are further discussed in Chapter 5.6.2.

In addition to the effects of different amounts of Mn in solid solution in the three alloy variants, the amount of dispersoids in C2-C3 after homogenization also has an effect on the annealing behavior. A large amount of dispersoids contribute to the Zener drag, P_Z (see Chapter 2.5.1). An increased P_Z lowers the effective driving force for recrystallization, $P = P_D - P_Z$. A lower P results in a larger R_C, as can be seen from Equation 2.5. Which consequently can suppress recrystallization, this especially when concurrent precipitation also takes place during softening (as will be discussed in the following chapter), which is the case for C2-C3, as seen from the EC curve in Fig. 4.48. By studying the softening curve for C2-C3 in Fig. 4.47, the OIM-maps and the ODFs for C2-C3 in Fig. 4.55 – Fig. 4.58 the effect of the dispersoids formed during homogenization becomes clear. The softening curve shows recovery and a possible recrystallization behavior, while the OIM-maps and ODFs show a combination of recrystallization and retained deformation, despite the low amount of Mn in solid solution before the annealing procedure. The dispersoids (and the concurrent precipitation during annealing) in C2-C3 hindered recrystallization and resulted in not fully recrystallised C2-C3 specimens.

5.6.2 The Effects of Concurrent Precipitation on Recrystallization

As can be seen from the softening curves for C2-A3, C2-B3 and C2-C3 for the non-isothermal annealing in Fig. 4.47, concurrent precipitation had a significant effect on the annealing behavior. The dispersoids formed during concurrent precipitation prevents recrystallization by preventing sub-grain growth during recovery and they also slow down any occurring recrystallization by grain boundary pinning (see Chapter 2.5.1). The EC curve for C2-A3 in Fig. 4.48 confirmed considerable precipitation for C2-A3 during annealing, which resulted in only recovery behavior, as seen from Fig. 4.47, and further confirmed by the OIM-map and ODF of C2-A3 in Fig. 4.49 and 4.50. The EC curve for C2-C3 in Fig. 4.48 shows less concurrent precipitation compared to C2-A3, but in combination with the already existing dispersoids in C2-C3 after homogenization (see the previous chapter), recrystallization is significantly suppressed, as seen in the OIM-maps and ODFs of C2-C3 in Fig. 4.55 – Fig. 4.58. The EC curve for C2-B3 shows the least amount of precipitation, which leads to a small P_Z (see Chapter 2.5.1) compared to C2-A3 and C2-C3, which further leads to a smaller critical nucleation radius for nucleation of recrystallization (see Equation 2.3) and less grain boundary pinning during recrystallization. And consequently a larger effective driving force ($P = P_D$ –

P_Z) for recrystallization. This is reflected in the softening curve for C2-B3 in Fig. 4.47 that shows a clear recrystallization behavior, and the OM-images, OIM-maps and ODFs of C2-B3 in Fig. 4.51 – Fig. 4.54, Fig. 4.59 and Fig. 4.60, which show a clear recrystallization structure and texture.

5.6.3 The Effects of Concurrent Precipitation on the Recrystallised Grain Structure and Texture

Since C2-A3 and C2-C3 were found to not be fully recrystallised during the non-isothermal annealing procedures, as mentioned in Chapter 4.3.3 and the two previous chapters, the discussions around grain structure and texture in this chapter will focus on C2-B3.

The grain structures of the C2-B3 specimens taken out of the oven at 375 °C and 400 °C during the non-isothermal annealing are clearly recrystallised, as can be seen from the OM-images and OIM-maps of the specimens in Fig. 4.51, Fig. 4.53, Fig. 4.59 and Fig. 4.60 (see Chapters 4.3.3 and 4.3.4). The grain structures are also, as already mentioned, significantly affected by concurrent precipitation, as can be seen from the EC curve for C2-B3 in Fig. 4.48. As a result the grain structures of both specimens consist of a combination of large grains elongated in the rolling direction and smaller more equiaxed grains. An inhomogeneous grain structure further confirmed by the grain size distributions presented in Chapter 4.3.6. These results are in accordance with the observations done in Chapter 5.5.2 regarding the recrystallised grain structures affected by concurrent precipitation (C2-B3 isothermally annealed at 350 °C).

The grain sizes for the two C2-B3 specimens were measured by the linear intercept method and the results are presented in Chapter 4.3.5. The grain sizes were found to be comparable to the grain size of C2-B3 isothermally annealed at 350 °C, a specimen also severely affected by concurrent precipitation (see Chapter 5.5).

The ODFs of both C2-B3 specimens (see Fig. 4.52 and Fig. 4.54) show ND-rotated cube components of medium strength, and the ODF for the 375 °C specimen also shows a P-texture of medium strength, both results in accordance with the texture observations done for the isothermally annealed specimens affected by concurrent precipitation (see Chapter 5.5.3). The results are also further in accordance with the observations of Daaland et al. [43] that the ND-rotated cube has a growth advance in the case of concurrent precipitation (see Chapter 2.6.2), and in accordance with the observations made by Stian Tangen [2] (see Chapter 2.6.2).

5.6.4 Evaluation of the Non-Isothermal Annealing Procedure

As mentioned in the introduction to Chapter 5.6, the motivation for the non-isothermal annealing experiments were to investigate whether a non-isothermal annealing program could result in significantly different grain structures and textures compared to the isothermal annealing programs. As seen in the results in the three previous chapters, no significantly different results were achieved compared to the isothermal annealing experiments. All three homogenization variants experienced a large degree of concurrent precipitation. Recrystallization was only achieved for C2-B3, probably due to the slow heating rate in the non-isothermal annealing procedure (50 °C/h). The recrystallised grain sizes, grain size distributions, grain shapes and textures achieved for C2-B3 samples that were non-isothermally annealed, were directly comparable to C2-B3 isothermally annealed at a low temperature.

To achieve more “desirable results” (significantly different grain structures and textures) a different annealing procedure with a higher heating rate could be the solution, which could be the topic of further work.

6. Conclusions

In this work the microstructural and texture evolution during annealing of 5 variants, with respect to strain and homogenization, of an AlMn-model alloy have been investigated. The objective has been to quantify and characterize the softening behavior for different solid solution levels of Mn and various deformation and annealing conditions. The obtained results can be summarized as follows:

- Different homogenization treatments resulted in different amounts of manganese in solid solution. Based on electrical conductivity measurements these amounts were estimated to be approximately 0.85 wt% (as cast), 0.55 wt% (hom. nr. 2) and 0.49 wt% (hom. nr. 3).

- The reductions of Mn in solid solution by hom. nr. 2 and hom. nr. 3 resulted in less concurrent precipitation and consequently a larger effective driving force for recovery and recrystallization in the hom. nr. 2 and hom. nr. 3 variants. Less Mn in solid solution leads to a decreased supersaturation and thus less potential for precipitation. The high amount of Mn in solid solution for the as cast variants resulted in much concurrent precipitation.

- Concurrent precipitation was found to delay and suppress the recovery and recrystallization processes, which is consistent with dispersoids preventing sub-grain growth and slowing down recrystallization through grain boundary pinning.

- At high annealing temperatures, with no (or little) concurrent precipitation occurring, the recrystallised grain structures were found to be homogeneous, fine grained and consisting of equiaxed grains. In these cases the recrystallised textures were found to be approximately random after a strain of 0.7, while they showed cube textures of weak and medium strength after a strain of 3.0.

- At low annealing temperatures, with concurrent precipitation occurring, the recrystallised grain structures were found to be inhomogeneous and coarse grained, with grains elongated in the rolling direction. In these cases the recrystallised textures were found to consist of P-textures and ND-rotated cube textures of medium and high strength.

- A high degree of deformation was found to increase the rate and degree of the recovery and recrystallization processes during the isothermal annealing procedures, and to result in fine recrystallised grain structures, consistent with the increased effective driving force for recovery and recrystallization. A high degree of deformation was also found to increase the rate and magnitude of precipitation during the isothermal annealing procedures.
- Annealing procedures at relatively low temperatures resulted in a small initial increase in the hardness, before the hardness started to decrease, which might indicate cluster formation of solute atoms under these conditions.
- Non-isothermal annealing experiments were carried out to see if non-isothermal annealing programs could result in significantly different grain structures and textures (different nucleation behavior) than the isothermal annealing programs. No significantly different results were achieved. Concurrent precipitation occurred for all variants non-isothermally annealed due to the slow heating rate, and the recrystallised grain sizes, grain size distributions, grain shapes and textures achieved were directly comparable to the results from the isothermal annealing experiments.
- The high amount of dispersoids in the hom. nr. 3 variants were found to reduce the effective driving force for recovery and recrystallization, which is consistent with dispersoids preventing sub-grain growth and slowing down recrystallization through grain boundary pinning.

7. References

[1]: J. Flatøy: Process and Alloy Development of Recyclable Aluminium Alloys, TMT4500 Project Work, NTNU, Trondheim, 2010, Unpublished work.

[2]: S. Tangen: Dr. Ing. Thesis, NTNU, Trondheim, 2004.

[3]: J. K. Solberg: Teknologiske Metaller og Legeringer, Compendium, NTNU, Trondheim, 2008, pp. 182-233.

[4]: E. Nes: Aluminium, 52, 1976, pp. 560.

[5]: E. Nes: Acta Met, 24, 1976, pp. 391.

[6]: Y. Kwag and J. G. Morris, Mat. Sci. and Eng., 77, 1986, pp. 59.

[7]: H. D. Merchant: Homogenization and Annealing of Al and Cu Alloys, The Metallurgical Soc. Inc., 1988.

[8]: K. Sjølstad: Dr. Ing. Thesis, NTNU, Trondheim, 2003.

[9]: Y. J. Li and L. Arnberg, TMS, San Diego, California, 2003.

[10]: http://aluminium.matter.org.uk, European Aluminium Association – MATTER - The University of Liverpool, 20 May 2011, Trondheim, Norway.

[11]: F. J. Humphreys & M. Hatherly: Recrystallization and Related Annealing Phenomena, 2nd ed., Elsevier Ltd., 2004, pp. 169-213.

[12]: K. Nord-Varhaug, B. Forbord, J. Benestad, T. Pettersen, B. Rønning, A. Bardal, S. Benum, K. Marthinsen and E. Nes: Proc. ICAA7 (ed. Starke et al.), Mater. Sci. Forum, vols. 331-337 (2000), pp. 1387.

[13]: T. Furu, R. Ørsund, E. Nes: Acta Met. Mater., 43 (1995), pp. 2209.

[14]: J. A. Sæter: Dr. Ing. Thesis, NTNU, Trondheim, 1997.

[15]: J. Hagström: Microstructural Development in cold rolled Aluminium Alloy AA3103 during annealing, Vir[FAB]-report, Team Arena, 2003.

[16]: E. Hornbogen & U. Köstner: Recrystallization of Metallic Materials, (ed. Haeßner F), Dr. Riedrer-Verlag, Stuttgart, 1978, pp. 159.

[17]: J. G. Morris & W. C. Liu: Al alloys: The influence of concurrent precipitation on recrystallization behavior, kinetics, and texture, 2005, Journal of the Minerals, Metals and Materials Society, Volume 57, Number 11, pp. 44-47.

[18]: P. C. M. Haan, J. v. Rijkom and J. A. H: Söntgerath: Proc. ICAA5 (ed. Driver et al.), Mater. Sci. Forum, vo. 217-222 (1996), pp. 765.

[19]: D. T. L. Alexander & A. L. Greer: Acta mater. 50 (2002), pp. 2571.

[20]: H. Watanabe, K. Ohori, Y. Takeuchi: Aluminium, 60 (1984), pp. 373.

[21]: Y. Li and L. Arnberg: Mat. Sci. and Eng., A347 (2003), pp. 130.

[22]: K. Ito, K. Lücke, R. Rixen: Z. Metallkunde, 67 (1976), pp. 338.

[23]: G. Hausch, P. Furrer, H. Warlimont: Z. Metallkunde, 69 (1978), pp. 174.

[24]: G. Gottstein: Physical Foundations of Materials Science, 1st ed., Springer-Verlag, Berlin Heidelberg, 2004, pp. 303-356.

[25]: O. Daaland: Dr.ing. Thesis, NTNU, Trondheim, 1993.

[26]: M. Somerday & F. J. Humphreys: Mat. Sci. and Tech., 19 (2003), pp. 20.

[27]: S. P. Bellier & R. D. Doherty: Acta Met., 25 (1977), pp. 521.

[28]: W. B. Hutchinson, A. Oskarsson, Å. Karlsson: Mater. Sci. Tech., 5 (1989), pp. 1118.

[29]: H. E. Vatne, S. Benum, R. Shahani, E. Nes: Proc. 16th Int. Risø Symp. on Mat. Sci. (eds. Hansen et al.), Risø National Laboratory, Roskilde (1995), pp. 573.

[30]: J. Hjelen & E. Nes: Proc. 7th Int. Risø Symp. on Mat. Sci. (eds. Hansen et al.), Risø National Laboratory, Roskilde (1986), pp. 361.

[31]: R. Ørsund & E. Nes: Scripta Met., 23 (1989), pp. 1187.

[32]: J. Hjelen: Dr. Scient. Thesis, The Norwegian Institute of Physics, Trondheim (1990).

[33]: E. Nes & W. B. Hutchinson: Proc. 10th Int. Risø Symp. on Metallurgy and Materials (eds. Sørensen et al.), Risø National Laboratory, Roskilde (1989), pp. 233.

[34]: F. J. Humphreys: Acta Met., 25 (1977), pp. 1323.

[35]: O. Engler, P. Yang, X. W. Kong: Acta Mat., 44 (1996), pp. 3349.

[36]: O. Engler, X. W. Kong, P. Yang: Scripta Mat., 37 (1997), pp. 1665.

[37]: O. Engler, X. W. Kong, K. Lücke: Acta Mat., 49 (2001), pp. 1701.

[38]: O. Engler: Mat. Sci. Tech., 12 (1996), pp. 859.

[39]: J. Hirsch & K. Lücke: Acta Met., 36 (1988), pp. 2883.

[40]: O. Engler: Mechanical Properties of Materials - Texture - Deformation Textures, Presentation, Hydro Aluminium, 2006.

[41]: O. Engler: Mechanical Properties of Materials - Texture - Recrystallization and Recrystallization Textures, Presentation, Hydro Aluminium, 2006.

[42]: I. L. Dillamore & H. Katoh: Met. Sci., 8 (1974), pp. 73.

[43]: O. Daaland, P. E. Dronen, H. E. Vatne, S. E. Næss and E. Nes: Proc. ReX'92 (eds. Furentes and Sevilliano), Mater. Sci. Forum, 113-115, (1993), pp. 115.

[44]: S. E. Næss: Dr. Scient. Thesis, Universitetet i Oslo, Det Matematisk-Naturvitenskapelige Fakultet, Fysisk Institutt (1990).

[45]: O. Daaland and E. Nes: Acta Mat., 44 (1996), pp. 1413.

[46]: H. E. Vatne, O. Engler and E. Nes: Mater. Sci. Tech., 13 (1997), pp. 93.

[47]: J. H. Ryu & D. N. Lee: Mat. Sci. Eng., A336 (2002), pp. 225.

[48]: D. Altenpohl: Aluminium und Aluminiumlegierungen, Springer-Verlag, Berlin, 1965, pp. 526.

[49]: G. Wang: PhD-Thesis, NTNU, Trondheim, 2010-, Unpublished work.

[50]: EDAX: OIM Analysis 5.3, Software Manual, pp. 120-122.

[51]: Personal Communication, Gavin Wang, NTNU, Trondheim, 2011.

Appendix A – Post-Processing of EBSD-data

The EBSD-data for a random specimen investigated in this work was selected and post-processed as presented in Chapter 3.5.4. A detailed study of the effect of all steps of the post-processing procedure was performed to make sure the post-processing did not affect the quality of the results. The results of this study are presented below.

Fig. A.1 – Fig A.4 shows the OIM-map, the grain size distribution, the pole figure and the ODF of the investigated specimen after the first step of the post-processing (the rotation correction).

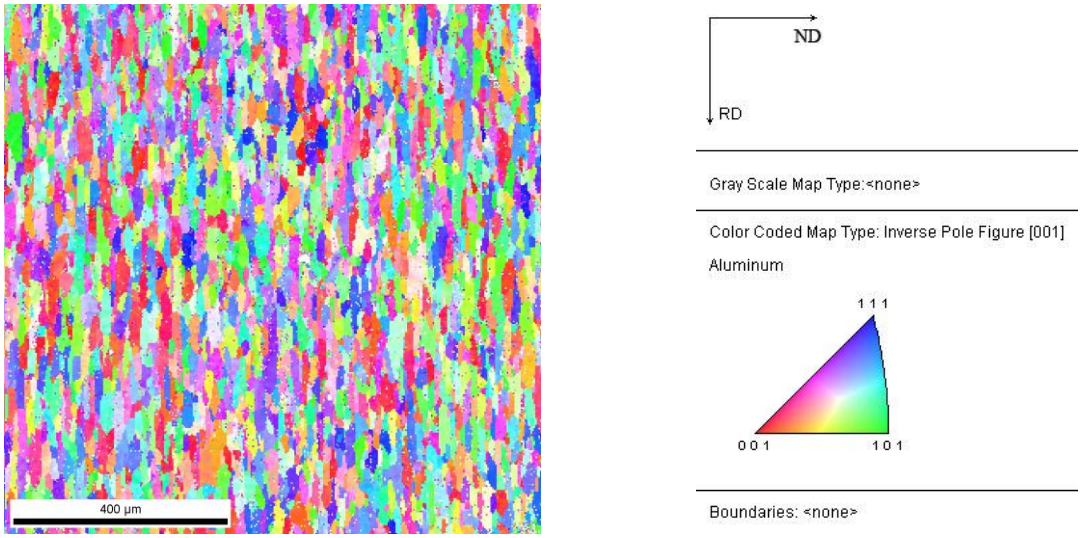

Fig. A.1: OIM-map after post-processing step 1

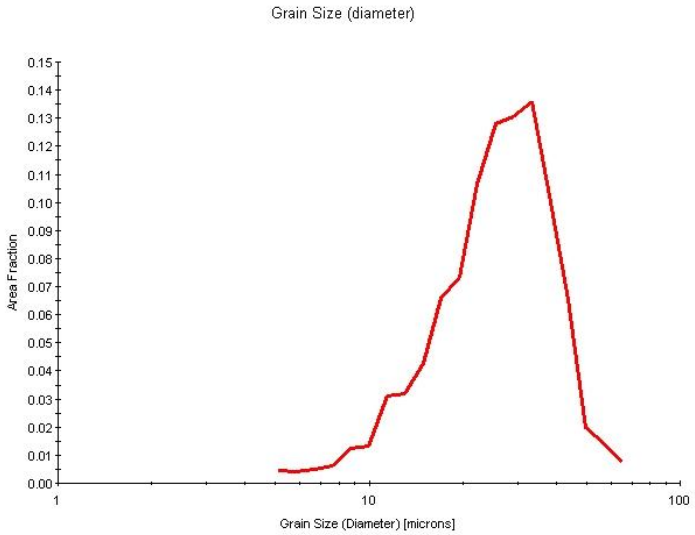

Chart: Grain Size (diameter)

Edge grains included in analysis

Diameter [microns]	Area Fraction
5.11853	0.00459945
5.85129	0.0043266
6.68897	0.00483332
7.64656	0.00628526
8.74124	0.0122295
9.99264	0.0131942
11.4232	0.0311242
13.0585	0.0317576
14.928	0.0424767
17.0651	0.0660099
19.5081	0.0734937
22.3009	0.106314
25.4935	0.128122
29.1432	0.13048
33.3153	0.13584
38.0847	0.10226
43.5369	0.0652888
49.7697	0.0200836
56.8947	0.0140225
65.0398	0.00725972

Average	
Number	16.7913
Standard Deviation	9.58496
Area	27.2179

Fig. A.2: Grain size distribution after post-processing step 1

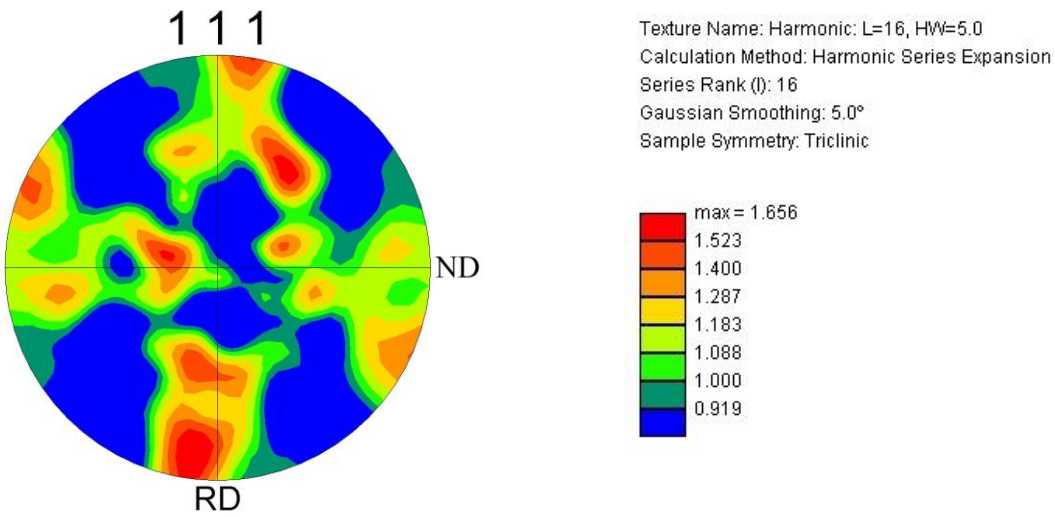

Fig. A.3: Pole figure after post-processing step 1

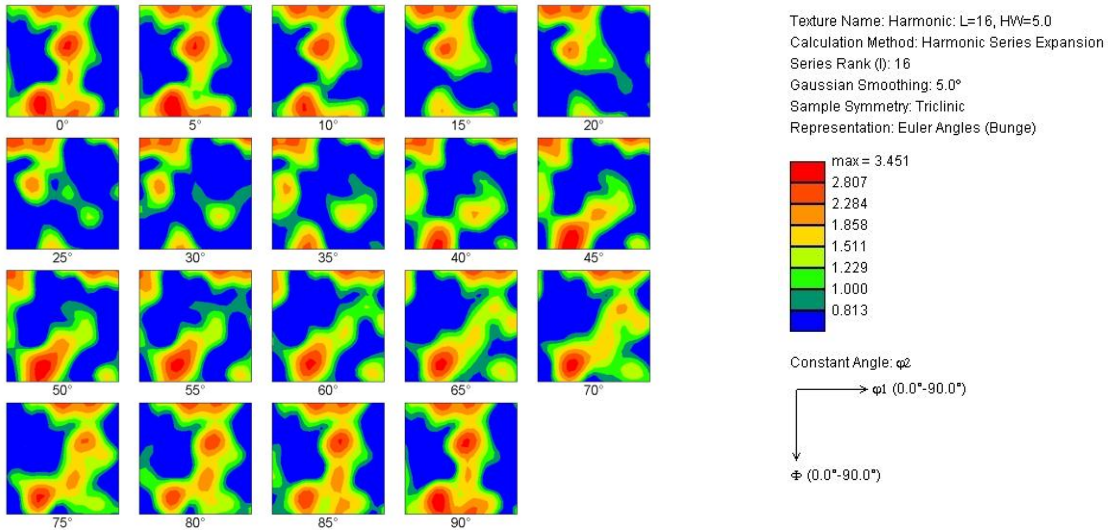

Fig. A.4: ODF after post-processing step 1

Fig. A.5 – Fig A.8 shows the OIM-map, the grain size distribution, the pole figure and the ODF of the investigated specimen after the fifth step of the post-processing procedure; after the CI standardization, the neighbor CI correlation and the grain dilations.

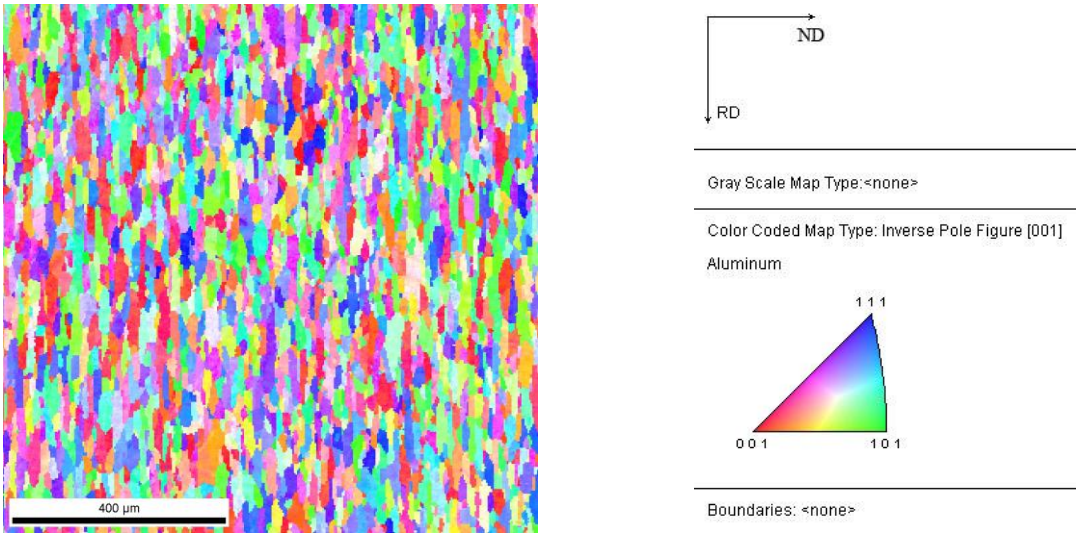

Fig. A.5: OIM-map after post-processing step 5

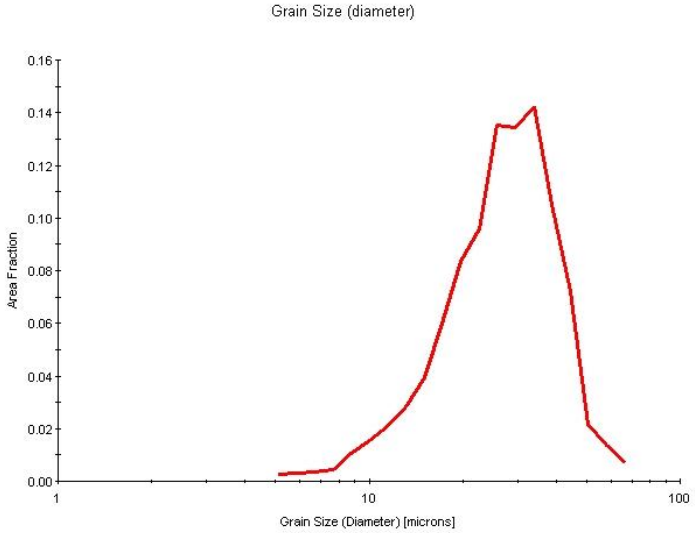

Chart: Grain Size (diameter)

Edge grains included in analysis

Diameter [microns]	Area Fraction
5.1212	0.00258185
5.86047	0.00293147
6.70645	0.00365762
7.67456	0.00421343
8.78241	0.0105067
10.0502	0.0155807
11.501	0.0213271
13.1612	0.0280955
15.0611	0.0392118
17.2352	0.061283
19.7232	0.0836142
22.5703	0.0957704
25.8285	0.135144
29.5569	0.134202
33.8236	0.142271
38.7062	0.105165
44.2936	0.0721304
50.6875	0.0216409
58.0045	0.0136802
66.3777	0.00699251

Average	
Number	18.1373
Standard Deviation	9.84211
Area	28.3148

Fig. A.6: Grain size distribution after post-processing step 5

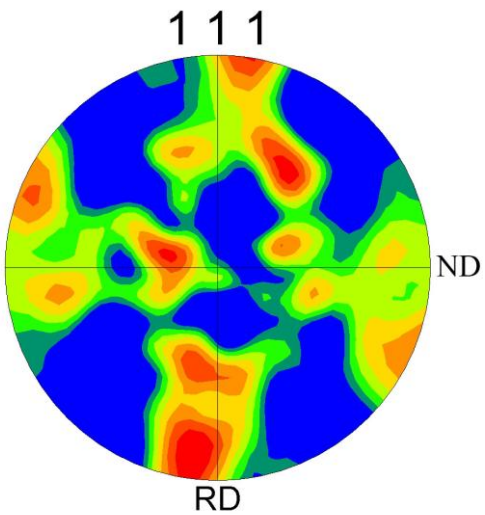

Texture Name: Harmonic: L=16, HW=5.0
Calculation Method: Harmonic Series Expansion
Series Rank (l): 16
Gaussian Smoothing: 5.0°
Sample Symmetry: Triclinic

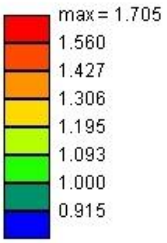

Fig. A.7: Pole figure after post-processing step 5

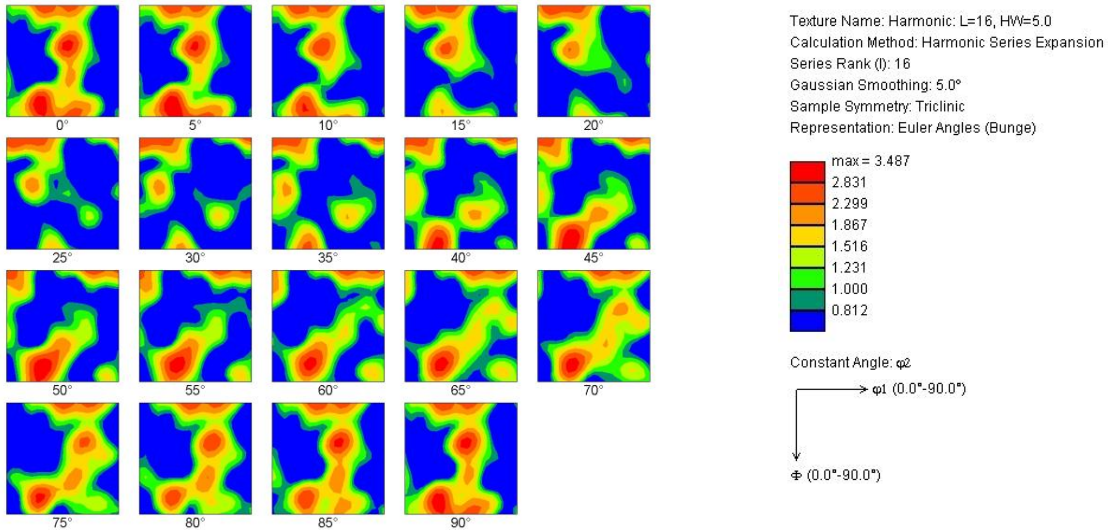

Fig. A.8: ODF after post-processing step 5

Fig. A.9 – Fig A.12 shows the OIM-map, the grain size distribution, the pole figure and the ODF of the investigated specimen after the final step of the post-processing procedure; after the single (average) orientation per grain method.

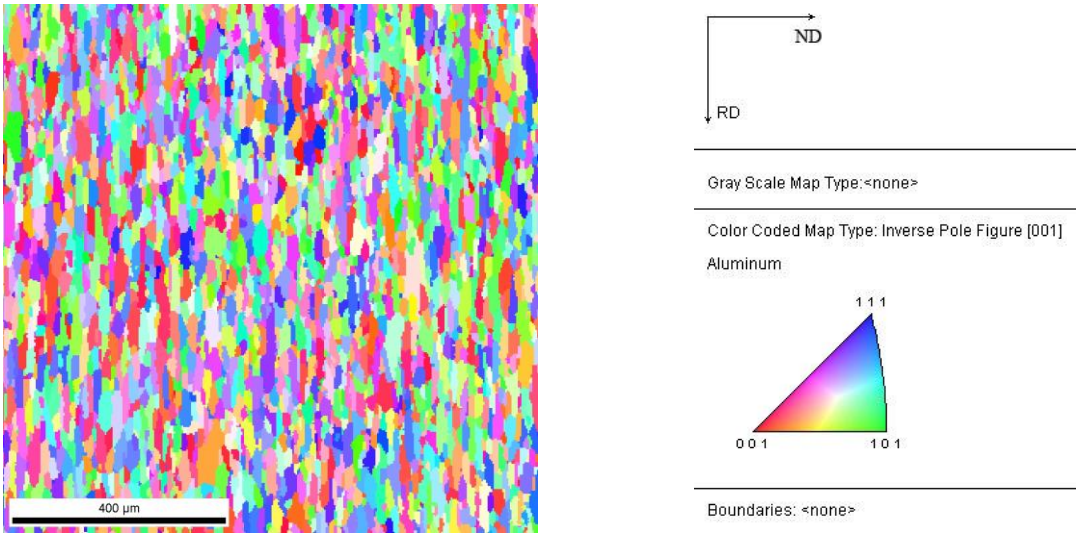

Fig. A.9: OIM-map after post-processing step 6

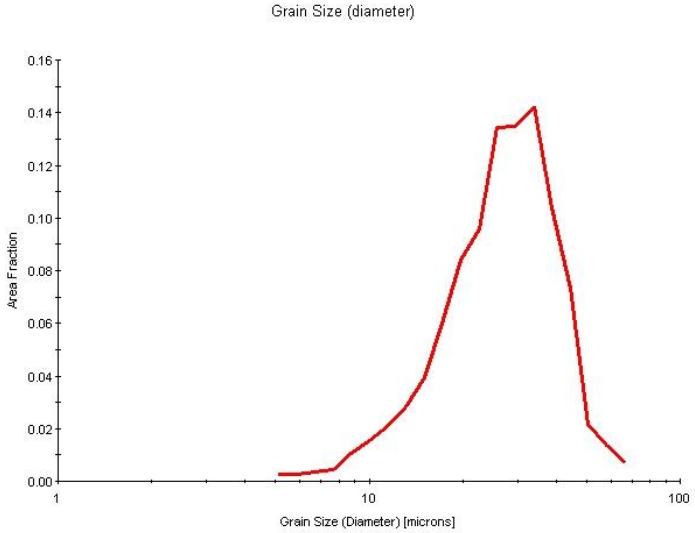

Chart: Grain Size (diameter)

Edge grains included in analysis

Diameter [microns]	Area Fraction
5.1212	0.00243841
5.86047	0.00277011
6.70645	0.00355004
7.67456	0.00421343
8.78241	0.0103901
10.0502	0.015258
11.501	0.0213451
13.1612	0.0280776
15.0611	0.0393821
17.2352	0.0613906
19.7232	0.0839011
22.5703	0.0958242
25.8285	0.134561
29.5569	0.134884
33.8236	0.142297
38.7062	0.10383
44.2936	0.0735378
50.6875	0.0216768
58.0045	0.0136802
66.3777	0.00699251

Average	
Number	18.2289
Standard Deviation	9.82536
Area	28.3338

Fig. A.10: Grain size distribution after post-processing step 6

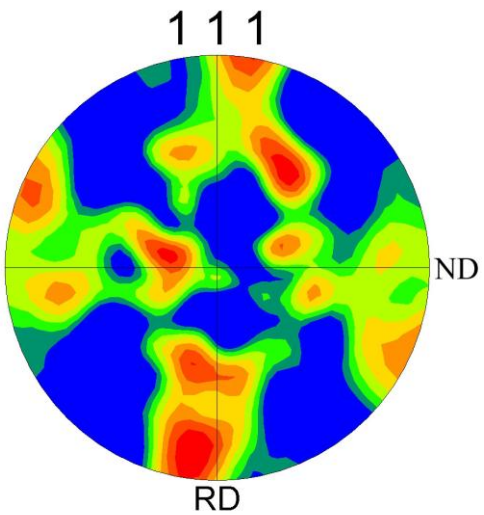

Texture Name: Harmonic: L=16, HW=5.0
Calculation Method: Harmonic Series Expansion
Series Rank (l): 16
Gaussian Smoothing: 5.0°
Sample Symmetry: Triclinic

max = 1.705
1.560
1.427
1.306
1.195
1.093
1.000
0.915

Fig. A.11: Pole figure after post-processing step 6

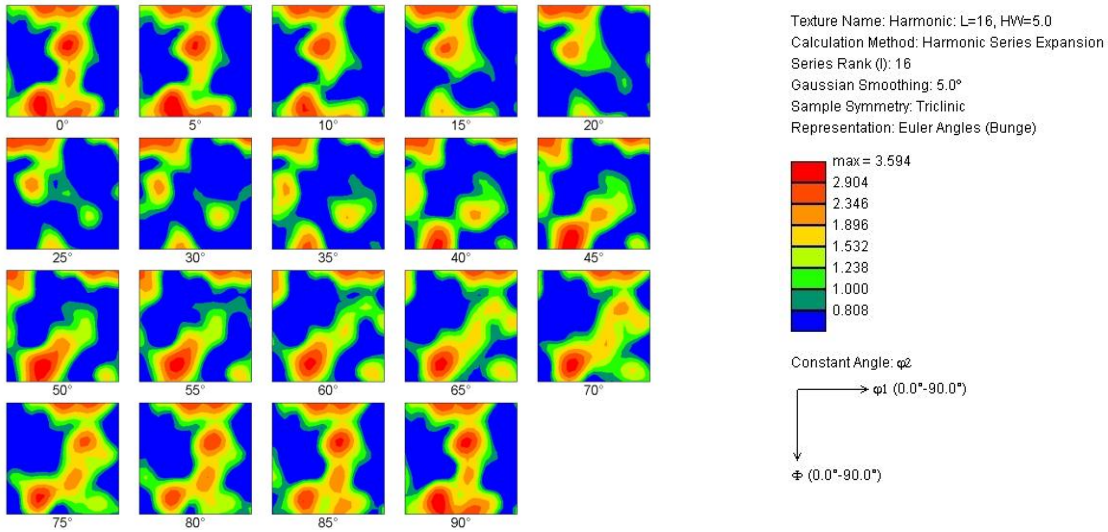

Fig. A.12: ODF after post-processing step 6

Appendix B – Calculation Examples

B.1 Amount of Manganese in Solid Solution

The amount of manganese in solid solution can be roughly approximated by using Matthiessens rule (Equation 2.11),

$$\frac{1}{\kappa} = 0{,}0267 + 0{,}036Mn + 0{,}032Fe + 0{,}0068Si \qquad \text{(B.1)}$$

and by neglecting the contributions of Fe and Si due to the low solubility of iron in aluminium, and the relative low total concentration of Si in the investigated alloy. This results in Equation B.2 below.

$$\frac{1}{\kappa} = 0{,}0267 + 0{,}036Mn \qquad \text{(B.2)}$$

By using this equation and the electrical conductivity measurements from Table 4.1 in Chapter 4.1 the amount of manganese in solid solution can be approximated. The approximation of the manganese in solid solution for as cast with ε = 0, and an electrical conductivity of 17.5 m/Ωmm^2 is shown below.

$$\frac{1}{\kappa} = 0{,}0267 + 0{,}036Mn \rightarrow \frac{1}{17{,}5} - 0{,}0267 = 0{,}036Mn$$

$$Mn = \frac{0{,}030}{0{,}036} \approx 0{,}85\%$$

Appendix C – Grain Size Distributions

C.1 Isothermally Annealed Specimens - Datasets

Complete datasets for the grain size distribution measurements on isothermally annealed specimens presented in Chapter 4.2.6 and described in Chapter 3.5.4 with accurate grain sizes and corresponding area fractions are presented in the following.

Chart: Grain Size (diameter)

Edge grains included in analysis

Diameter [microns]	Area Fraction
7.12691	0.00405157
8.88471	0.00231518
11.0761	0.00525456
13.8079	0.00327417
17.2135	0.00653699
21.4591	0.0048006
26.7519	0.00890891
33.3501	0.0127335
41.5757	0.0153892
51.83	0.0287582
64.6135	0.046349
80.55	0.0585435
100.417	0.0934471
125.184	0.0738532
156.06	0.109228
194.552	0.195673
242.536	0.136755
302.356	0.0746873
376.931	0.0427685
469.898	0.0766734

Average	
Number	32.2006
Standard Deviation	48.5657
Area	198.55

Fig. C.1: Grain size distribution for C2-A3 annealed at 400 °C for 10^5 s

Chart: Grain Size (diameter)

Edge grains included in analysis

Diameter [microns]	Area Fraction
3.47958	0.00171524
4.13601	0.00257287
4.91627	0.00537035
5.84372	0.00324263
6.94614	0.0036306
8.25654	0.00336106
9.81414	0.00610137
11.6656	0.00766551
13.8663	0.0119332
16.4822	0.0175976
19.5915	0.0339169
23.2875	0.0424278
27.6807	0.0636683
32.9027	0.0844554
39.1098	0.136088
46.4878	0.161772
55.2578	0.158648
65.6822	0.126242
78.0732	0.094902
92.8017	0.0346888

Average	
Number	17.5203
Standard Deviation	17.3727
Area	47.4944

Fig. C.2: Grain size distribution for C2-A3 annealed at 450 °C for 10^5 s

Chart: Grain Size (diameter)

Edge grains included in analysis

Diameter [microns]	Area Fraction
3.43167	0.00110962
3.96751	0.000942792
4.58702	0.00105531
5.30325	0.00235892
6.13133	0.00263051
7.0887	0.00552096
8.19556	0.00780229
9.47525	0.0117325
10.9548	0.0209044
12.6653	0.0269646
14.6429	0.0488816
16.9293	0.0699878
19.5727	0.0845914
22.6289	0.123909
26.1623	0.140418
30.2474	0.166548
34.9703	0.148527
40.4307	0.0813711
46.7438	0.0370094
54.0425	0.0177346

Average	
Number	17.1297
Standard Deviation	9.74509
Area	27.1118

Fig. C.3: Grain size distribution for C2-A3 annealed at 500 °C for 10^5 s

Chart: Grain Size (diameter)

Edge grains included in analysis

Diameter [microns]	Area Fraction
3.43985	0.00160827
3.99593	0.00218669
4.64191	0.00264283
5.39231	0.00573241
6.26403	0.00589465
7.27667	0.0132353
8.453	0.0155819
9.81951	0.021714
11.4069	0.0366799
13.2509	0.0573453
15.3931	0.0702749
17.8815	0.0882481
20.7722	0.122929
24.1302	0.136557
28.0311	0.133592
32.5626	0.120806
37.8266	0.0958944
43.9416	0.0403973
51.0451	0.0206889
59.297	0.00798964

Average	
Number	14.2235
Standard Deviation	8.86575
Area	24.7711

Fig. C.4: Grain size distribution for C2-B2 annealed at 450 °C for 10^5 s

Chart: Grain Size (diameter)

Edge grains included in analysis

Diameter [microns]	Area Fraction
3.44059	0.00130388
3.99852	0.00133351
4.64693	0.00142241
5.40049	0.00366469
6.27624	0.0035264
7.294	0.0101248
8.47681	0.0102829
9.85142	0.0195384
11.4489	0.0252132
13.3055	0.0476261
15.4632	0.0607637
17.9707	0.0919728
20.8849	0.111452
24.2716	0.147753
28.2075	0.14076
32.7817	0.129405
38.0976	0.0787661
44.2755	0.0649568
51.4553	0.032755
59.7994	0.0173801

Average	
Number	15.8076
Standard Deviation	9.47632
Area	26.6353

Fig. C.5: Grain size distribution for C2-B2 annealed at 500 °C for 10^5 s

Chart: Grain Size (diameter)

Edge grains included in analysis

Diameter [microns]	Area Fraction
6.87884	0.00302548
7.98886	0.00748322
9.278	0.0113294
10.7752	0.0311238
12.5139	0.0335699
14.5333	0.0595278
16.8785	0.0425659
19.6021	0.037223
22.7653	0.040168
26.4389	0.0445292
30.7052	0.0575484
35.6601	0.0565828
41.4145	0.0786302
48.0974	0.0928242
55.8588	0.0916655
64.8726	0.0963646
75.3409	0.0646937
87.4985	0.0845524
101.618	0.0329745
118.016	0.0336182

Average	
Number	18.6313
Standard Deviation	14.6235
Area	47.8213

Fig. C.6: Grain size distribution for C2-B3 annealed at 350 °C for 10^5 s

Chart: Grain Size (diameter)

Edge grains included in analysis

Diameter [microns]	Area Fraction
5.05879	0.00264193
5.64883	0.00835969
6.30768	0
7.04338	0.0159287
7.86489	0.0492807
8.78221	0.0352997
9.80652	0.0744755
10.9503	0.0759025
12.2275	0.115792
13.6537	0.115821
15.2462	0.0845707
17.0244	0.0938368
19.01	0.0833655
21.2273	0.0755457
23.7031	0.0737427
26.4678	0.0471498
29.5548	0.0274414
33.002	0.0117923
36.8512	0.00347115
41.1493	0.00558277

Average	
Number	11.9352
Standard Deviation	4.74356
Area	16.0633

Fig. C.7: Grain size distribution for C2-B3 annealed at 400 °C for 10^5 s

Chart: Grain Size (diameter)

Edge grains included in analysis

Diameter [microns]	Area Fraction
3.39459	0.00237138
3.84028	0.00306101
4.34449	0.00454918
4.91489	0.00522268
5.56018	0.00660598
6.2902	0.0133088
7.11607	0.0246898
8.05036	0.0275733
9.10732	0.0410958
10.3031	0.0581673
11.6558	0.0844098
13.1861	0.107531
14.9174	0.121658
16.8759	0.121731
19.0916	0.128325
21.5982	0.117609
24.4339	0.0723513
27.642	0.0391761
31.2712	0.0148493
35.3769	0.0057147

Average	
Number	11.2753
Standard Deviation	5.46446
Area	16.3278

Fig. C.8: Grain size distribution for C2-B3 annealed at 450 °C for 10^5 s

Chart: Grain Size (diameter)

Edge grains included in analysis

Diameter [microns]	Area Fraction
3.3952	0.00320793
3.84234	0.00524826
4.34837	0.00655738
4.92104	0.00731218
5.56913	0.0078547
6.30257	0.0166529
7.13261	0.026544
8.07195	0.026945
9.13501	0.0372332
10.3381	0.0539057
11.6996	0.0810827
13.2404	0.090333
14.9841	0.123863
16.9575	0.127523
19.1908	0.12724
21.7181	0.110186
24.5784	0.0775131
27.8153	0.0376499
31.4785	0.0254629
35.6241	0.00768565

Average	
Number	10.7515
Standard Deviation	5.70361
Area	16.5508

Fig. C.9: Grain size distribution for C2-B3 annealed at 500 °C for 10^5 s

C.2 Non-Isothermally Annealed Specimens - Datasets

Complete datasets for the grain size distribution measurements on non-isothermally annealed specimens presented in Chapter 4.3.6 and described in Chapter 3.5.4 with accurate grain sizes and corresponding area fractions are presented in the following.

Chart: Grain Size (diameter)

Edge grains included in analysis

Diameter [microns]	Area Fraction
3.50539	0.00459079
4.22871	0.0196668
5.10129	0.0254053
6.15392	0.0248119
7.42376	0.0484328
8.95562	0.0312131
10.8036	0.0375362
13.0329	0.038567
15.7221	0.0459036
18.9663	0.0646522
22.88	0.0731235
27.6011	0.0952459
33.2965	0.0919241
40.1671	0.0905122
48.4555	0.0889877
58.4541	0.102955
70.5158	0.0516421
85.0665	0.0491085
102.62	0
123.795	0.0157213

Average	
Number	9.36975
Standard Deviation	9.17956
Area	35.0459

Fig. C.10: Grain size distribution for C2-B3 non-isothermally annealed and taken out of oven at 375 °C

Chart: Grain Size (diameter)

Edge grains included in analysis

Diameter [microns]	Area Fraction
5.17669	0.00662778
6.05303	0.00874867
7.07772	0.0163309
8.27589	0.00800636
9.67688	0.0206964
11.315	0.0196182
13.2305	0.0181866
15.4703	0.0310622
18.0892	0.0342877
21.1515	0.0492135
24.7321	0.0556999
28.9189	0.0940438
33.8145	0.0835278
39.5388	0.0910923
46.2322	0.126555
54.0587	0.104675
63.2102	0.0616826
73.9108	0.0740986
86.4229	0.0725786
101.053	0.0232679

Average	
Number	15.5908
Standard Deviation	13.9509
Area	43.1164

Fig. C.11: Grain size distribution for C2-B3 non-isothermally annealed and taken out of oven at 400 °C

C.3 Grain Size Distributions

The grain size distributions not included in Chapter 4.2.6 are presented in the following.

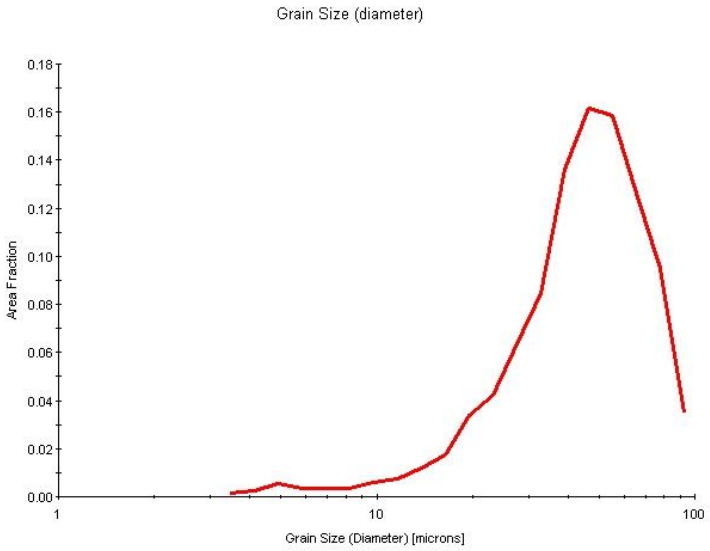

Fig. C.12: Grain size distribution for C2-A3 annealed at 450 °C for 10^5 s

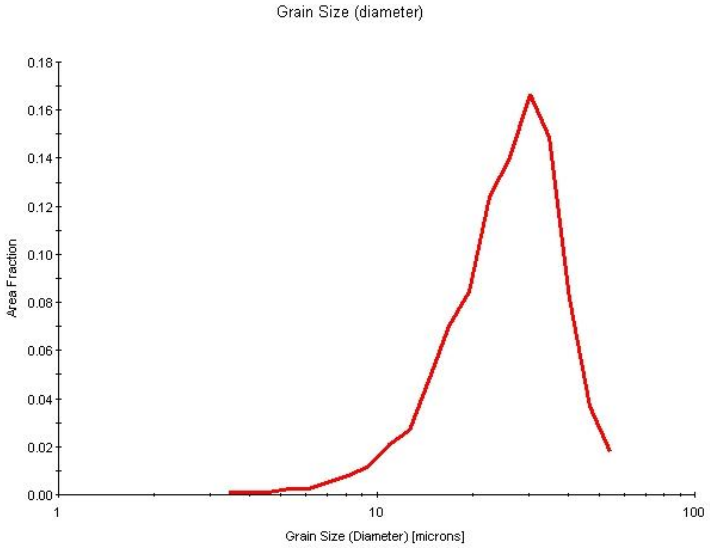

Fig. C.13: Grain size distribution for C2-A3 annealed at 500 °C for 10^5 s

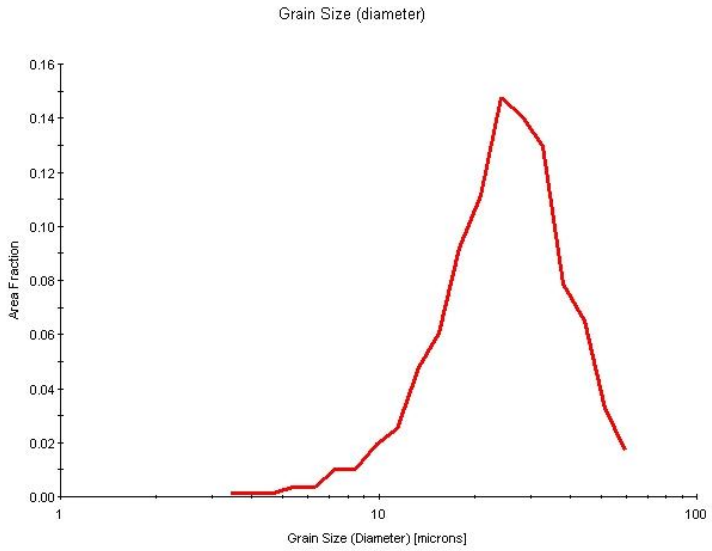

Fig. C.14: Grain size distribution for C2-B2 annealed at 500 °C for 10^5 s

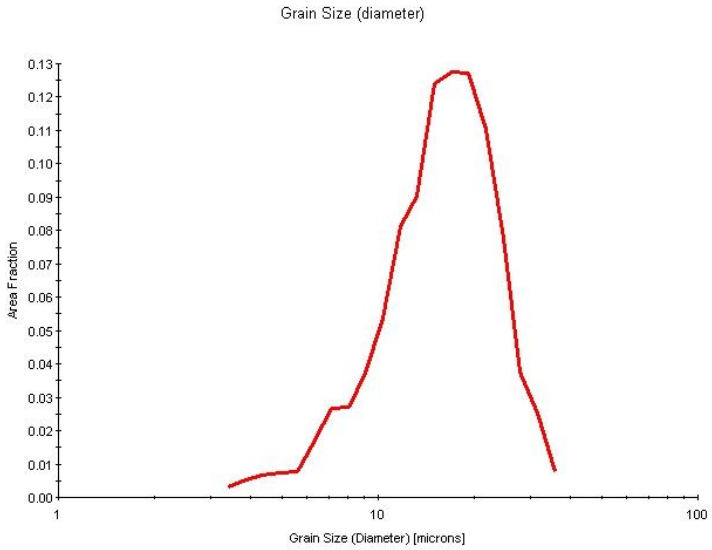

Fig. C.15: Grain size distribution for C2-B3 annealed at 500 °C for 10^5 s

Appendix D – Pole Figures

D.1 Isothermally Annealed Specimens

The pole figures from the texture measurements of the isothermally annealed specimens described in Chapter 3.5 are presented in the following.

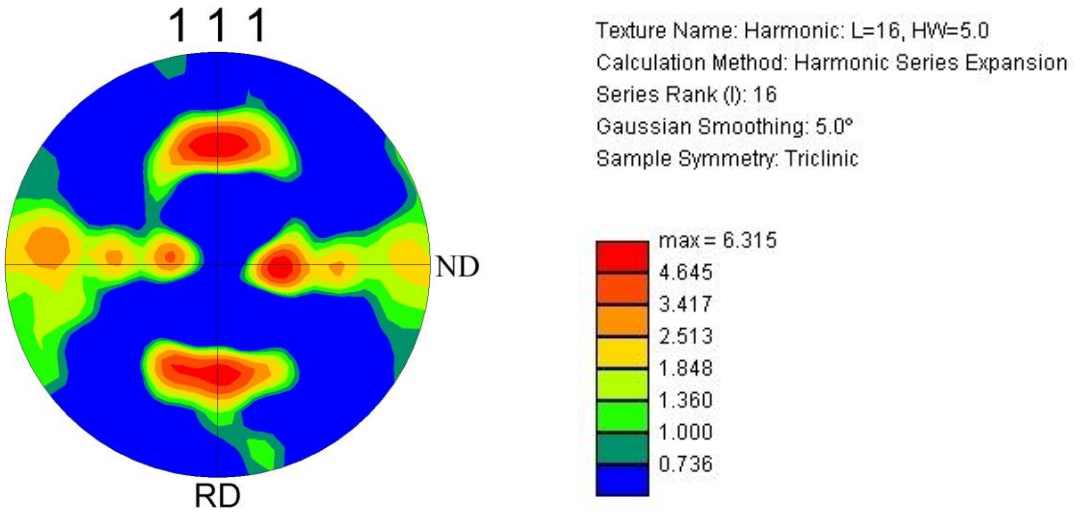

Fig. D.1: Pole figure for C2-A3 annealed at 400 °C for 10^5 s from 40X EBSD-scan

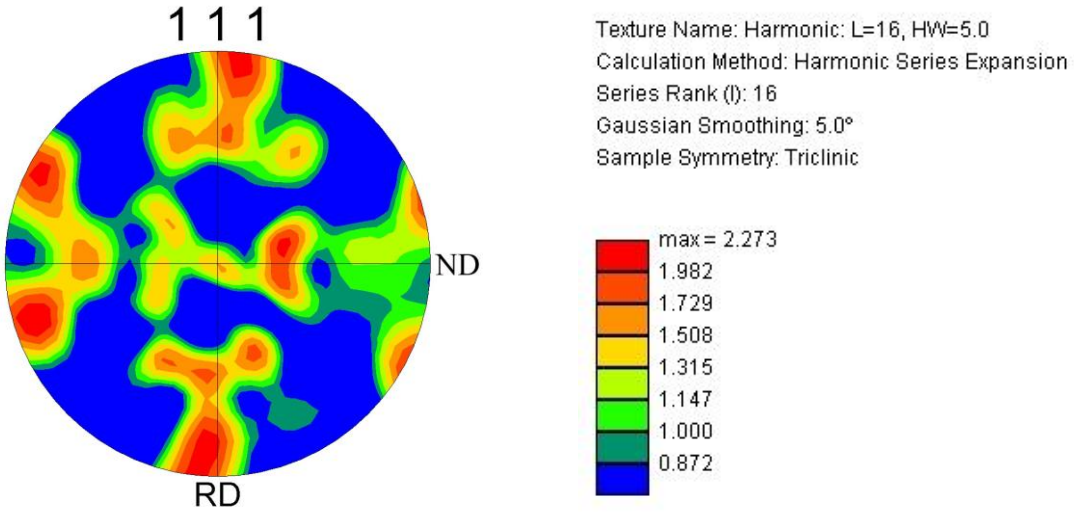

Fig. D.2: Pole figure for C2-A3 annealed at 450 °C for 10^5 s from 80X EBSD-scan

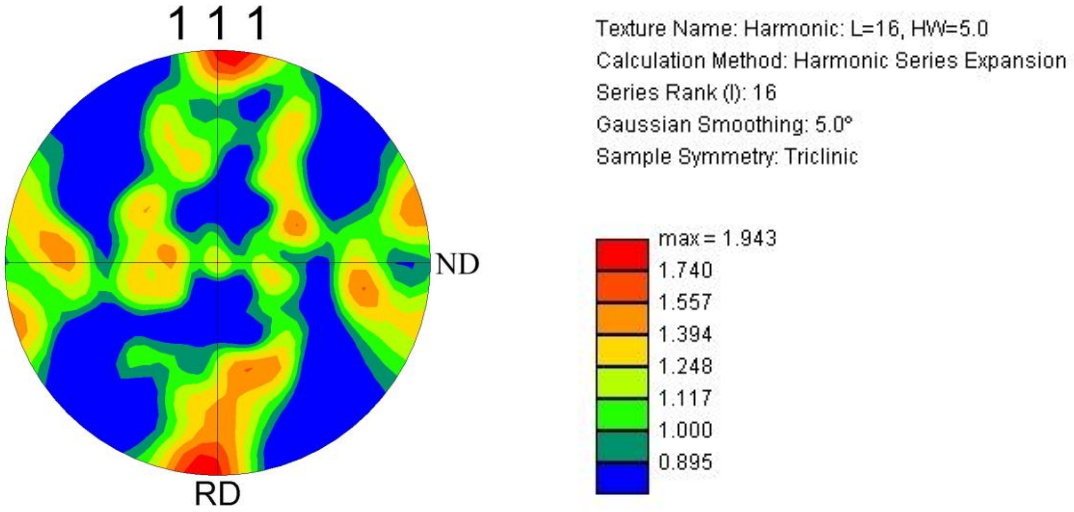

Fig. D.3: Pole figure for C2-A3 annealed at 500 °C for 10^5 s from 80X EBSD-scan

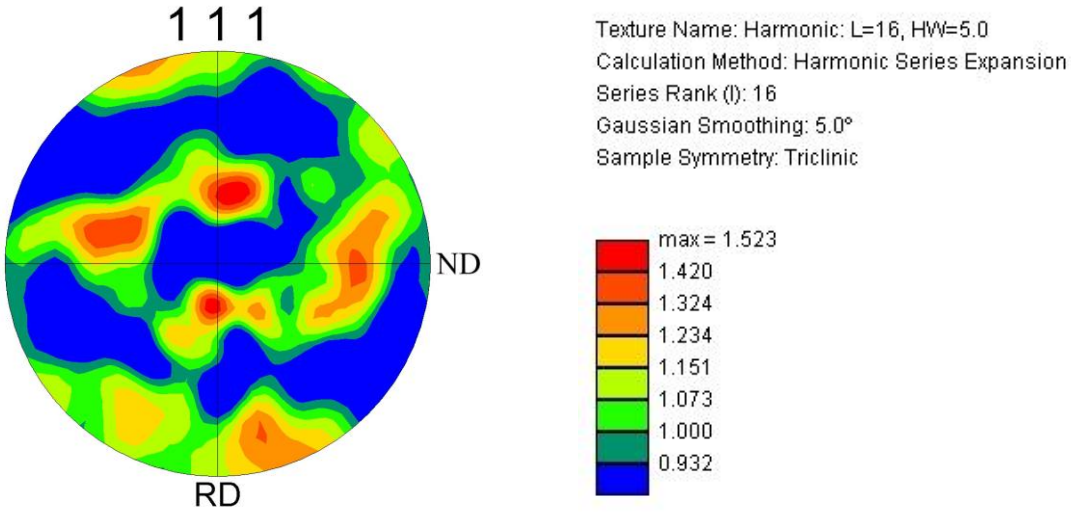

Fig. D.4: Pole figure for C2-B2 annealed at 450 °C for 10^5 s from 60X EBSD-scan

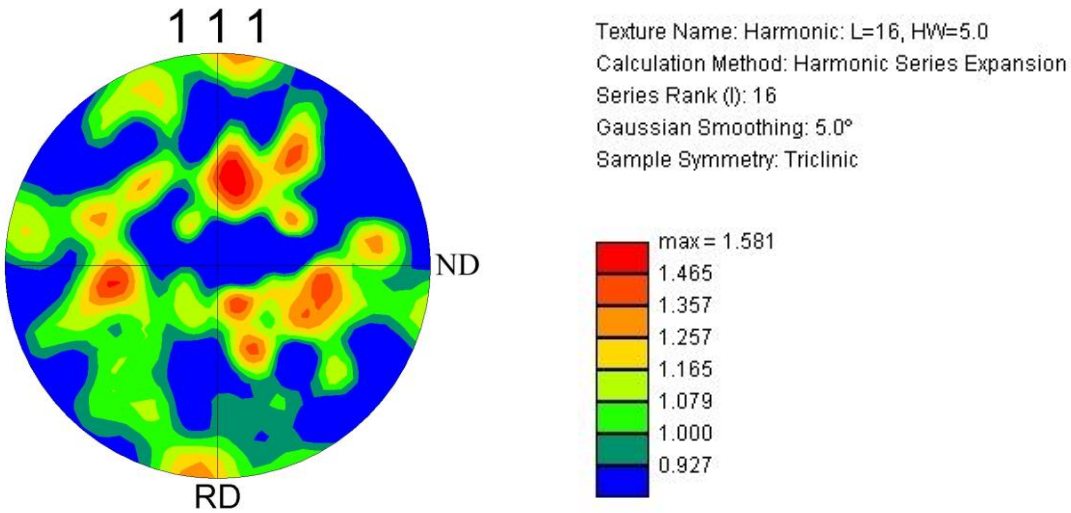

Fig. D.5: Pole figure for C2-B2 annealed at 500 °C for 10^5 s from 90X EBSD-scan

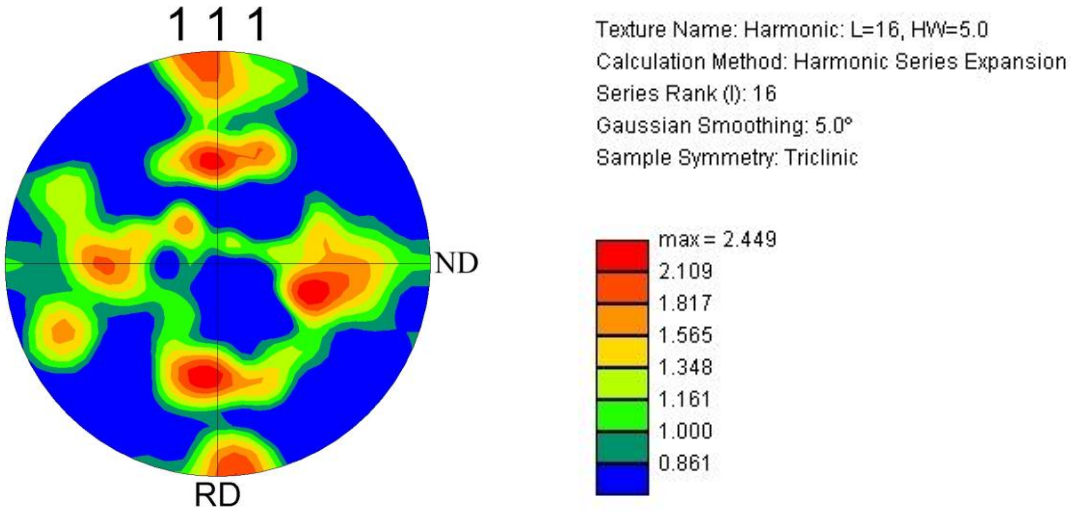

Fig. D.6: Pole figure for C2-B3 annealed at 350 °C for 10^5 s from 80X EBSD-scan

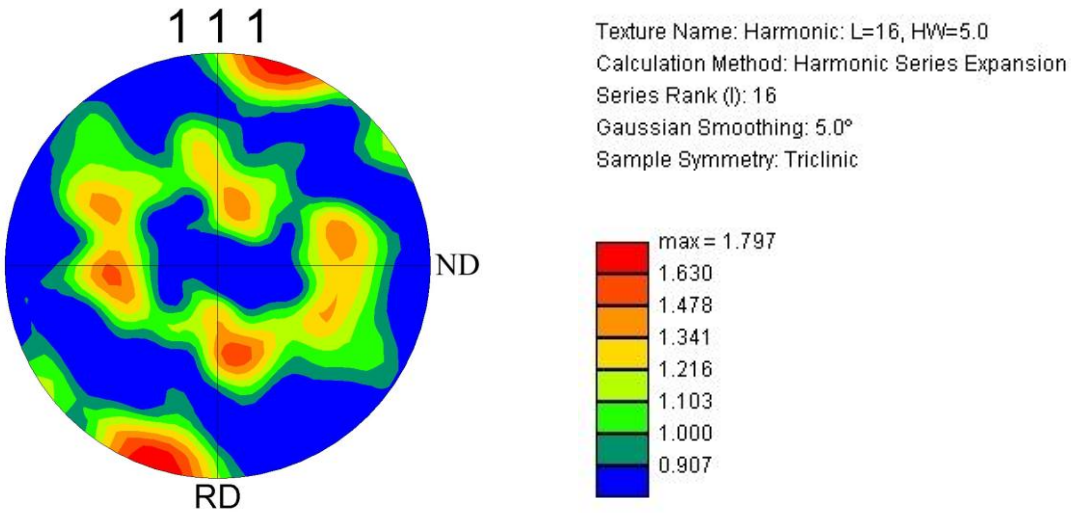

Fig. D.7: Pole figure for C2-B3 annealed at 400 °C for 10^5 s from 80X EBSD-scan

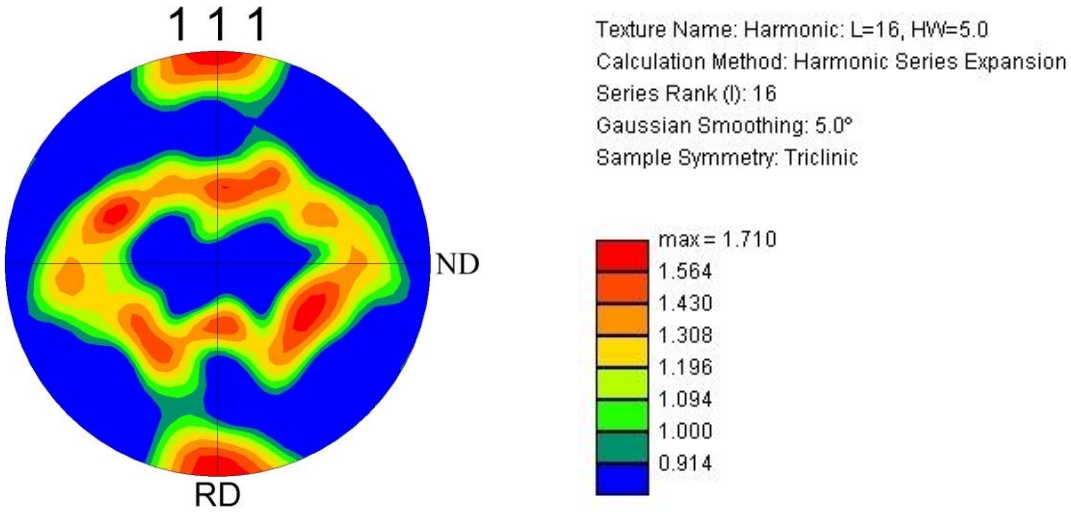

Fig. D.8: Pole figure for C2-B3 annealed at 450 °C for 10^5 s from 80X EBSD-scan

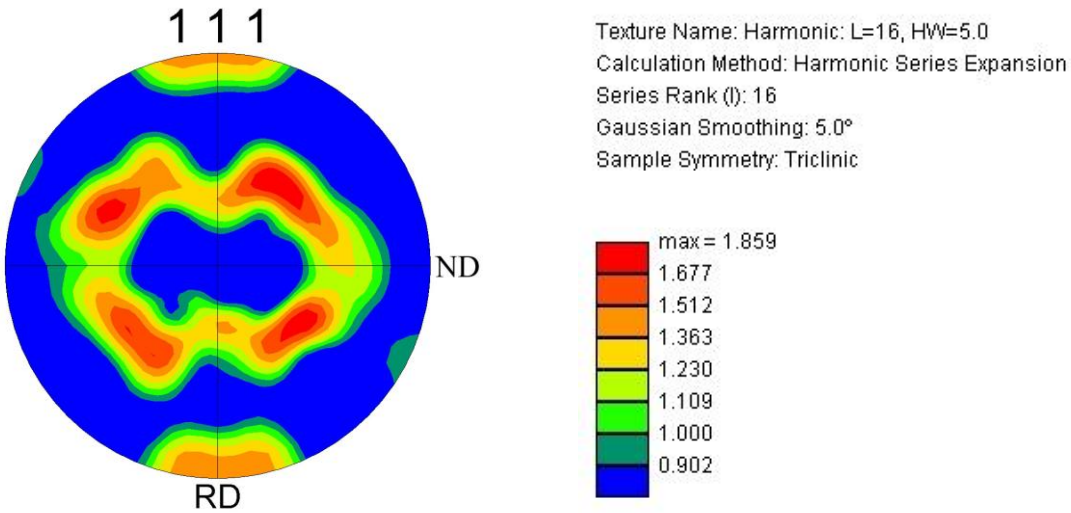

Fig. D.9: Pole figure for C2-B3 annealed at 500 °C for 10^5 s from 80X EBSD-scan

D.2 Non-Isothermally Annealed Specimens

The pole figures from the texture measurements of the non-isothermally annealed specimens described in Chapter 3.5 are presented in the following.

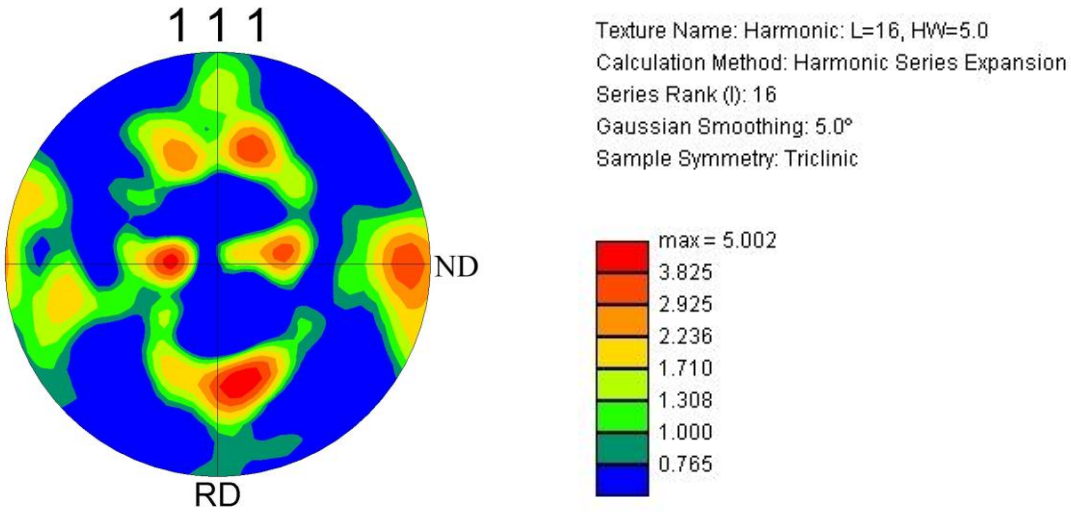

Fig. D.10: Pole figure from a 80X EBSD-scan of C2-A3 non-isothermally annealed and taken out of the oven after 3 h at 400 °C

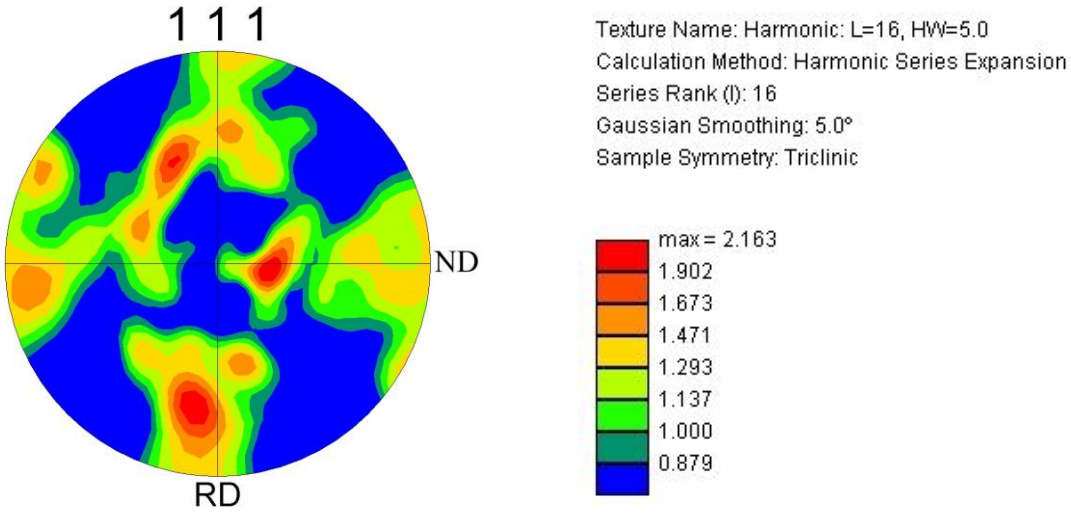

Fig. D.11: Pole figure from a 80X EBSD-scan of C2-B3 non-isothermally annealed and taken out of the oven at 375 °C

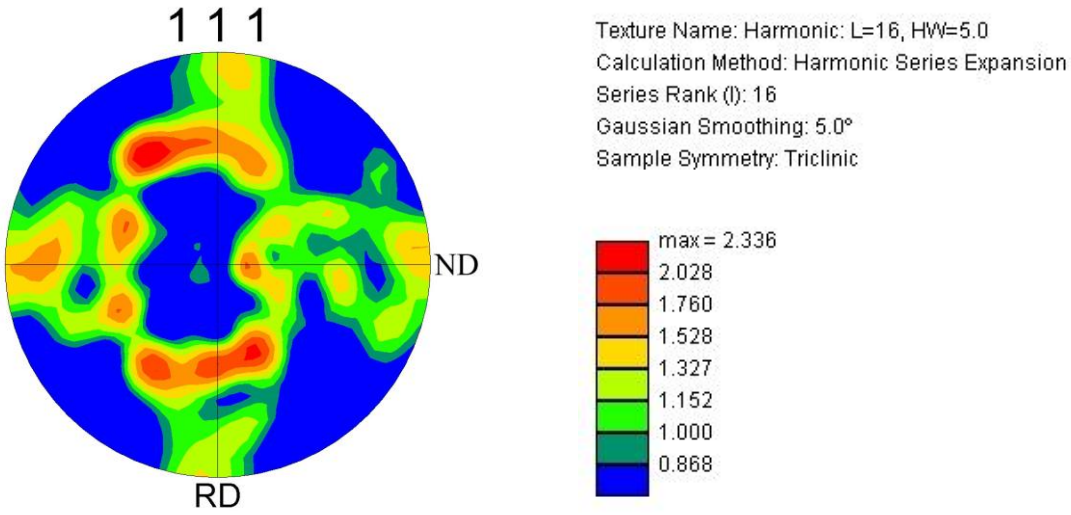

Fig. D.12: Pole figure from a 80X EBSD-scan of C2-B3 non-isothermally annealed and taken out of the oven at 400 °C

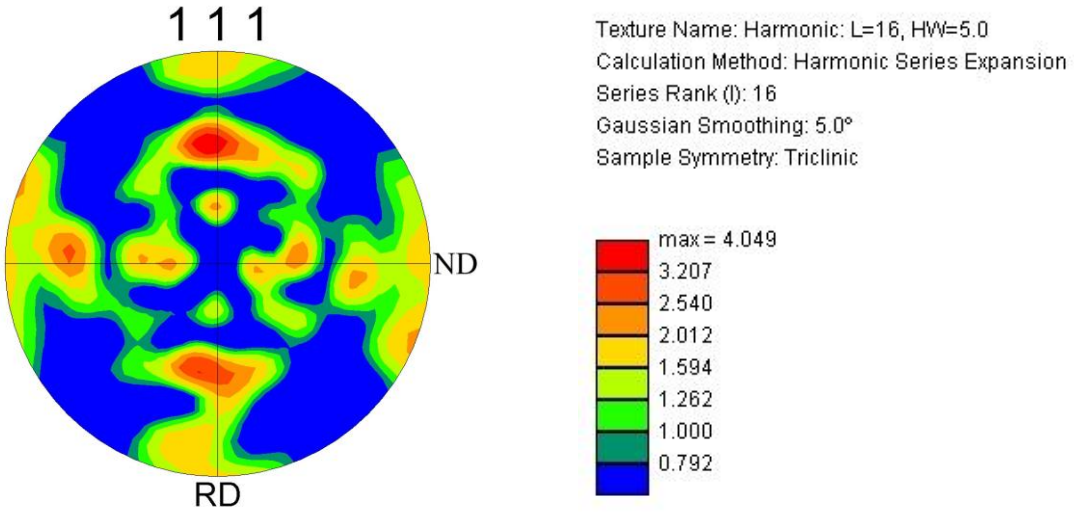

Fig. D.13: Pole figure from a 80X EBSD-scan of C2-C3 non-isothermally annealed and taken out of the oven after 2 h at 400 °C

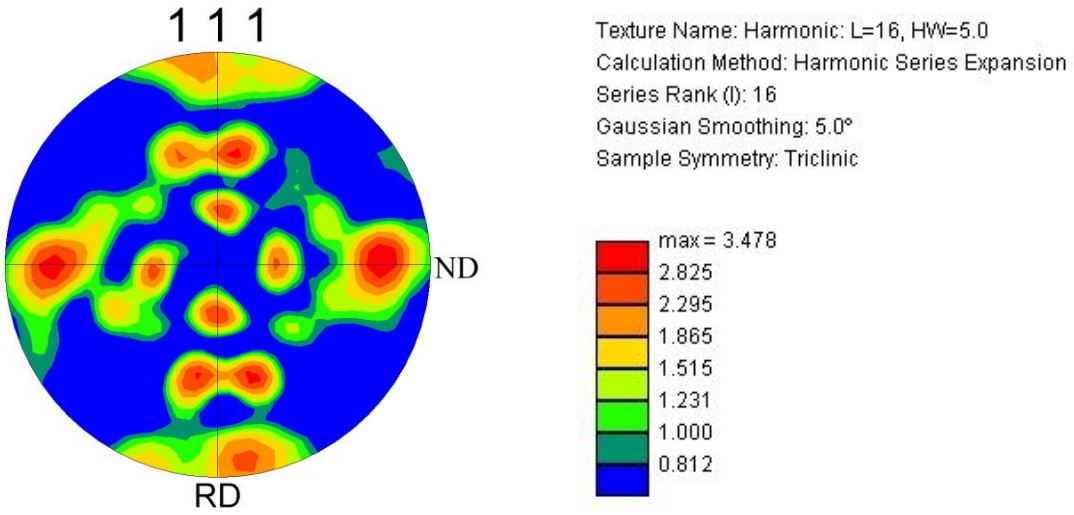

Fig. D.14: Pole figure from a 80X EBSD-scan of C2-C3 non-isothermally annealed and taken out of the oven after 3 h at 400 °C

Appendix E – OM-images

E.1 Initial Characterization

The optical microscope images from the initial characterization described in Chapter 3.2.3 are presented in the following. Fig. E.1 and Fig. E.2 shows the OM-images of C2-A1 and C2-B1. Both images are taken at magnification 20X.

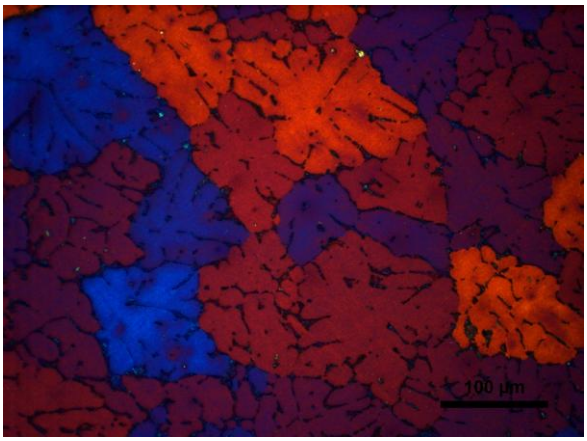

Fig. E.1: OM-image of C2-A1

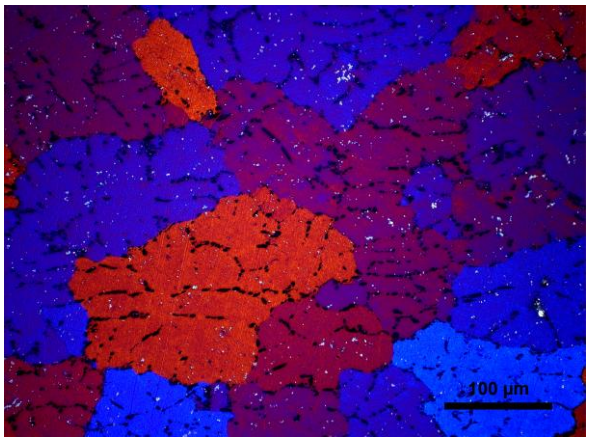

Fig. E.2: OM-image of C2-B1